

富山大学工学部紀要

第36卷

Bulletin of
Faculty of Engineering
Toyama University

Vol. 36

1985

目 次

| | |
|--|--|
| 1. 静剛性が正の自動調整静圧軸受の動特性に及ぼす安定化要素の影響 (周波数応答とインディシャル応答) | ……………大住 剛・森 美郎・池内 健…………… 1 |
| 2. 矩形ダクト内乱流促進体による物質移動の増進機構 (英文) | ……………宮下 尚・若林嘉一郎……………10 |
| 3. 非線形電磁流体波による強制的磁気再結合 (英文) | ……………坂井純一・T. Tajima・F. Brunel……………23 |
| 4. 磁場の収縮時における爆発的静電場と粒子加速 (英文) | ……………坂井純一・T. Tajima・杉原 亮……………32 |
| 5. 太陽フレアにおける融合不安定 (英文) | ……………中島 弘・T. Tajima・F. Brunel・坂井純一……………39 |
| 6. 電流層を伴う太陽紅炎の力学モデル (英文) | ……………坂井純一・鷲見治一……………47 |
| 7. 速い無衝突磁気再結合の計算機によるモデル化 (英文) | ……………J. N. Leboeuf・F. Brunel・T. Tajima・坂井純一・C. C. Wu・J. M. Dawson……………53 |
| 8. 三角行列分解と行列リーマン・ヒルベルト問題 | ……………川田 勉……………66 |
| 9. 昭和58年度修士論文概要一覧…………… | ……………79 |

静剛性が正の自動調整静圧軸受の動特性に及ぼす安定化要素の影響 (周波数応答とインディシャル応答)

大住 剛, 森 美郎*, 池内 健*

1. はしがき

静圧軸受で支持された軸は回転精度が高く、工作機械の主軸に用いると、軸受剛性のほぼ等しい転がり軸受を用いる場合より加工精度と加工効率が高く、振動が生じ難いことが良く知られている。これは油潤滑膜の持つ高いエネルギー吸収能力による。従って、固定絞りを使った静圧軸受は非常に安定な軸受として多く使用されているが、静剛性が有限であるため、できるだけこれを大きくすることが望まれる。そこで考案された自動調整静圧軸受は静剛性を無限大にまで大きくできる。また、この軸受は静剛性を正、および負にも容易に変化できる。しかし、静的に高性能であっても、変動荷重が加わった時には、固定絞りの軸受よりも大きな振動を生じたり、場合によっては軸受系が不安定となる。

静圧気体軸受では、この種の不安定を防止するために安定化要素を接続することにより動特性の改善が計られることが知られている。¹⁾ そこで、この自動調整静圧油軸受についても静剛性が無限大および負の場合に対して、周波数応答およびインディシャル応答におよぼす安定化要素の影響について調べた。^{2),3)}

固定絞りの軸受を使用すれば構造は簡単であるが静剛性に限界がある。一方、可変絞りをを用いて、静剛性を無限大にすれば、軸の回転精度などの動特性が悪くなる傾向がある。従って、この軸受を使って静剛性が固定絞りの場合よりも高く有限値を保つ軸受にすれば、広い作動条件で優れた性能を発揮すると思われる。さらにこの軸受に安定化要素を用いることにより、可変絞りの欠点、すなわち減衰特性が悪く、振動エネルギー吸収量が少い点を補うことができると推定される。

そこで本報では、静剛性が常に正である固定絞りの静圧軸受の動特性⁴⁾と比較しながら、より高い正の静剛性を実現できる場合の自動調整静圧軸受にも毛細管絞りと空気室からなる安定化要素を接続した場合の影響について述べることにする。

2. 理論解析

2.1 軸受系の伝達関数

図1は本実験に使用した軸受系とその寸法を示す。油圧源から供給される圧油(圧力 p_s)は円板弁のすきま(h')を通して試験用軸受ポケット(圧力 p_b)に流入し軸受すきま(h)を通して軸受外に流出する。そして、軸受は軸(負荷 w)を支持する。軸受ポケットには毛細管絞り(半径 r_p 、長さ l)と空気室(圧縮率 γ_x)からなる安定化要素を接続する。また、円板弁と軸受すきま間の残留空気の除去は容易でないので、この影響を無視できるようにポケットに空気室を接続して圧縮性を与える。諸係数および式の誘導の詳細は文献(2),(3),(5)に述べるので基礎式の結果のみを表1に示す。この基

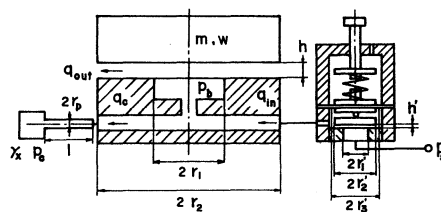


図1 軸受系の概略図

* 京都大学工学部

礎式をもとに基準設定値からの微小変化を考える。すなわち, $q = q_0 + \Delta q$, $h = h_0 + \Delta h$, $h' = h'_0 + \Delta h'$, $p_b = p_{b0} + \Delta p_b$, $w = w_0 + \Delta w$ を表中の式 (1) ~ (7) に代入して線形化する。そして各係数を無次元量の定義に従って無次元化し, $S = d/dT = t_0 S$ としてラプラス変換をおこない ΔW を入力, ΔH を出力と考えた伝達関数として整理すると

$$G(S) = \frac{\Delta H}{\Delta W} = - (B_0 S^4 + B_1 S^3 + B_2 S^2 + B_3 S + B_4) / (A_0 S^6 + A_1 S^5 + A_2 S^4 + A_3 S^3 + A_4 S^2 + A_5 S + A_6) \quad (8)$$

| Eq.No. | Fundamental Equations |
|--------|--|
| 1 | $m d^2 h / dt^2 + \lambda dh / dt - a_b p_b = -w$ |
| 2 | $q_{in} = \pi h^3 (p_b - p_0) / 6 \mu \ln (r_2 / r_1) = c_b h^3 (p_b - p_0)$ |
| 3 | $q_{out} = \pi h^3 p_b / 6 \mu \ln (r_2 / r_1) = c_b h^3 p_b$ |
| 4 | $q_c = \pi r_0^4 (p_b - p_0) / 8 \mu l = c_r (p_b - p_0)$ |
| 5 | $q_c = \gamma_c d p_c / dt$ |
| 6 | $q_{in} - q_{out} - q_c = a_b dh / dt + \gamma d p_b / dt + a_c^* dh' / dt$ |
| 7 | $m' d^2 h' / dt^2 + \lambda' dh' / dt - k h' - a_b^* p_b - a_b^* p_0 = 0$ |

$a_b^* = \pi r_0^4 - a_b^*$, λ, λ' : viscosity damping coefficients of bearing clearance and disk valve clearance

表1 基礎方程式

が得られる。ここで分母, 分子の係数は無次元量を使って表2のように表わされる。

軸の静剛性は $-|\Delta W / \Delta H|_{static} = -\Delta W_0 / \Delta H_0 = A_6 / B_4 = 3K / (\beta K - 3)$ となり, $K=1.0$ とすると軸受の静剛性は3.0となり固定絞りの場合の4倍にまで高められている。ただし, $\beta = 4.0$ とする。

また, 諸式の誘導に当って次の5つの仮定をおこなった。

- 1) 軸受, 円板のすきまは一樣で, 軸と円板は荷重の方向に平行に動く。
- 2) 軸受, 円板弁のすきま部では, 油は粘性流であり, 配管中および軸受ポケット部においては圧力降下はない。
- 3) 軸受と円板弁のすきま部および配管中での油の圧縮性は無視できる。
- 4) 油の慣性力は無視できる。
- 5) 荷重の変動に対する各係数の変化量は基準設定値に比べて小さい。

2.2 エネルギー吸収率

軸受の動特性の評価関数としてエネルギー吸収率を定義^{2),3)}した。その結果を述べる。

2.2.1 周波数応答におけるエネルギー吸収率²⁾ 単位時間当りの吸収エネルギー e_d (エネルギー吸収率) は, 後述の記号を使用すると $e_d = \Delta w_0 \Delta h_0 \omega \sin \psi / 2$ となる。また, 無次元エネルギー吸収率 E_d と e_d の間には

$$E_d = e_d a_b p_s t_b / \{h_0 (\Delta w_0)^2\} = (\Delta H_0 / \Delta W_0) Q \sin \psi / 2$$

の関係がある。ここで $\sin \psi = \text{Imag}\{G(j\Omega) / |G(j\Omega)|\}$ を代入すると, $E_d = \text{Imag}\{G(j\Omega)\}$ より E_d が計算できる。

2.2.2 インディシャル応答に対するエネルギー吸収率³⁾ 単位負荷が単位負荷変化を受けた時の単位時間当りのエネルギー吸収量としてエネルギー吸収率 e_d を定義すると, $e_d = -(w / \Delta w) d(\Delta h / \Delta w) / dt$ となり, 無次元エネルギー吸収率 E_d との間に $E_d = -(W / \Delta W) d(\Delta H / \Delta W) / dT = (a_b^2 p_s / q_0) e_d$ の関係がある。

また, 安定化要素自身のエネルギー吸収率 e_{da} , 絞りのエネルギー散逸率 e_{db} , 空気室のエネルギー吸収率 e_{dc} は次のように定義される。

| | |
|-------|--|
| A_0 | $\tau^2 M \Gamma \Gamma$ |
| A_1 | $\tau^2 M \Gamma a + (\tau^2 M M a + \Gamma(\tau \Delta M + \tau^2 M \Delta) + \beta \tau^2 M M) \Gamma$ |
| A_2 | $(\beta \tau^2 M M + \Gamma(\tau \Delta M + \tau^2 M \Delta)) a + (\tau \Delta M + \tau^2 M \Delta) a + (\tau^2 M \Delta + \tau \Delta M) \beta$ $(\tau^2 M + \tau M + \Gamma(K M + \tau \Delta \Delta)) \Gamma$ |
| A_3 | $(\tau^2 M \Delta + \tau \Delta M) \beta + \Gamma(K M + \tau \Delta \Delta) + (\tau^2 M + \tau M) a + (K M + \tau \Delta \Delta) a$ $+ 3 \tau^2 M + (\beta K - 3) M + \tau \Delta + (K \Gamma + \tau \Delta + \beta \tau \Delta \Delta) \Gamma$ |
| A_4 | $(3 \tau^2 M + (\beta K - 3) M + \tau \Delta + (K \Gamma + \tau) \Delta + \beta \tau \Delta \Delta) a + (3 \tau \Delta + (\beta K - 3) \Delta$ $+ a K \Delta + K) \Gamma$ |
| A_5 | $(3 \tau \Delta + (\beta K - 3) \Delta + K) a + 3 K \Gamma$ |
| A_6 | $3 K a$ |
| B_0 | $\tau^2 M \Gamma \Gamma$ |
| B_1 | $\tau^2 M \Gamma a + (\tau^2 M a + (\beta \tau^2 M + \tau \Delta \Gamma)) \Gamma$ |
| B_2 | $(\beta \tau^2 M + \tau \Delta \Gamma) a + (\tau \Delta a + \tau + \beta \tau \Delta + K \Gamma) \Gamma$ |
| B_3 | $(\tau + \beta \tau \Delta + K \Gamma) a + (K a + \beta K - 3) \Gamma$ |
| B_4 | $(\beta K - 3) a$ |

表2 伝達関数の係数

$$e_{da} = (\Delta q_c / \Delta w)(p_{b0} + \Delta p_b) / \Delta w, \quad e_{db} = (\Delta q_c / \Delta w)(\Delta p_b - \Delta p_c) / \Delta w$$

$$e_{dc} = (\Delta q_c / \Delta w)(p_{b0} + \Delta p_b) / \Delta w$$

従って、無次元量との間にそれぞれ次の関係が成立する。

$$E_{da} = (a_s^2 p_s / q_0) e_{da}, \quad E_{db} = (a_s^2 p_s / q_0) e_{db}, \quad E_{dc} = (a_s^2 p_s / q_0) e_{dc}$$

3. 数値計算結果とその考察

本章では、ポケット内圧縮率 Γ 、安定化要素絞りの流量係数 α 、安定化要素の空気室の圧縮率 Γ_x を変化させた場合の周波数応答およびインディシャル応答について述べる。

3.1 周波数応答

3.1.1 Γ の影響、図2は周波数応答およびエネルギー吸収率に与える Γ の影響であるが図2(a)は $\Delta H_0 / \Delta W_0$ を示す。 $\Gamma = 0.0$ では周波数の増加につれて、 $\Delta H_0 / \Delta W_0$ は次第に減少し $(\Delta H_0 / \Delta W_0)_{\max}$ は存在しない。 Γ が増加するにつれて $(\Delta H_0 / \Delta W_0)_{\max}$ が存在し、その値は急激に大きくなる。また、 $(\Delta H_0 / \Delta W_0)_{\max}$ を与える Ω は Γ の増加につれて減少する。全体の傾向は固定絞りの場合⁴⁾と同じであるが $(\Delta H_0 / \Delta W_0)_{\max}$ が大きく、 Ω の変化に対する $(\Delta H_0 / \Delta W_0)$ 値の変化割合も大きい。

図2(b)は ψ と Ω の関係を示すが、全体の傾向は固定絞りの場合⁴⁾と同じで Ω の増加につれて、 180° 以上になった後 90° に急減し、 90° ではほぼ一定値を保った後 Ω が 4×10^2 以上となると急減する。しかし、 $\Gamma = 0.0$ の場合は 180° から 90° への減少率は非常に小さい。

図2(c)は E_d を示す。 $\Delta H_0 / \Delta W_0$ および ψ の傾向は固定絞りの場合⁴⁾と同じであるため、 E_d の傾向も同じである。 $\Gamma = 0.0$ の場合は ψ の 180° から 90° の減少率が極端に小さい影響により $\Omega \approx 10 \sim 4 \times 10^2$ 間の E_d は Ω の増加に対し緩慢な増加関数であるが、それ以上となると、 $E_d \approx 0.7$ となり $\Gamma = 0.0$ の場合と同じ値となり固定絞りの場合の $E_d = 0.5$ に比べて大きい。

Γ が大きすぎると(例えば図2(c)で $\Gamma = 4.0$ 以上) E_d は低周波数まで $E_d > 0$ とでき、吸収能力の周波数領域が広がるが低周波数での $E_d < 0$ の絶対値も大きく、かつ $\Delta H_0 / \Delta W_0$ も大きくなるので、わずかの Γ を与え、大きくても $\Gamma = 2.0$ 程度で使用した方が有効である。

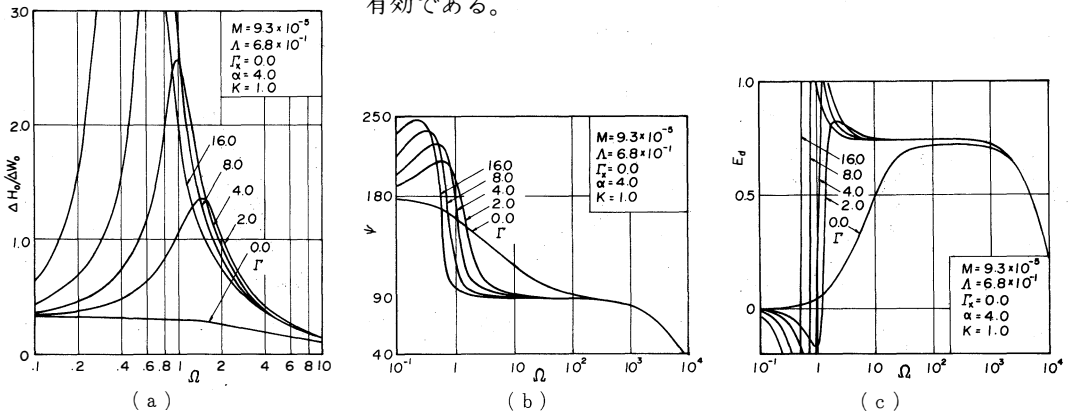


図2 $\Delta H_0 / \Delta W_0$, ψ , E_d に及ぼす Γ の影響

3.1.2 α の影響 図3は α の影響を示すが、 $\Delta H_0 / \Delta W_0$ を示す図3(a)では α の増加により $(\Delta H_0 / \Delta W_0)_{\max}$ が増加して行くが、それを与える Ω はほとんど変化しない。

図3(b)は ψ を示す。 180° から 90° へ急変する Ω は α によってほとんど影響を受けない。

図3 (a), (b)で説明したように, $(\Delta H_0/\Delta W_0)_{\max}$ および 180° から 90° へ変化する Ω は α によってほとんど影響されないで, 図3 (c)によると, $E_d > 0$ の周波数領域を広げることにはできない。しかし, α が小さいと(例えば $\alpha = 1.0$ の曲線), E_d は $\Gamma = 0.0$ の場合と同じ傾向となるので, 図3 (c)の $\alpha = 4.0$ の曲線となる程度の α を選んだ方が $\Omega \approx 0.8 \sim 8$ の E_d を大きくできて良い。

図2 (c)および図3 (c)でみられるように, 安定化要素の存在はエネルギー吸収の点では, 静剛性が正の場合も有効であることがわかる。

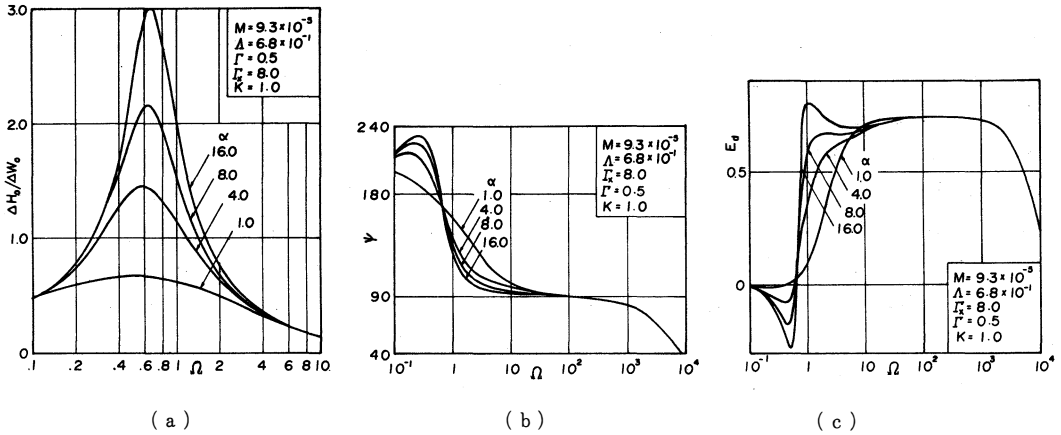


図3 $\Delta H_0/\Delta W_0$, ψ , E_d に及ぼす α の影響

3. 1. 3 Γ_x の影響 図4 (a)は $\Delta H_0/\Delta W_0$ の周波数特性を示すが, Γ_x の増加により $(\Delta H_0/\Delta W_0)_{\max}$ が大きくなり, それを与える Ω が減少する。しかし, Γ の増加の場合と比べて, $(\Delta H_0/\Delta W_0)_{\max}$ を与える Ω が減少する性質は同じであるが, $(\Delta H_0/\Delta W_0)_{\max}$ はそれほど大きくならず, Γ の増加の影響とは異なることがわかる。

図4 (b)は ψ と Ω の関係を表わすが, Ω の増加につれて 180° から急激に 90° に減少しさらに Ω の増加により減少を続ける性質は Γ の影響(図2 (b)参照)と同じであり固定絞りの Γ の影響⁴⁾とも類似である。しかし, 180° から 90° への急減の程度は図2 (b)に比べてややゆるやかである。

図4 (c)は E_d を表わす。 $\Delta H_0/\Delta W_0$ が大きくて, ψ が 90° に近いほど E_d は大きくなることは E_d の定義の示す通りであり,

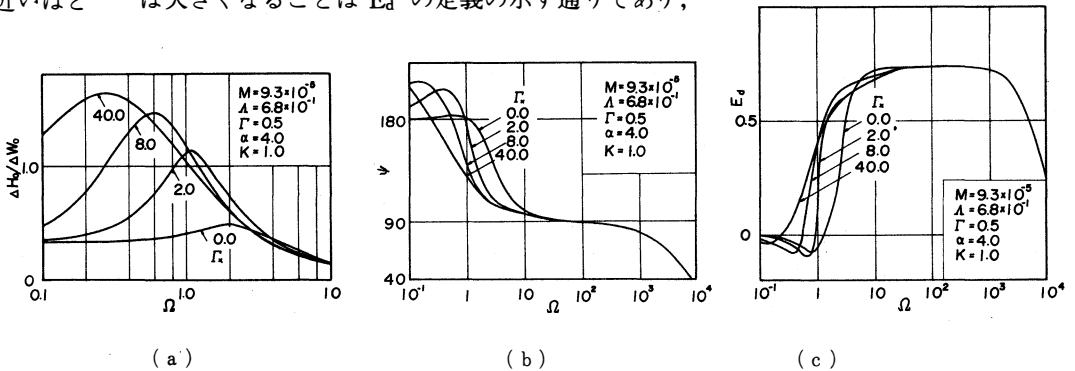


図4 $\Delta H_0/\Delta W_0$, ψ , E_d に及ぼす Γ_x の影響

従って全体の性質は図2 (c)と類似であるが, 図4 (b)で述べたように 180° から 90° への変化はは余り大きくないため, E_d を正とする範囲が低周波領域にまで広がっており, Γ , α の影響の場合

と著しく異なり、安定化要素の接続によりエネルギー吸収率が大きくなるので、振動荷重下での回転精度が高くなることが予測される。

3.2 インディシャル応答

3.2.1 α の影響 図5(a)

は α の影響を示すインディシャル応答で α の増加により最初の極値と第2の極値の振幅 ($\Delta H/\Delta W$)_{p-p} が大きく、振動性も大きくなり、 α が小さい方がよい。しかし、図5(b)

に示すように、 $\alpha = 0.0$ の場合には衝撃直後の E_d は小さく、正である時間も $\alpha \neq 0.0$ に比べて短かいので、安定化要素の接続の意味がある。

3.2.2 Γ_x の影響 図6(a)

は Γ_x を変化させた場合の $\Delta H/\Delta W$ のインディシャル応答である。 Γ_x の増加につれて $\Delta H/\Delta W$ のピーク値は大きくなるが、振動性がなくなる。 $\Gamma = 0.0$ の場合は $\Gamma_x \neq 0.0$ に比べて $\Delta H/\Delta W$ のピーク値は極端に小さく、 $\Delta H/\Delta W$ のみを考える限り、安定化要素の有効性は認め難い。

図6(b)に E_d を示すが、 $\Gamma_x = 0.0$ の場合に比べて荷重変動直後の E_d が非常に大きく、また $E_d > 0$ の時間も長く、エネルギー吸収の点では安定化要素の接続は有効である。

そこで E_{da} を調べてみると、図6(c)に示すように荷重変動直後の E_{da} は非常に大きく、 E_d との時間おくれも大きく $E_{da} > 0$ の時間が非常に長いことから、一時的にエネルギーの吸収が起っていることが良くわかる。

図6(e)の E_{dc} は E_{da} とほとんど同じ形をしており E_{da} の大部分が E_{dc} に吸収されることがわかる。

これに対して、図6(d)の毛細管絞りでの E_{db} はわずかであり、空気室からの逆流による散逸は特に小さい。

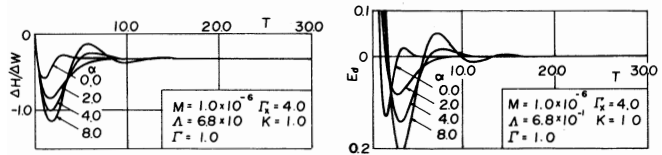
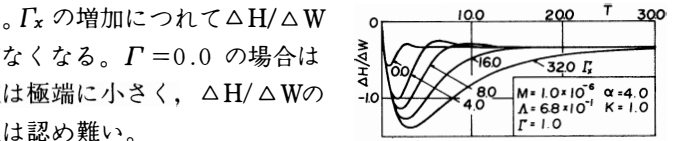
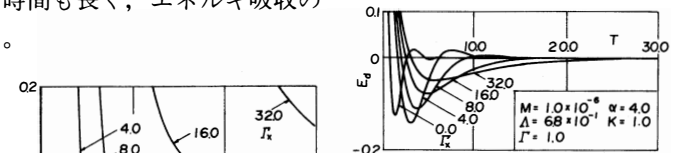


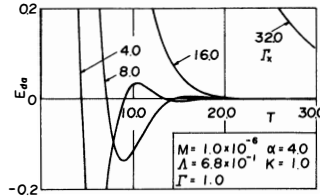
図5 $\Delta H/\Delta W$, E_d に及ぼす α の影響



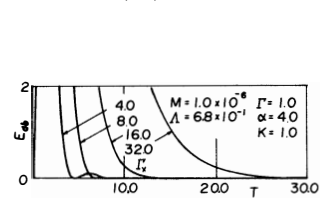
(a)



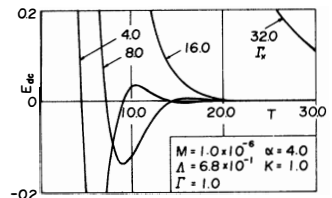
(b)



(c)



(d)



(e)

図6 $\Delta H/\Delta W$, E_d , E_{da} , E_{db} , E_{dc} に及ぼす Γ_x の影響

4. 実験装置とその方法

図7は計算結果を検討するためにおこなった実験装置の概略である。油圧源から供給された圧油は円板弁で絞られて、試験用軸受に流入し軸を浮上させる。

軸は静圧気体軸受で支持され、荷重の変動方向に平行に動き、摺動による摩擦が無視できるようにした。

発振器から正弦波または矩形波を電力増幅して、軸に接続した電磁石に加えて荷重変動を与え、その変動をロードセルにより検出した。

容量形変位形または差動トランスにより、軸変位を測定した。

5. 実験結果とその検討

本節では安定化要素の空気室の空気量を変え、圧縮率 γ_x を変化させた場合の軸受の周波数応答およびインディシャル応答について述べることにする。

表3は周波数応答とインディシャル応答の実験条件を示す。表中、静剛性が26.0N/ μm のものは周波数応答の場合の実験条件であり、16.0N/ μm の場合はインディシャル応答の時の実験条件を示している。

図8は周波数応答の実験と計算の結果を示すが、図8(a)では γ_x が大きいほど Δh_0 は低周波で最大値をとり、その値は大きい。実験値は定性的には理論値とよく一致しているが、最大値は理論値よりやや小さい。

図8(b)は ψ を示しているが、 γ_x が大きい場合には ψ は 180° より大きくなる。そして、 180° から 90° への減少は低い周波数で起る。1.0~3.0 Hzでは、実験値が理論値より大きい、これより周波数 f が小さい時には、実験値は理論値とよく一致している。このように位相の実験値と計算値の差の大きいのは入力荷重変動と出力変位の波形の比較から位相の測定をおこなっているため、時間軸の読み取り誤差が大きいことによると思われる。

図8(c)は e_a を示すが、図中の実験値は e_a の定義式に図8(a),(b)の測定値を代入して求めた。 γ_x の増加につれて e_a の負を与える周波数は低周波領域に移り、振動吸収能力の周波数域が広がる。実験値は理論値の傾向を良く示しているが、実験値が計算値より小さくなるのは主として位相の実験値と理論値の差によるものである。

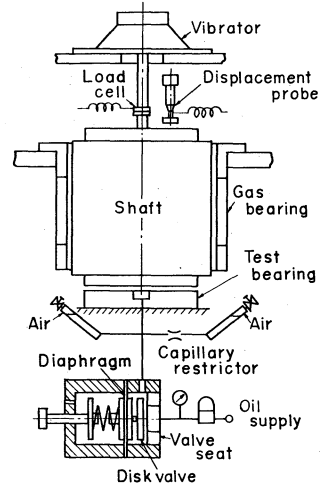


図7 実験装置の概略

| Symbol | Stiffness N/ μm | | Symbol | Stiffness N/ μm | |
|-----------------------------|----------------------------|-------------------|---------------------------|----------------------------|--------------------|
| | Fig. 8 | Fig. 9 | | Fig. 8 | Fig. 9 |
| a_b cm ² | 10.8 | 10.8 | p_{b0} MPa | 0.318 | 0.318 |
| a_0 cm ² | 1.26 | 1.26 | q_0 cm ² /s | 0.19 | 0.03 |
| πr_s^2 cm ² | 4.15 | 4.15 | t_b s | 0.188 | 1.6 |
| h_0 μm | 33 | 43 | t'_b s | 0.036 | 0.304 |
| h'_0 μm | 23 | 30 | Δw N | 19.6 | 9.8 |
| k N/cm | 150×10^3 | 194×10^3 | λ Ns/cm | 26×10^6 | 173×10^5 |
| m kg | 3502 | 3502 | χ Ns/cm | 0.56×10^3 | 3.66×10^2 |
| m' kg | 0.05 | 0.05 | μ Pa \cdot s | 0.014 | 0.199 |
| P_b MPa | 0.636 | 0.636 | C_I cm ² /Ns | 0.013 | 0.008 |

表3 実験条件

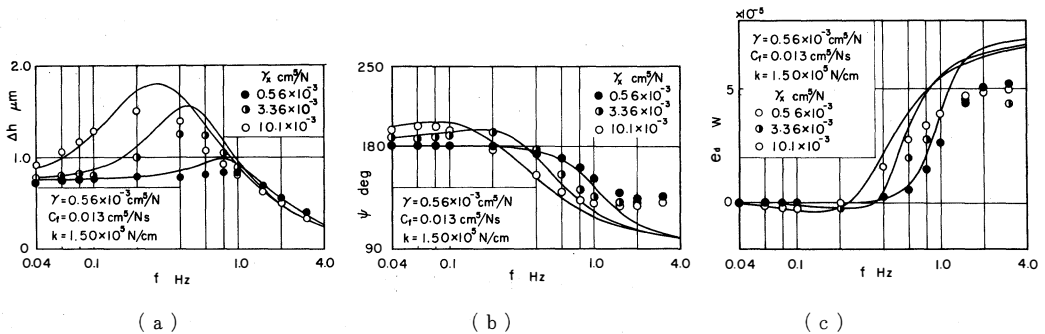


図8 $\Delta h_0, \psi, e_a$ に及ぼす γ_x の影響

図9は γ_x を変化させた場合の理論値と実験値の対応を示す。 γ_x の増加により、 Δh の最初の極値は増加するが、振動性がなくなることは図6(a)で述べたが、本実験では γ_x の値が十分大きくなかったため、振動性の抑制が顕著に表われる図は得られなかった。しかし全体として実験値と計算

値は良く対応している。

6. あとがき

実験値と計算値の良い対応を見たので、数値計算によって得られた結果をまとめて述べる。

(1) 自動調整静圧軸受に2.0程度の Γ を与えることによりエネルギー吸収率が改善できる。

(2) 安定化要素のない自動調整静圧軸受は $\Gamma=0.0$ では固定絞りの軸受より動特性はすぐれている。

(3) 静剛性が正の自動調整静圧軸受に安定化要素を接続することにより Γ の大きな振動性のある軸受の動特性を改善できる。

(4) 静剛性が正の自動調整静圧軸受に安定化要素を接続することによりエネルギー吸収率を低周波領域まで正に広げることができる。

(5) 静剛性が正の自動調整静圧軸受に安定化要素を接続することにより短時間における衝撃エネルギーの吸収量と吸収時間を大きくできる。

最後に、本研究をおこなう機会を与えて下さった富山大学工学部、中川孝之教授に深く感謝します。また、実験に御協力下さった当時、本学学生だった松倉泉、鷲北健二、茶谷渉の諸氏に深く感謝します。

尚、本報は昭和57年6月18日、機械学会北陸信越支部地方講演会(福井)発表の一部に加筆したものである。

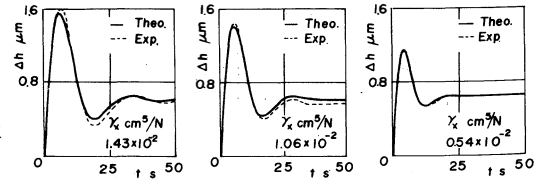


図9 Δh に及ぼす γ_x の影響

記号

有次元量

| | |
|-----------|--|
| a_b | : 有効軸受面積, $\pi(r_2^2 - r_1^2) / \{2\ln(r_2/r_1)\}^{5)}$ |
| h | : 軸受すきま |
| m | : 軸の質量 |
| p_s | : 供給圧力 |
| p_b | : 軸受ポケット内圧力 |
| Q_{in} | : 軸受流入流量 |
| Q_{out} | : 軸受流出流量 |
| Q_c | : 安定化要素空気室への流入流量 |
| w | : 軸荷重 |
| λ | : 軸受すきま部の油膜の粘性減衰係数 $1.5\pi\mu(r_2^2 - r_1^2)\{r_2^2 + r_1^2 - (r_2^2 - r_1^2) / \ln(r_2/r_1)\} / h_0^3$ |
| γ | : 円板弁と軸受すきま間の空気の圧縮率 |
| t_b | : 軸受の時定数 $a_b h_0 / q_0$ |
| μ | : 油の粘度 |
| a_b | : 円板弁の有効受圧面積 $\pi(r_2^2 - r_1^2) / \{2\ln(r_2/r_1)\}$ |

| | |
|------------|---|
| h' | : 円板弁すきま |
| k | : 円板弁支持部のバネ定数 |
| m' | : 円板弁可動部の質量 |
| t_b' | : 円板弁の時定数, $(\pi r_3^2 - a_b') h_0' / q_0$ |
| λ' | : 円板弁すきま部の油膜の粘性減衰係数 $1.5\pi\mu(r_2'^2 - r_1'^2)\{r_2'^2 + r_1'^2 - (r_2'^2 - r_1'^2) r_1'^2 / \ln(r_2'/r_1')\} / h_0'^3$ |
| r_1 | : 軸受ポケット半径 |
| r_2 | : 軸受外周半径 |
| r_1' | : 円板弁弁座内径/2 |
| r_2' | : 円板弁弁座外径/2 |
| r_3 | : 板バネ有効半径 |
| γ_x | : 安定化要素の空気室の空気の圧縮率 |
| C_{ab} | : 軸受すきま部の流量係数 $\pi / \{6\mu\ln(r_2/r_1)\}^{5)}$ |
| C_b' | : 円板弁すきま部の流量係数 $\pi / \{6\mu\ln(r_2'/r_1')\}^{5)}$ |
| C_f | : 安定化要素絞りの流量係数 |

| | |
|--|---|
| Δh : 軸受すきまの変化 | ΔH : $\Delta h/h_0$ |
| Δw : 軸荷重の変化 | ΔP_b : $\Delta p_b/p_s$ |
| Δh_0 : 軸受すきまの変化振幅 | ΔW : $\Delta w/(a_b p_s)$ |
| Δw_0 : 軸荷重の変化振幅 | Λ : $\lambda q_0/(a_b^2 p_s)$ |
| e_a : エネルギー吸収率 | Γ : $\gamma p_s/(a_b h_0)$ |
| e_{da} : 安定化要素のエネルギー吸収率 | Γ_x : $\gamma_x p_s/(a_b h_0)$ |
| e_{db} : 安定化要素絞りのエネルギー散逸率 | M : $m' q_0^2 / \{(\pi r_3^2 - a_b')^3 p_s h_0'\}$ |
| e_{dc} : 安定化要素空気室のエネルギー吸収率 | Λ' : $\lambda' q_0 / \{\pi r_3'^2 - a_b'\}^2 p_s\}$ |
| $\Delta h'$: 円板弁すきまの変化 | $\Delta H'$: $\Delta h'/h_0'$ |
| s : ラプラス演算子 | α : $C_f p_s / q_0$ |
| $\overline{\Delta h}$: Δh のラプラス変換 | τ : t_b'/t_b |
| $\overline{\Delta w}$: Δw のラプラス変換 | T : t/t_b |
| q_0 : 基準状態の流量 | β : $1 / \{P_{b0}(1 - P_{b0})\}$ |
| h_0 : 基準状態の軸受すきま | S : $d/dT = t_b s$ |
| p_{b0} : 基準状態のポケット内圧力 | $\overline{\Delta H}$: ΔH のラプラス変換 |
| 無次元量 | $\overline{\Delta W}$: ΔW のラプラス変換 |
| M : $m q_0^2 / (a_b^3 p_s h_0)$ | K : $kh_0' / \{(\pi r_3'^2 - a_b') p_s\}$ |
| P_b : p_b / p_s | |

参考文献

- 1) 森美郎, 森 淳暢: 日本機械学会論文集, 32, 244 (1966) 1877.
- 2) 大住 剛, 森 美郎, 池内 健, 梶谷克人: 潤滑, 29, 2 (1984)
- 3) 大住 剛, 森 美郎, 池内 健 : 潤滑, 30, 3 (1985)
- 4) 大住 剛, 森 美郎, 池内 健 : 潤滑, 28, 10 (1982) 739
- 5) 森 美郎, 池内 健, 高田秀希: 潤滑, 20, 9 (1974) 651

Effects of Stabilizer on Dynamic Characteristics of Self-Controlled Externally Pressurized Bearing with Positive Static Stiffness

(Frequency and Indicial Responses)

Tsuyoshi OHSUMI, Haruo MORI, Ken IKEUCHI

In a self-controlled externally pressurized thrust bearing with positive static stiffness attaching a stabilizer which consists of capillary restrictor and air chamber, its effects were investigated on frequency and indicial responses and compared with those of an externally pressurized bearing with a fixed restrictor.

As the result, it was proved that this bearing could be made superior to the bearing with a fixed restrictor in static and dynamic characteristics.

〔英文和訳〕

静剛性が正の自動調整静圧軸受の動特性に及ぼす安定化要素の影響
(周波数応答とインディシャル応答)

大住 剛, 森 美郎, 池内 健

毛細管絞りと空気室からなる安定化要素を接続した静剛性が正の自動調整静圧スラスト軸受において、固定絞り静圧軸受と比較しながら周波数応答およびインディシャル応答に及ぼす影響を調べた。

その結果、静特性および動特性において、固定絞り軸受より優れたものにする事ができることがわかった。

(1984年10月31日受理)

Augmentation Mechanism of Mass Transfer Among Turbulence Promoters on Wall Surface in Rectangular Duct

Hisashi MIYASHITA, and Kaichiro WAKABAYASHI

Department of Chemical Engineering
Toyama University, Takaoka, 933, JAPAN

ABSTRACT

An augmentation mechanism of mass transfer was investigated phenomenologically by using turbulence promoters on the wall surface in a rectangular duct. The augmentation of local mass transfer among the turbulence promoters was measured by varying the diameter, the pitch of the promoters and the clearance between the promoters and the wall. In order to examine the augmentation mechanism, wall shear stress, mass transfer intensity and turbulence intensity at the wall were measured by an electrochemical method. Further, flow behaviors were measured by visualization.

It was found phenomenologically that the augmentation of mass transfer with the clearance was caused by turbulence due to reattachment flow, large scale eddies and increase of shear stress due to flow jet under the promoters and was caused by only turbulence on the wall surface in case of no clearance.

1. INTRODUCTION

It is well known that roughening the surface by use of turbulence promoters (regular geometric roughness element) on the wall surface in a duct improves the heat transfer from the surface for the design of compact heat exchanger. The increase in heat transfer is accompanied by an increase in resistance to fluid flow. The problem of optimizing heat transfer performance for given flow friction has been studied by many investigators. Some of them are shown in Table 1.

It has been found in practical applications that an increase in flow resistance does not always decrease energy efficiencies. However, few investigations of the augmentation mechanism of heat transfer have been published.

Mori et al[16] and Fujita et al[4] suggested that augmentation of heat transfer depends mainly on turbulence intensity near the wall surface-downstream from a single cylinder turbulence promoter placed on the transfer wall in a rectangular duct.

Miyashita et al[14] pointed out that augmentation depends on the turbulence intensity near the wall surface in the case of no clearance between promoter and wall, and depends not only on the turbulence intensity but also on the shear stress at the wall in the case of non-zero clearances in a rectangular duct.

In this paper, the augmentation ratio of local mass transfer coefficients among the promoters was measured by varying the diameter, the pitch of the promoter and the clearance between

promoter and wall surface. Flow behavior was observed by visualization. Wall shear stress, mass transfer intensity at the wall and turbulence intensity close to the wall surface were measured by an electrochemical method, in order to examine the detailed augmentation mechanism of heat/mass transfer on the wall surface among the turbulence promoters in a rectangular duct.

| INVESTIGATORS | GEOMETRY | PROMOTER | FULUID | EXPERIMENTAL CONDITION |
|--------------------|---|-----------------|-------------------------|--|
| Mori et al.[16] | rectangular duct (H=33mm,W=77mm) | cylinder | electrolyte solution | Re=4.5x10 ⁴ ,H/Dp=6.6 |
| Kasagi et al.[9] | water tunnel | (step) | water | U _b =25-60cm/s,step height=10,20,30cm |
| Igarashi et al.[8] | wind tunnel | (step) | air | U _∞ =6-24cm/s, step height=10cm |
| Fujita et al.[4] | wind tunnel | cylinder | air | U _∞ =20cm/s, Dp=5mm |
| Oyakawa et al.[18] | rectangular duct (H=50mm,W=300mm) | cylinder | air | Re=2.5x10 ⁴ ,H/Dp=1.25-2.5 |
| Hanawa et al.[6] | rectangular duct (H=10mm,W=50mm) | cylinder | air | Re=6x10 ³ -3x10 ⁴ , H/Dp=2,P/Dp=5,10, 15,20 |
| Rao et al.[20] | annulus (Do=152mm,Di=76mm) | wire ring | air | Re=9x10 ⁴ -2.2x10 ⁵ , (Do-Di)/2Dp=30,42 P/Dp=3,7,10 |
| Furuya et al.[5] | wind tunnel | cylinder | air | U _∞ =13,21cm/s,Dp=2mm,P/Dp=1-64 |
| Han et al.[7] | rectangular duct (H=13,25mm,W=301mm) | rectangular rib | air | Re=3x10 ³ -3x10 ⁴ ,H/e=10-30,P/e=5-20 |
| Konno et al.[11] | rectangular duct (H=2.6, 5mm,W=70mm) | cylinder | water | Re=8x10 ² -3x10 ⁴ ,H/Dp=1.3-3.1,P/Dp= 2-56 |
| Oyakawa et al.[19] | rectangular duct (H=50mm, W=300mm) | cylinder | air | Re=9x10 ⁴ -1.7x10 ⁵ ,H/Dp=2.5, P/Dp= 4,8,12 |

Table 1 Investigations on enhanced heat transfer using turbulence promoters

2. EXPERIMENTAL APPARATUS AND PROCEDURE

A schematic diagram of the experimental apparatus and a detail of the test section are shown in Fig.1 and Fig.2, respectively. The dimensions of the cross section in a duct for mass transfer measurements were 40 x 50 mm (height by width). The test section was 2800 mm long (63 hydraulic diameters in length) to obtain the hydraulically fully developed flow at the mass transfer section. Following the entrance region, a mass transfer development region of 10 x90 mm preceded the cathode (10 x 360 mm) for measurement of average mass transfer coefficients. Further, 1.0 mm platinum point electrodes (30 points) for the measurement of the local mass transfer coefficients, wall shear stress and mass transfer intensity were arranged at intervals of 5 mm on the nickel cathode. Two anodes (17 x 450 mm²) were located on the bottom side of cathode. Each electrode was isolated electrically by epoxy resin. A blunt nose type probe with 0.3 mm platinum wire was used to measure the velocity profile in the duct.

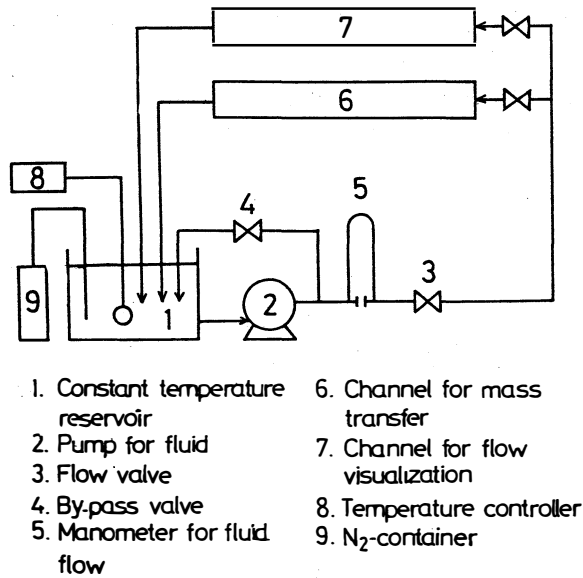


Fig. 1 Schematic diagram of experimental apparatus

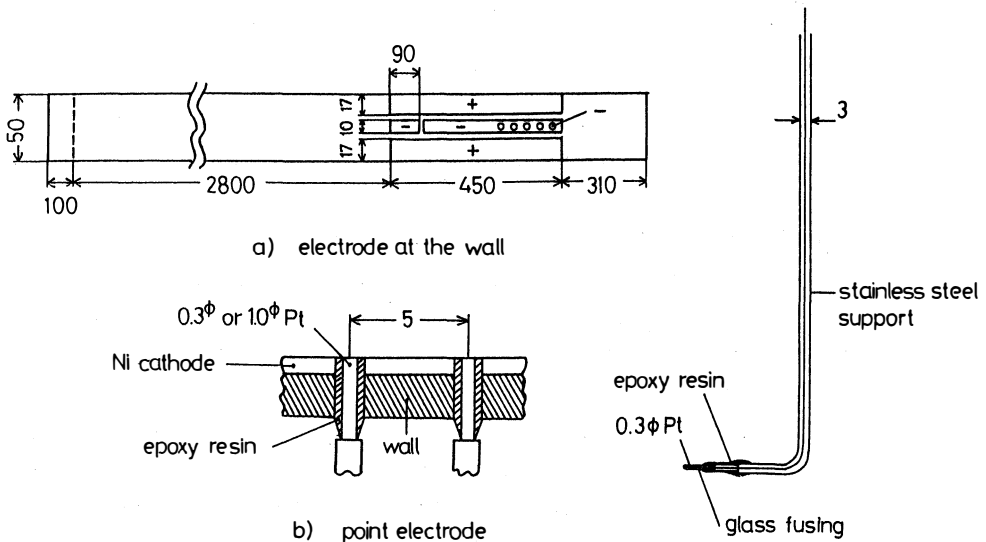


Fig. 2 Details of test section and probe

Experiments were carried out by varying the diameter of turbulence promoters D_p (3, 5, 7 and 10 mm), clearance between the promoter and the wall surface c (0, 1, 3, 5, 7, 10 and centre), pitch among the promoters p ($p/D_p = 5, 7, 9, 12$ and 16) and flow Reynolds number Re ($6.64 \times 10^3 - 1.73 \times 10^4$).

In experiments for the electrochemical method, 0.005M potassium ferri/ferro cyanide and 2M sodium hydroxide used as electrolyte solution. Temperature was set up 303 ± 0.5 K. The density and viscosity of electrolyte were 1075 kg/m^3 and $0.0013 \text{ Pa} \cdot \text{s}$ ($\text{N} \cdot \text{s/m}^2$) respectively. The diffusion coefficient for the ferricyanide ion was $5.776 \times 10^{-10} \text{ m}^2/\text{s}$ given by Mitchell and Hanratty's correlation[21], and the Schmidt number was equal to 2097.

In experiments for visualization, aluminium powder was suspended in water[1]. The flow pattern was observed in a transparent duct. The experimental conditions were similar to those for the measurement of mass transfer.

The coordinates and variables of the test section are shown in Fig. 3 .

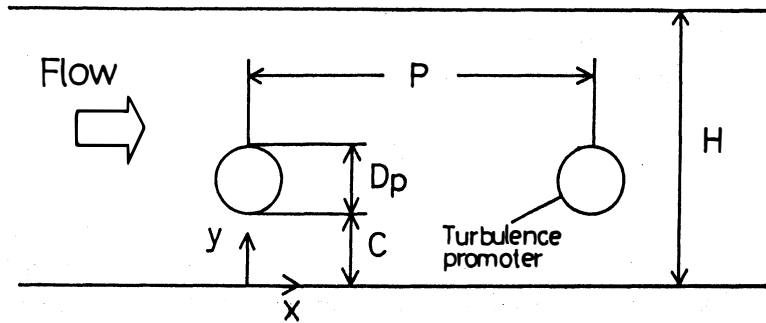


Fig. 3 Coordinates and notations of test section

3. CALCULATION OF TRANSPORT PHYSICAL FACTORS

The mass transfer coefficients were measured by using the potassium ferri/ferrocyanide redox electrochemical reaction as reviewed in detail by Mizushima[15]. The basis of the method is that when operating at the so-called "limiting current" condition the electrochemical phenomena are limited by mass transfer at the cathode only, and hence the concentration of ferricyanide ion is zero at this electrode. Mass transfer limitations do not occur at the anode, if its transfer area is very large relative to that at the cathode. Under these conditions, the mass transfer coefficient is given by

$$k = \frac{i}{n_e \cdot F \cdot A \cdot C_b} \quad (1)$$

To overcome ion-migration effects in a potential field, potassium ferricyanide solution is dissolved in strong electrolyte, in this case sodium hydroxide when the concentration of this unreactive electrolyte is high compared to the concentration of ferricyanide ion, the transfer of ferricyanide ion is done ordinary diffusion or by the ordinary mass transfer mechanism with constant composition at the wall.

The principle of the shear stress and the fluid velocity measurement is also described by Mizushina [15]. The wall shear stress on the bottom wall can be calculated from following the equation in the case of circular surface.

$$\tau = 3.55 \times 10^{-15} \frac{\mu \cdot i}{D^2 \cdot C^3 \cdot d^5} \quad (2)$$

The above equation is given by the solution of Leveque, assuming that the velocity profile is linear and that the Prandtl number of the fluid is large.

The fluid velocity can be calculated by the following equation from limiting current measured by a blunt nose type probe.

$$\mu = (i - \alpha)^2 / \beta^2 \quad (3)$$

where, α and β are constants given by calibration.

Mass transfer intensity is defined by the following equation.

$$I = 100 \frac{\sqrt{k}^2}{k_0} \quad (4)$$

k_0 and k' is calculated from Eq. (1), where \sqrt{k}^2 is the root mean square value for the fluctuating component of mass transfer coefficient. k_0 is the time averaged mass transfer coefficient in a smooth duct. Mass transfer intensity is a transport property to be obtained the information on turbulence close to the wall surface. Electric circuits for the measurements of mass transfer coefficient, the intensity, and fluid velocity using a probe are shown in Fig. 4.

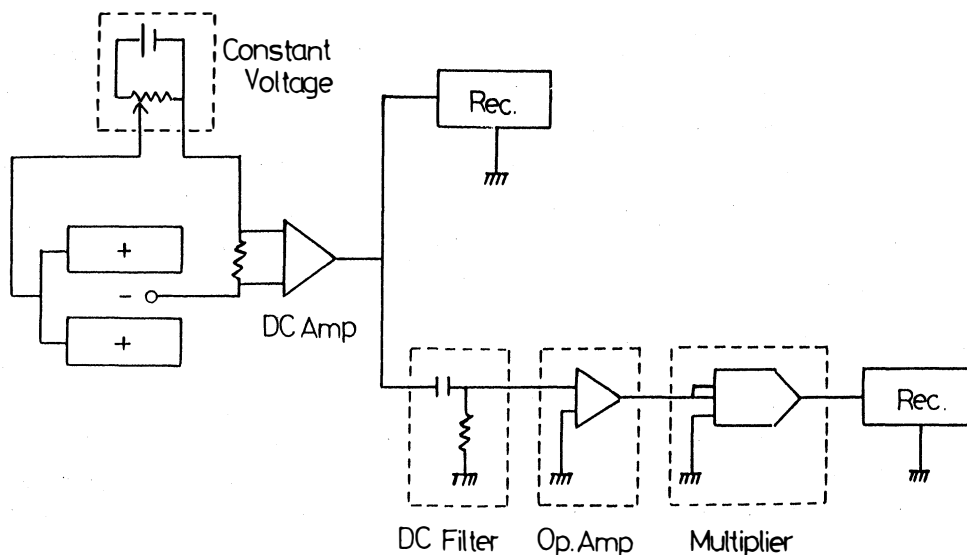


Fig. 4 Electric circuits for measurement of transport factors

4. EXPERIMENTAL RESULTS AND DISCUSSIN

pre-experiment

Before initiating experiments with turbulence promoter, mass transfer coefficient, friction factor and velocity profile were measured for smooth duct as shown in Fig. 5, 6 and 7, and obtained the following correlations, respectively.

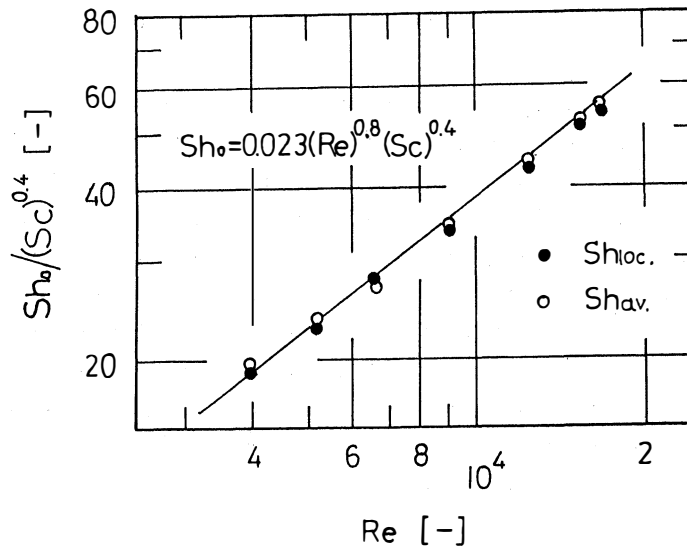


Fig. 5 Mass transfer coefficient for smooth duct

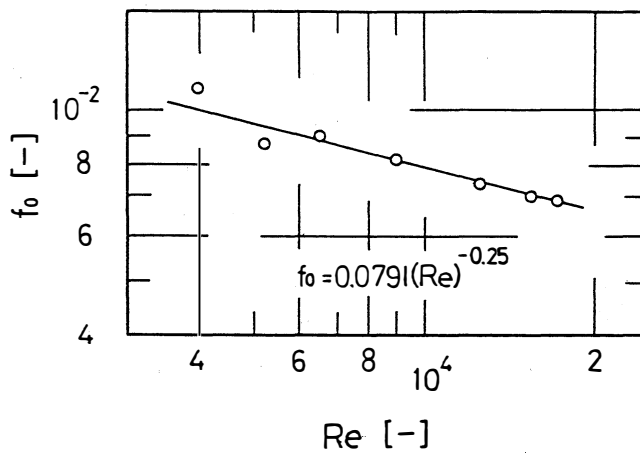


Fig. 6 Friction factor for smooth duct

$$Sh_0 = 0.023 (Re)^{0.8} (Sc)^{0.4} \quad (5)$$

$$f = 0.0791 (Re)^{-0.25} \quad (6)$$

$$u^+ = 5.5 + 2.5 (\ln y^+) \quad (y^+ > 30) \quad (7)$$

where, Re is based on equivalent diameter and in range of $4000 < Re < 18000$. These equations agreed with the classical well known ones within experimental errors.

The experimental equation in turbulent convective heat transfer is

$$Nu = 0.023 (Re)^{0.8} (Pr)^{0.4} \quad (8)$$

$(Re > 8000)$.

With the electrochemical method, mass transfer experiments where the concentration on the wall is zero are similar to those of heat transfer where the temperature on the wall is constant. Analogy between heat and mass transfer is shown by Eq.(4) and (7).

Next, in order to examine the entrance effects in the interval between the turbulence promoters, the distributions of augmentation ratio Sh/Sh_0 of mass transfer among the turbulence promoters were measured for case of $P/Dp=11$, $c=0$ and 3 as shown in Fig. 8. From the data in the figure, it was found that the same distributions were observed downstream from the third promoter. Therefore, the experiment with the promoters was carried out in the section between the third and the fourth promoter, because of safety, though it was reported by the other articles[17, 19] which was repeated in down stream from the second promoter.

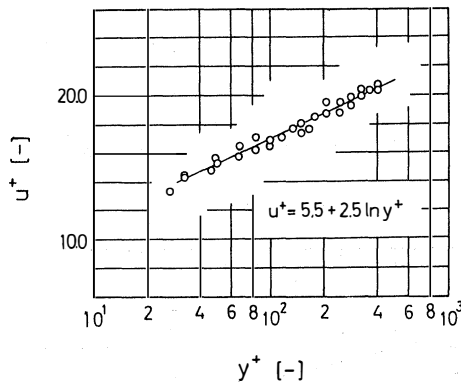


Fig. 7 Velocity profile for smooth duct

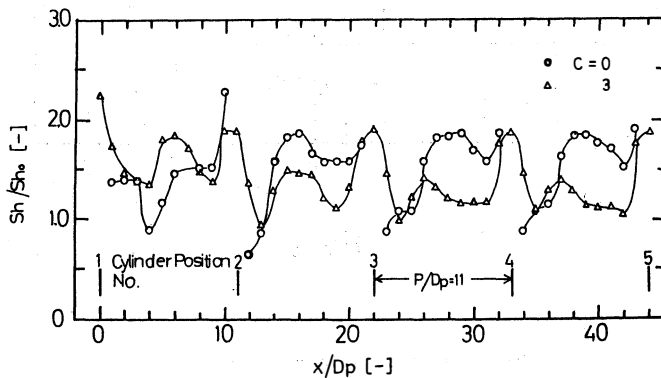


Fig. 8 Check for entrance effect among turbulence promoters

Flow pattern

Flow patterns among the turbulence promoters in turbulent flow for each P/D_p were clearly classified according to the clearance between the promoter and the wall, that is, $c = 1$ and ≥ 3 as suggested by Miyashita [14] for a single promoter in a rectangular duct. Further, the flow pattern was observed by visualization, in order to examine the effect on P/D_p

(1) In the case of $P/D_p = 5$

A typical sketch of the flow pattern with clearance for $P/D_p = 5$ is shown in Fig. 9.

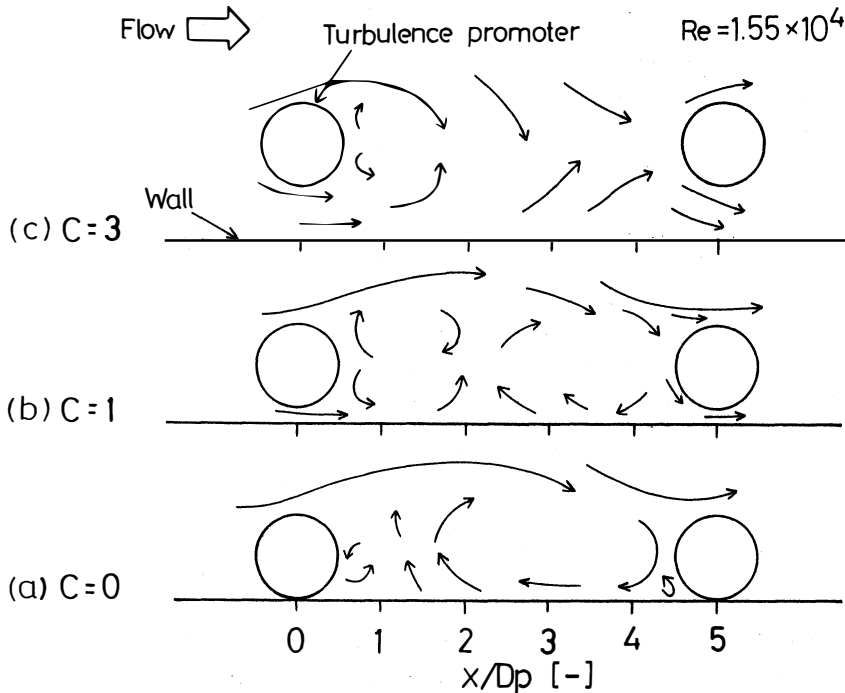


Fig. 9 Flow pattern for $P/D_p = 5$ ($Re = 1.55 \times 10^4$)

$c = 0$:

The flow separated at the top of the promoter was not attached on the wall but collided to the next promoter. It was observed that a part of the flow formed a normal circulating flow among the promoters.

$c = 1$:

A couple of normal and reverse circulating flow was observed in the section between the promoter and $x/D_p = 2 - 4$.

$c = 3$:

A large scale eddy was formed by the combination of the top and the bottom flow of the promoter and Karman's vortex street was formed in back of the promoter as in the experiment [14] for the single promoter.

In generally, the flow in $P/D_p = 5$ seems to stagnate among the promoters because the pitch

of promoters is small and the next promoter is located before the wake flow reaches the attachment point.

(2) In the case of $p/Dp=7$

A typical sketch of the flow pattern with clearance for $p/Dp=7$ is shown in Fig. 10.

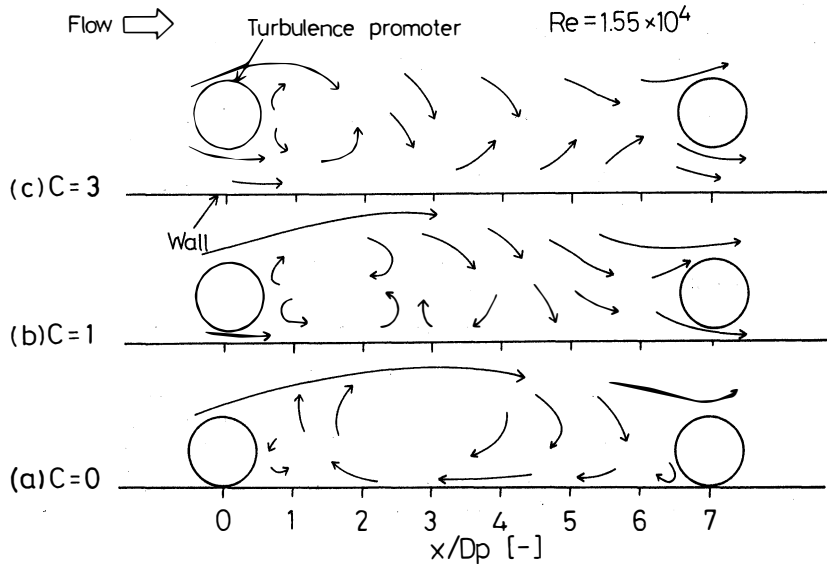


Fig. 10 Flow pattern for $P/Dp=7$ ($Re=1.55 \times 10^4$)

$c=0$:

A part of the separating flow attaches to the wall near $x/Dp=6$ in front of next promoter. The other flow collides with the next promoter, and normal circulating flow is formed among the promoters.

$c=1$:

The top flow of the promoter attaches near $x/Dp=5$ and the bulk flow behavior appears to make violent turbulence before the next promoter.

$c=3$:

Karman's vortex street is formed in the same way as for $p/Dp=5$, and the effect on the wall due to large scale eddies occurring from the top flow of the promoter was observed in the range of $x/Dp=3$ to 4. It is similar to the flow pattern found in experiments for the single promoter. For $c>3$, Karman's vortex street was formed for all p/Dp .

(3) In the case of $p/Dp=9, 11$ and 16

The flow patterns corresponding to clearance c were recognized as the same as for $p/Dp=7$.

In conclusion, it was found that the flow pattern among the promoters distinguished $p/Dp=5$ from $p/Dp \geq 7$, from the behaviors of the separating flow having a direct influence on the augmentation of mass transfer on the wall.

DISTRIBUTION OF LOCAL MASS TRANSFER COEFFICIENT, WALL SHEAR STRESS AND MASS TRANSFER INTENSITY

It may be considered from the flow pattern that the attachment flow and large scale eddies play important roles for the augmentation of mass transfer among the promoters on the wall. In order to discuss the mechanism of this augmentation, local mass transfer coefficients, wall shear stress and mass transfer intensity among the promoters were measured at clearances $c=0, 1$ and 3 , for $p/Dp=5$ and 9 ($p/Dp \geq 7$), as typical examples of flow patterns. The coefficients were expressed as augmentation ratios, Sh/Sh_0 and $|\tau/\tau_0|$, and then correlated with x/Dp .

(1) General tendency

The augmentation ratio of mass transfer Sh/Sh_0 usually has a peak just under the promoter. This peak occurs at the same location as a peak in the absolute value of the shear stress $|\tau/\tau_0|$ and the place of the minimum value of the mass transfer intensity. Therefore, it appears that the augmentation of mass transfer was caused by the thin laminar layer of the accelerated flow under the promoter on the wall. Wall shear stress is an important factor against augmentation of mass transfer only at $x/Dp=0$. Because $|\tau/\tau_0|$ is less than unity in all sections except under the promoter.

(2) In the case of $p/Dp=5$

The profiles of Sh/Sh_0 , $|\tau/\tau_0|$ and I among the promoters are shown in Fig. 11-(a). (b). (c), for $c=0, 1$ and 3 respectively. For $c=0$, the shape of Sh/Sh_0 and I are only increasing to the

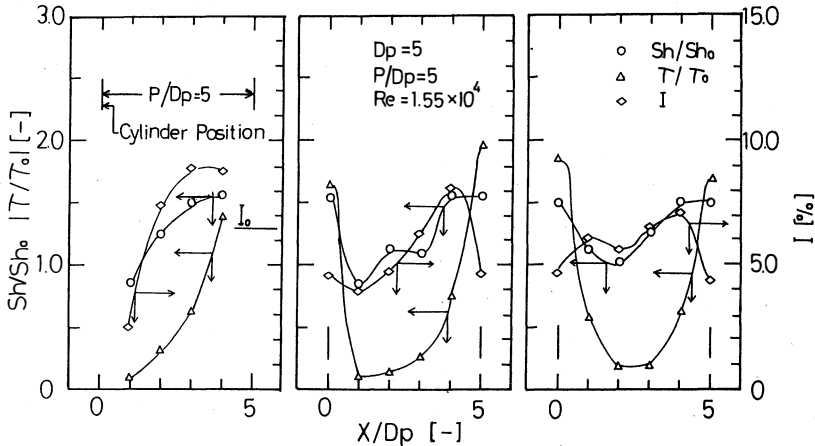


Fig. 11 Profiles of transport factors for $P/Dp=5$

direction of flow and are similar. Therefore, it may be considered that the augmentation of mass transfer is caused by the turbulence due to the circulating eddy formed among the promoters near the wall. For $c=1$ and 3 , both profiles Sh/Sh_0 have minimum values at $x/Dp=1-2$.

Then increasing and approaches the values of Sh/Sh_0 at $x/Dp=0$. These profiles are similar to those of the mass transfer intensity I . Therefore, it was concluded that the augmentation at the wall surface is affected significantly by the turbulence which caused by the separating

flow or Karman's vortex street formed from the first promoter colliding with the next promoter, was caused by a high value in Sh/Sh_0 at $x/Dp=4$.

(3) In the case of $p/Dp=9$

The profiles of Sh/Sh_0 and among the promoters are shown in Fig. 13-(a), (b), (c) with $c=0, 1$ and 3 respectively. For $c=0$, Sh/Sh_0 have a minimum point at $x/Dp=2$ corresponding to at the stagnation point where reversed flow arises. It is some high values in the wide region of

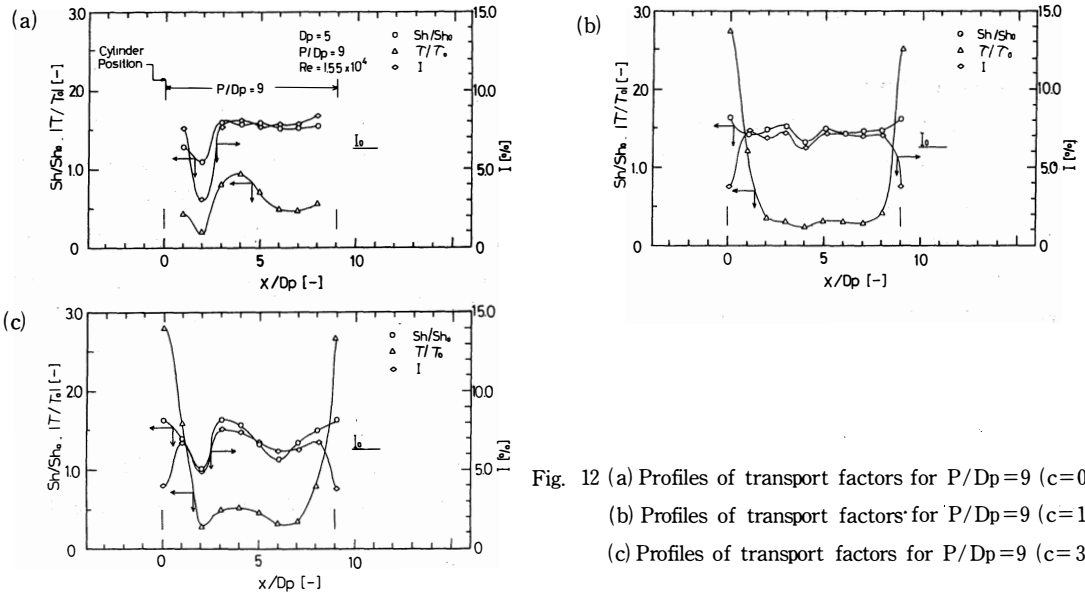


Fig. 12 (a) Profiles of transport factors for $P/Dp=9$ ($c=0$)
 (b) Profiles of transport factors for $P/Dp=9$ ($c=1$)
 (c) Profiles of transport factors for $P/Dp=9$ ($c=3$)

$x/Dp=3 - 8$ and is quite similar to the mass transfer intensity profile. Accordingly, it is recognized that turbulence due to attachment near the wall is a factor in the augmentation of mass transfer.

For $c=1$, Sh/Sh_0 gives a slightly lower value at $x/Dp=4$ but has high values over the whole range except for just under the promoter. This profile is quite similar to the mass transfer intensity. Accordingly, it is recognized that turbulence due to the attachment flow is also a factor for the augmentation of mass transfer.

For $c=3$, Sh/Sh_0 has a peak at $x/Dp=3 - 4$ as in the experiments for a single promoter. The peak corresponds to that of the mass transfer intensity. This means that the augmentation of mass transfer is caused by turbulence from Karman's vortex street in the flow pattern.

CONCLUSIONS

An experimental investigation was performed to study the mechanism for the augmentation of heat transfer due to the cylinder type turbulence promoters on the wall in a rectangular duct. In this paper, an electrochemical method using the redox system of ferri/ferrocyanide ion was used in order to measure the mass transfer coefficient, wall shear stress, fluid velocity and mass transfer intensity. The augmentation mechanism of mass transfer among the promoters was explained through the behaviours of the wall shear stress, the mass transfer intensity and the flow pattern by visualization.

Results were as follows.

It was confirmed that the measurement by electrochemical method was correct from the agreement with well known correlations.

The flow patterns were classified by $p/Dp=5$ and $p/Dp \geq 7$, because of the existence of an attachment point among the promoters, and also classified by the clearance, in $c=0, 1$ and 3 . As c increases, a slipping flow occurs just under the promoter and Karman's vortex street is formed downstream of the promoter for $c \geq 3$ and any p/Dp .

It was found that the attachment flow and large scale eddies play an important role in the augmentation of mass transfer among the promoters through the comparison of profiles of $|\tau/\tau_0|$, I and flow pattern.

$p/Dp=5$: For $c=0$, the augmentation of Sh/Sh_0 depends on the turbulence intensity I . For $c>0$, it depends not only on the increasing $|\tau/\tau_0|$ under the promoter ($x/Dp=0$), but on the turbulence due to large scale eddies among the promoters.

$p/Dp \geq 7$: For $c=0$, it depends on the turbulence due to the attachment flow among the promoters. For $c>0$, it depends not only on the $|\tau/\tau_0|$ under the promoter but also on the turbulence due to attachment flow, circulating eddies and Karman's vortex ($c \geq 3$) among the promoters.

NOTATION

| | | |
|----------------|---|-------------------------|
| A | = surface area of electrode | [cm ²] |
| c | = clearance between turbulence promoter and wall | [mm] |
| c _b | = bulk concentration of ferricyanide ion | [mol/cm ³] |
| D | = diffusivity of ferricyanide ion | [cm ² /s] |
| D _p | = diameter of turbulence promoter | [mm] |
| d | = diameter of point electrode | [mm] |
| F | = Faraday's constant (= 9.652x10 ⁴) | [c/g-equiv.] |
| f | = friction factor | [-] |
| H | = height of rectangular duct | [mm] |
| I | = mass transfer intensity | [%] |
| i | = electric current | [A] |
| k | = mass transfer coefficient | [cm/s] |
| n _e | = valence charge of an ion | [-] |
| p | = pitch of turbulence promoter | [mm] |
| Re | = Reynolds number | [-] |
| Sc | = Schmidt number | [-] |
| Sh | = Sherwood number | [-] |
| u ⁺ | = non-dimensional velocity ($U/(\sqrt{\tau/\rho})$) | [-] |
| U | = mean velocity | [cm/s] |
| u | = free stream velocity | [cm/s] |
| y ⁺ | = non-dimensional distance from wall | [-] |
| x, y | = coordinates of test section | [mm] |
| μ | = viscosity | [pa. s] |

| | | |
|--------|----------------|-------------------------|
| ρ | = density | [g/cm ³] |
| τ | = shear stress | [g/cm. s ²] |

subscripts

o = smoothed duct

LITERATURE CITED

- 1) Asanuma T.: "Hand book of flowvisualization" p.198, Asakura shoten, Tokyo(1977)
- 2) Bergles A.E.: Progr. Heat and Mass Transfer 1,331 (1969)
- 3) Brown W.S., C.C. Pitts and G. Leppert: J. Heat Trans.,84, 133 (1962)
- 4) Fujita H., H. Takahama and R. Yamashita: JSME, 42, 2828(1976)
- 5) Furuya Y., M. Miyata and H. Fujita : Trans. ASME, Journal of Fluid Engineering, Dec., p636 (1976)
- 6) Hanawa J. and Y. Okamoto : Preprint of the 9th Heat Transfer Symp. Japan, p.76 (1972)
- 7) Han J.C., L.R. Gricksman and W.M. Rohsenow: In t. J. Heat Mass Transfer, 21, 1143(1978)
- 8) Igarashi T.: Preprint of the 13th Heat Transfer symp. Japan, p.88(1976)
- 9) Kasagi N., K. Hirata and H. Hiraoka: Preprint of the 14th Heat Transfer Symp., Japan, p.76(1977)
- 10) Kestin J. and R. T. Wood: 4th Int. Heat Transfer Conf., FC 2.7 (1970)
- 11) Konno H., K. Okuda, K. Sasabayashi and S. Ohtani: Kagaku Kogaku, 31, 872 (1967)
- 12) Mabuchi I.: "Netsu Prosesu Kogaku (Heat Process Engineering)", p.1, Ed. The soc. of Chem. Eng., Japan, Maki Shoten (1975)
- 13) Miyashita H., A. Takayanagi, Y. Shiomi and K. Wakabayashi: Kagaku Kogaku Ronbunshu, 6, 153 (1980)
- 14) Miyashita H., Y. Shiomi and K. Wakabayashi: Kagaku Kogaku Ronbunshu, 7, 349 (1981)
- 15) Mizushima T.: "Advances in Heat Transfer" vol. 7, p.87, Academic Press, N. Y. (1971)
- 16) Mori Y. and T. Daikoku: JSME, 38, 832 (1972)
- 17) Okada T. and T. Takeyama: Preprint of the 9th Heat Transfer Symp., Japan, p.443 (1972)
- 18) Oyakawa K. and I. Mabuchi: Preprint of the 16th Heat Transfer Symp., Japan, p.16(1979)
- 19) Oyakawa K. and I. Mabuchi: Preprint of the 17th Heat Transfer Symp., Japan, p.61(1980)
- 20) Rao C. K. and J. J. C. Picot: 4th Int. Heat Transfer Conf., FC 8.4 (1970)
- 21) Reiss L. P. and T. J. Hanratty: A. I. Ch. E. Journal, 8, 245 (1962)
- 22) Reiss L. P. and T. J. Hanratty: A. I. Ch. E. Journal, 9, 154 (1963)
- 23) Sibulkin M.: J. Aeron. Sci., 19, 570 (1952)

This article was originally presented in International Journal of chemical Engineering "chemical Engineering Communication"

(Received October 31, 1984)

Forced Reconnection by Nonlinear Magnetohydrodynamic Waves

J. Sakai

Department of Applied Mathematics and Physics
Faculty of Engineering
Toyama University, Toyama, 930
JAPAN

T. Tajima and F. Brunel
Department of Physics and Institute for Fusion Studies
University of Texas
U. S. A.

ABSTRACT

Forced magnetic reconnection induced by magnetohydrodynamic (MHD) waves may account for the triggering of explosive solar activities such as flares. Reconnection in a neutral sheet plasma can be driven by the ponderomotive force associated with nonlinear MHD waves accompanying plasma vortex motion. The nonlinear stage of forced reconnection by MHD waves is simulated with a MHD particle-code. Some conditions for fast reconnection are discussed with applications to solar flares.

1. INTRODUCTION

Magnetic field reconnection processes (Vasyliunas, 1975; Sonnerup, 1979; Syrovatskii, 1981; White, 1983) may play a significant role in the fast release of magnetic field energy stored in current-carrying plasma such as in a magnetic neutral sheet. They may be important also in the acceleration process of high energy particles. It becomes clear, however, that both the old steady reconnection models by Sweet (1958), Parker (1963) and Petschek (1963) and non-steady reconnection models of tearing modes (Furth, Killeen and Rosenbluth, 1963) are insufficient to explain the impulsive phase of solar flares (Svestka, 1976; Sturrock, 1981) or the sequential triggering phase (Vorpahl, 1976).

The observation (Vorpahl, 1976) hints a mechanism of triggering of solar flares by fast magnetosonic waves. In order to explain the triggering phase of flares, Sakai and Washimi (1982) and Sakai (1983) proposed a theoretical model of forced reconnection caused by fast magnetosonic waves. They showed that the ponderomotive force of fast magnetosonic waves enhances the plasma vortex motion in turn to a rapid growth of forced tearing modes.

Brunel, Tajima and Dawson (1982) showed that the effect of plasma compressibility leads to fast reconnection following Parker's slower reconnection phase. They demonstrated this by computer simulation making use of MHD particle-code (Brunel et al., 1981). Furthermore, in the nonlinear stage of forced tearing instability when magnetic islands are formed, the coalescence instability of magnetic islands may play a most effective role (Leboeuf, Tajima and Dawson, 1982) in the magnetic energy conversion.

About 10% of the magnetic energy stored in the current filaments can be converted into the plasma thermal energy as well as into high energy particles (Tajima, Brunel and Sakai, 1982; Tajima et al., 1983). The quasi-periodic acceleration mechanism (Tajima et al. 1982 and 1983) through relaxation oscillations of two merging current filaments may explain the amplitude oscillations of X-ray, γ -ray and microwave emissions (Forrest et al., 1981; Nakajima et al., 1983).

In the present paper we theoretically discuss the triggering phase in terms of forced reconnection caused by external nonlinear MHD waves, and, moreover, examine and visualize this process by means of a MHD particle simulation. In Section 2, we discuss the nonlinear effect of MHD waves, the ponderomotive force. The threshold condition for external MHD waves to drive the forced reconnection is estimated. In Section 3, we present some simulation results of forced reconnection by nonlinear MHD waves and discuss conditions for fast reconnection. In Section 4, we discuss a situation where the present forced reconnection mechanism by waves may play a significant role to trigger a flare.

2. INITIAL PHASE OF FORCED RECONNECTION BY WAVES

In this section we discuss how fast reconnection is triggered by external MHD waves (fast magnetosonic waves and Alfvén waves). In the initial phase of reconnection forced by nonlinear MHD waves, the magnetic perturbation associated with the reconnection should be small. It is possible then to treat the perturbation associated with reconnection as a linear one. On the other hand, we must take into account nonlinear effects of external MHD waves and also coupling between MHD waves and reconnecting magnetic perturbation. An important nonlinear effect of MHD waves for the neutral sheet can be characterized by a slowly varying ponderomotive force, since the period of the MHD waves is much shorter than the growth time of reconnection. Both fast magnetosonic waves propagating perpendicular to the magnetic field (Sakai and Washimi, 1982; Sakai, 1983) and shear Alfvén waves propagating parallel to the magnetic field (Washimi, 1980) drive plasma vortex motion through their ponderomotive force, as depicted in Figure 1.

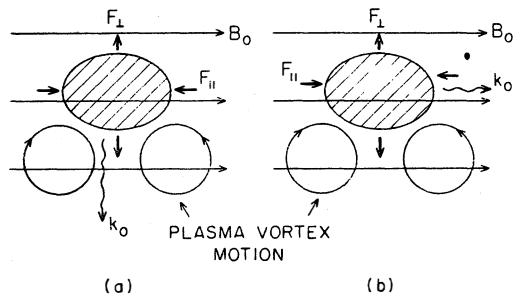


Fig. 1 Schematic plasma vortex motion by ponderomotive forces associated with a wave packet (shaded region) of fast magnetosonic waves (a) and shear Alfvén waves (b).

In a uniform plasma, the ponderomotive force: \vec{F} associated with fast magnetosonic waves and Alfvén waves is described by

$$\begin{aligned} F_{\parallel} &= \rho_0 V_A^2 \nabla_{\parallel} I, \\ F_{\perp} &= -\rho_0 V_A^2 \nabla_{\perp} I, \end{aligned} \tag{1}$$

where F_{11} is the component parallel to the static magnetic field, F_{\perp} the perpendicular component, ρ_0 the background density, V_A the Alfvén velocity and I the normalized wave intensity of MHD waves; $I = |\phi|^2$, where ϕ is the normalized wave amplitude $\delta B / B_{\infty}$ and B_{∞} is the value of B_y at $x = \infty$. This expression shows that $\text{curl } \vec{F} \neq 0$. This suggests that the plasma vortex motion is created by the ponderomotive force (see Figure 2).

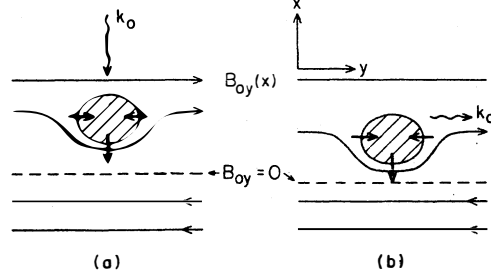


Fig. 2 Finite-amplitude MHD waves propagate (a) across or (b) along the neutral sheet, causing plasma vortex motion, which in turn causes reconnection.

In inhomogeneous plasma (e.g. a neutral sheet plasma and plasma configuration with magnetic shear (Sakai, 1982)), the ponderomotive force has additional terms due to the plasma inhomogeneity. This becomes important for forced excitation of the tearing mode and ballooning mode.

This fast magnetosonic wave-forced reconnection process in its initial phase may be described by the following coupled equations (Sakai and Washimi, 1982):

$$\frac{\partial}{\partial t} \nabla^2 \Pi + \frac{\rho'_0}{\rho_0} \frac{\partial^2 \Pi}{\partial x \partial t} - \frac{B_{0y}}{4\pi\rho_0} \frac{\partial}{\partial y} \left(\nabla^2 A - \frac{B''_{0y}}{B_{0y}} A \right) + \frac{\partial}{\partial y} \left\{ 2(V_A^2 + \frac{V_g^4}{C_s^2}) \frac{\partial I}{\partial x} + 2 \frac{V_g^3}{C_s^2} \frac{\partial I}{\partial t} \right\} = 0, \quad (2)$$

$$\frac{\partial A}{\partial t} = B_{0y} \frac{\partial \Pi}{\partial y} + \frac{C^2}{4\pi\sigma} \nabla^2 A + 2 \frac{\omega}{k} B_{0y} I, \quad (3)$$

where the velocity ($\vec{v} = \text{rot } \Pi \vec{e}_z$) and magnetic perturbations ($\vec{B} = \text{rot } A \vec{e}_z$) are linearized. Here $\nabla^2 = \frac{\partial^2}{\partial x^2} + \frac{\partial^2}{\partial y^2}$ and the prime denotes the derivative with respect to x . B_{0y} is the magnetic field produced by the neutral sheet current. Equation (2) describes the time evolution of plasma vorticity; the last term drives plasma vorticity through the ponderomotive effect.

Equation (3) is the magnetic induction equation.

This set of equations along with the wave kinetic equation for MHD waves self-consistently describes the linear stage of forced reconnection. Forced excitation of tearing modes by magnetosonic waves has been studied (Sakai and Washimi, 1982; Sakai, 1983). The instability grows with a time scale τ given by

$$\tau \simeq 0.2 \tau_A (ka)^{-2} (v_A/v_g)^{4/3} S^{1/3} I_0^{-4/3}, \quad (4)$$

where τ_A is the Alfvén transit time across the current sheet, defined as $\tau_A = a/v_A$ ($v_A = B_{\infty} / \sqrt{4\pi\rho(0)}$), a a thickness of the current sheet, $\rho(0)$ the density at $x=0$, k the wavenumber of the mode, v_g the group velocity of fast waves, $S = \tau_r / \tau_A$ the magnetic Reynolds number,

τ_r the resistive time and I_0 is the wave intensity of fast waves at $x=0$.

This forced tearing mode can be excited if the wave intensity I_0 of the fast waves exceeds a critical value I_c given by

$$I_c = (v_A/v_g)(ka)^{-9/5} S^{-1/5} \quad (5)$$

From Eq. (4), we find two conditions for rapid growth of forced tearing modes:

- (1) when wave intensity is large;
- (2) when ka is large.

Note that $v_A \simeq v_g$ and S is fixed. The second condition indicates that if the external driven fast wave amplitude is modulated locally, we obtain a more rapid growth. The threshold (Eq. (5)) was derived from the condition that the width, $x_s \simeq a(2I_0 v_g / v_A S)^{1/3}$, within which the ponderomotive force is dominant, exceeds the usual resistive thickness layer, $x_r \simeq a(kaS)^{-1/2} (\gamma \tau_r)^{1/4}$.

3. FORCED RECONNECTION OBSERVED IN A COMPUTER SIMULATION

It is difficult to study the nonlinear stage of forced reconnection analytically. Therefore, we present instead the result of a MHD simulation. The purposes in this section are two-fold. The first is to demonstrate the two factors for fast reconnection that were pointed out in the previous section: (1) that the wave amplitude of the external MHD waves exceeds a threshold value; (2) that a local enhancement of the wave amplitude along the y -direction significantly accelerates reconnection. The second purpose is to explore any hidden condition that escapes the analytical approach, predicted in the previous section, playing a vital role in controlling the process of wave-triggered reconnection. In particular we study the effect of the toroidal magnetic field on wave-triggered fast reconnection.

The study of nonlinear development of forced reconnection by simulation is carried out using a MHD particle-code (Brunel et al., 1981). In the MHD particle-code, the equation of motion is solved in Lagrangian coordinates, while the Maxwell equations are solved in Eulerian coordinates, by means of Lax-Wendroff algorithm. The conservation of fluid and momentum is exact.

The density and the magnetic field of the neutral sheet plasma at $t=0$ should satisfy the static pressure balance and the following choice was made:

$$\rho_0 = \rho(x=34\Delta) \operatorname{sech}^2[(x-34\Delta)/a] \quad (6)$$

$$B = B_\infty \tanh[(x-34\Delta)/a] \vec{e}_y + B_t \vec{e}_z \quad (7)$$

where a is the thickness of the current sheet, B_t the toroidal component of the magnetic field and Δ is the grid length. A periodic boundary condition is imposed in the y -direction, while in the x -direction the metallic boundary condition is taken (i.e. $\sigma = \infty$ and $\vec{v} = 0$ on $x = 0$ and 64Δ). The physical parameters used in the simulation are as follows: the magnetic Reynolds number $S = 300 - 2020$, $a = 5\Delta$, the resistivity $\eta = 0.06$ in appropriate normalization of space by Δ and velocity by c_s . In order to excite nonlinear MHD waves far from the neutral sheet, an oscillating external current with frequency $\omega_0 = 2.1, 3.1, 6.2(\Delta c_s^{-1})$ is imposed at $x = 50\Delta$. This option was due to the metallic boundary condition employed in the code where the incoming

wave solution is not allowed.

In order to observe the rate of reconnection, we have computed the destruction of magnetic flux at the X-point as a function of time as shown in Figure 3. Figure 3(a) shows time evolution of the destruction of magnetic flux when the wave amplitude is above a threshold.

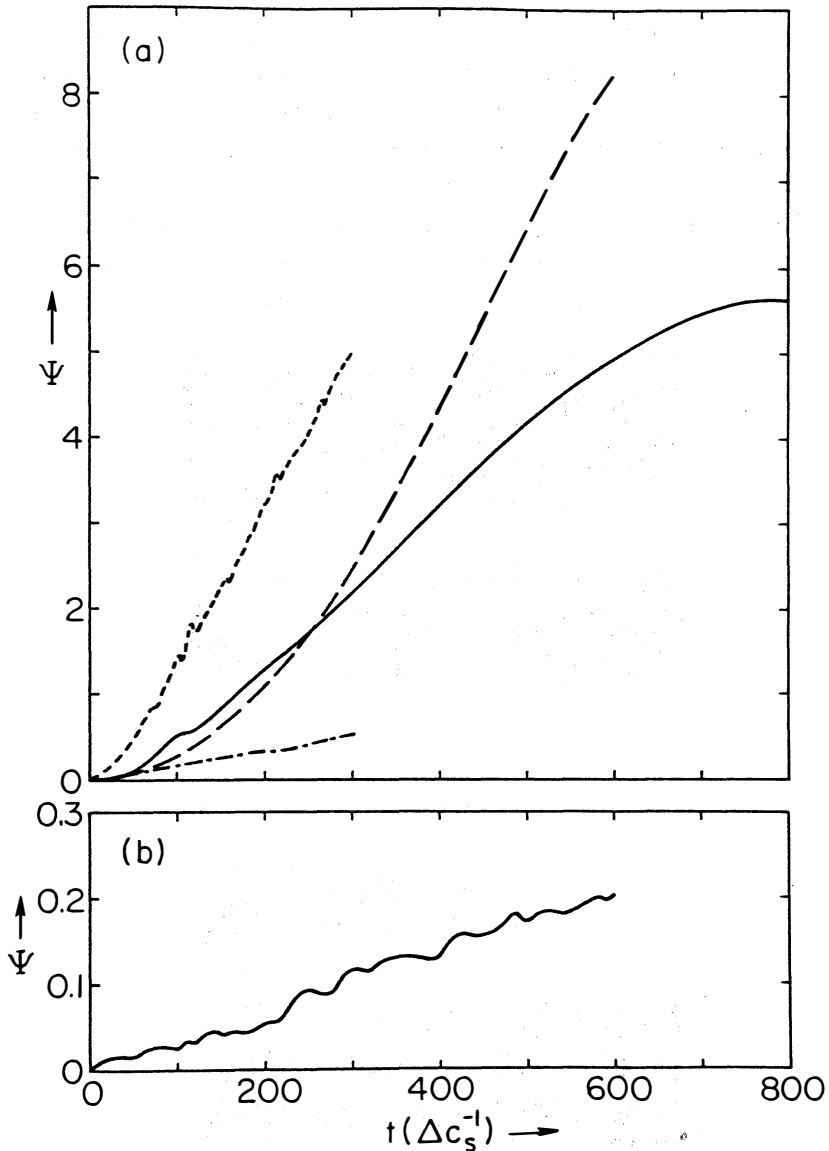


Fig. 3 Reconnecting magnetic flux (ψ) as a function of time

(a) Dash-dotted curve: $B_t / B_\infty = 3$, $S = 2020$.

Solid curve: $B_t / B_\infty = 1.25$, $S = 700$.

Dashed curve: $B_t / B_\infty = 0.625$, $S = 300$.

Dotted curve: $B_t / B_\infty = 1.25$, wave intensity 10 times larger than above three cases. $S = 700$.

(b) No wave: $B_t / B_\infty = 1.25$, $S = 700$.

While Figure 3(b) shows the case when the wave is absent. When the wave amplitude is below a threshold, no fast reconnection is observed as seen in Fig. 3(b). We could not find the threshold of wave amplitude, numerically. We, therefore, discuss only cases above the threshold in the following.

In order to confirm the second condition, i.e. a local enhancement of the wave amplitude along the y -direction, we tried two different cases; (case 1) the external current intensity is constant along the y -direction and (case 2) the current intensity is modulated in the y -direction by superposing two Fourier modes with different wave numbers; $k_1 = 2\pi/128$ and $k_2 = 2\pi/64$, whose amplitudes are 0.0625. In both cases we maintained the intensity of the external waves. In the case(1), we hardly saw reconnection within the length of computer run. Figure 4 shows magnetic field lines in the x - y plane at $t = 300 \Delta c_s^{-1}$ in the case of unlocalized wave simulation. When a local enhancement of the wave amplitude is added with the total wave amplitude kept constant, however, a dramatic acceleration of reconnection took place [case(2)].

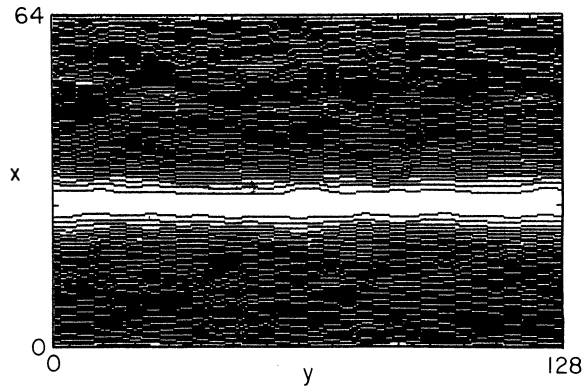


Fig. 4 Unlocalized wave-simulation result at $t = 3000 \Delta c_s^{-1}$. Away from the neutral sheet, the field lines are so dense that they aggregate to look like dark areas, while the neutral sheet region looks light.

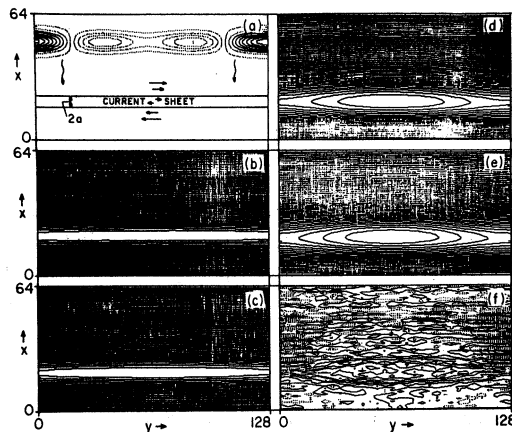


Fig. 5 Simulation results (Localized waves)

- (b) The field line at $t = 120 \Delta c_s^{-1}$.
- (c) The field line at $t = 200 \Delta c_s^{-1}$.
- (d) The field line at $t = 610 \Delta c_s^{-1}$.
- (e) The field line at $t = 800 \Delta c_s^{-1}$.
- (f) The density contours at $t = 625 \Delta c_s^{-1}$. The solid lines are high density regions and the dotted ones are low density regions.

Figure 5 shows the time evolution of magnetic field lines in the x - y plane for the case (2). Reconnection started at the point in the neutral sheet where the amplitude of the external current has a maximum. Figure 5(a) shows the intensity distribution of the external current which was imposed near $x = 50 \Delta$. The amplitude of the external current has a maximum near $y = 124 \Delta$. Therefore the excited MHD waves can be considered to be generated with a maximum amplitude near $y = 124 \Delta$. At the stage of Figure 5(b) we see some modulations in the magnetic field-lines due to the nonlinear MHD waves propagating across the neutral sheet. As shown in Figure 5(d), reconnection occurs at the point where the external MHD waves push the neutral sheet with maximum strength. As reconnection proceeds, the magnetic island grows as shown in Figure 5(e). In Figure 5(f), the density distribution is shown at $t = 625 \Delta c_s^{-1}$. Particles are squeezed near the point where reconnection takes place. The time evolution of reconnecting magnetic flux at the X-point corresponding to Figure 5 is shown by the solid curve in Figure 3(a). The reconnection rate in this case is about 25 times faster than the case of no-wave at $t = 600 \Delta c_s^{-1}$.

We now turn to a new effect of the toroidal magnetic field on fast reconnection. In this series of simulation, we studied wave-triggered reconnection with the toroidal magnetic field B_t (added vertically in the x - y plane) varied. It turns out that the speed of reconnection is much reduced when the toroidal field is applied. Figure 3(a) shows the rate of reconnection for three cases; $B_t / B_\infty = 3$ (dash-dotted curve), $B_t / B_\infty = 1.25$ (solid curve), and $B_t / B_\infty = 0.625$ (dashed curve). When the toroidal field (B_t) is less than the poloidal field (B_∞), fast reconnection takes place. This effect is not explained by the conventional theories including Furth et al. (1963) and Sakai and Washimi (1982). We therefore seem to have found an additional parameter that controls the wave-induced fast reconnection, i.e. the magnitude of the toroidal magnetic field. We attempt to focus on this effect in the following.

Tajima (1981) found the threshold effect of the toroidal field on collisionless reconnection: when the toroidal field is less than the poloidal field, fast reconnection takes place, while no fast reconnection is observed and instead a tearing turbulence occurs when $B_t > B_\infty$. The present simulation of reconnection triggered by impinging MHD waves is consistent with the collisionless reconnection case. Figure 6 shows magnetic field-line reconnection with different toroidal fields; (a) $B_t / B_\infty = 1.25$, (b) $B_t / B_\infty = 3$ at $t = 300 \Delta c_s^{-1}$. When $B_t > B_\infty$, the toroidal field tends to bar rapid reconnection from developing either due to the increased incompressibility of plasma by strong toroidal field or due to the increased magnetization of ions which changes the response of ions to the magnetic perturbation.

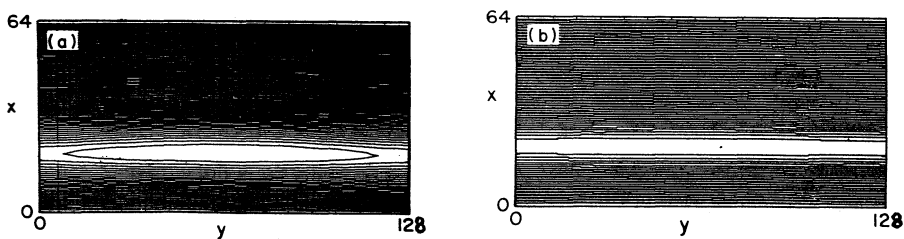


Fig. 6 Comparison of magnetic field-line reconnection with different toroidal magnetic fields ; (a) $B_t / B_\infty = 1.25$ (b) $B_t / B_\infty = 3$, at $t = 300 \Delta c_s^{-1}$.

Summarizing the simulation, for fast reconnection induced by external nonlinear MHD waves, we find:

- (1) A threshold amplitude for the external MHD waves exists.
- (2) Localized wave pressure by nonlinear MHD waves can lead to fast reconnection.
- (3) When there is no toroidal magnetic field, fast reconnection takes place more easily.

As the toroidal field becomes stronger, the reconnection process with waves becomes slower or more difficult.

4. DISCUSSIONS

We now discuss possible mechanisms for MHD waves to localize near the neutral sheet. When a fast magnetosonic wave propagates perpendicular to the magnetic field, the wave becomes unstable against a modulation along the magnetic field, if the amplitude of the fast wave exceeds a critical value, $\phi_m = c_s / v_A$ (Sakai, 1983). This modulational instability can lead to a local enhancement of the wave amplitude.

For the Alfvén wave, local enhancement of the amplitude near the current sheet may be realized by spatial resonance. The external Alfvén waves resonate at the point where the resonance condition, $\omega = k_{\parallel} v_A(x)$, is satisfied (Chen and Hasegawa, 1974). Amplitude enhancement takes place near the resonance when this happens.

The threshold phenomena (Tajima, 1981) for the toroidal magnetic field to control fast reconnection may be important for the magnetic energy storage in the current system of the solar atmosphere. This is because only when the magnetic field B_{∞} produced by the neutral sheet current exceeds the toroidal magnetic field, fast reconnection can set in. This means that as soon as B_{∞} exceeds B_t , an explosive reconnection can take place. This may account for impulsive nature of flares.

The stability of a single current loop (see Van Hoven, 1981) which is tied to the photosphere has recently received attention. In this plasma configuration, the toroidal component of the loop magnetic field changes its sign at a certain radial position in the loop. Nevertheless, the tearing mode may not be excited due to line-tying (Mok and Van Hoven, 1982) in this configuration. Although the resistive interchange instability (Schnack and Killeen, 1981) could still occur, the growth rate is too small to explain the impulsive phase of solar flares for a single current loop. If the nonlinear MHD waves localize near the region where the magnetic field reverses, however, reconnection can occur fast enough through the present mechanism of forced excitation of resistive interchange instability. This may lead to impulsive mass ejection near the photosphere. Of course, when there are more than one loop currents, instead of a single current, the coalescence process (Tajima et al. 1982, 1983) can also play a vital role in facilitating rapid reconnection.

ACKNOWLEDGMENTS

The authors were supported by National Science Foundation Grant ATM 82-14730 and the U.S. Department of Energy Contract DE-FGO5-80ET 53088. A part of this work was performed when one of us (J.S.) was staying at the Physics Department of Texas University at Austin.

REFERENCES

- Brunel, F., Leboeuf, J. N., Tajima, T., Dawson, J. M., Makino, M., and kamimura, T., 1981, *J. Comput. Phys.*, 43, 268.
- Brunel, F. Tajima, T., and Dawson, J.M., 1982, *Phys. Rev. Lett.* 49, 323 .
- Chen, L., and Hasegawa, A., 1974, *Phys. Fluids* 17, 1399 .
- Forrest, D.J., Chupp, E.L., Ryan, J.M., Reppin, C., Rieger, E., Karbach, G., Pinkau, K., Share, G., and Kinzer, G., 1981, in the late volume of the 17th International Cosmic Ray Conference in Paris, France.
- Furth, H.P., Killeen, J., and Rosenbluth, M.N., 1963, *Phys. Fluids* 6, 459 .
- Leboeuf, J.N., Tajima, T., and Dawson, J.M., 1982, *Phys. Fluids* 25, 784 .
- Mok, Y., and Van Hoven, G., 1982, *Phys. Fluids* 25, 636 .
- Nakajima, H., Kosugi, T., Kai, K., and Enome, S., 1983, *Nature* 305, 292
- Parker, E.N., 1963, *Ap. J. Suppl. Ser.* 77, 177 .
- Petschek H.E., 1964, in *Symposium on the Physics of Solar Flares*, ed. by W.H. Hess, NASA, Washington, p. 425 .
- Sakai, J., 1982, *Ap. J.* 263, 970 .
- Sakai, J., 1983, *Solar Phys.* 84, 109 .
- Sakai, J., 1983, *J. Plasma Phys.* 30, 109 .
- Sakai, J., and Washimi, H., 1982, *Ap. J.* 258, 833 .
- Schnack, D.D., and Killeen, J., 1981, *Nucl. Fusion* 21, 1447.
- Sonnerup, B.U.Ö., 1979, in *Solar System Plasma Physics*, ed. C. F. Kennel et al. (Amsterdam: North-Holland), p. 45.
- Sturrock, P.A., 1980, ed. *Solar Flares: A Monograph from Skylab Solar Workshop II* (Boulder, Colorado Assoc. Univ. Press).
- Svestka, z., 1976, *Solar Flares* (Dordrecht, Reidel).
- Syrovatskii, S.I., 1981, *Ann. Rev. Astron. Astrophys.* 19, 163 .
- Sweet, P.A., 1958, *Nuovo Cimento Suppl.* 8 (Ser. 10) 188 .
- Tajima, T., 1982, in *Fusion Energy-1981* (International Centre for Theoretical Physics, Trieste, 1982) p. 403 .
- Tajima, T., Brunel, F., and Sakai, J., 1982, *Ap. J.* 258, L45 .
- Tajima, T., Brunel, F., Sakai, J., Vlahos, L., and Kundu, M.R., 1985, *IAU Symposium No. 107* (D. Reidel Pub. Co.). P. 197.
- Van Hoven, G., 1981, *Solar Flare Magnetohydrodynamics*, (New York, Gordon & Breach), Chapter 4 .
- Vasyliunas, V.M., 1975, *Rev. Geophys. Space Phys.* 13, 303 .
- Vorpahl, J.A., 1976, *Ap. J.* 205, 868 .
- Washimi, H., 1981, *RIA-Report No. 13*, The Research Institute of Atmospherics, Nagoya Univ., Japan.
- White, R.B., 1983, in *Handbook of Plasma Physics*, ed. by M.N. Rosenbluth and R.Z. Sagdeev (Amsterdam, North-Holland).

This paper was presented on 1984 International Conference on Plasma Physics held at Lausanne, Switzerland, June 27–July 3, 1984 and 1984 Plasma Astrophysics/ Course and Workshop held at Varenna, Italy, Aug. 28–Sep. 7, 1984.

(Received October 31 . 1984)

Explosive Transverse Electric Field and Particle Acceleration During Magnetic Collapse

J. Sakai *, T. Tajima **, R. Sugihara ***

* Department of Applied Mathematics & Physics, Faculty of Engineering,
Toyama University, Toyama 930 Japan

** Department of Physics & Institute for Fusion Studies, University of Texas, Austin,
Texas 78712 U. S. A

*** Institute of Plasma Physics, Nagoya University, Nagoya 464 Japan

ABSTRACT

It is shown that ion streams across the magnetic field moving with electrons cause explosive transverse electrostatic field during magnetic collapse such as coalescence instability of current loops. The electrostatic field can explosively accelerate ions and electrons perpendicular both to the magnetic field and ion streams. Ions and electrons are almost simultaneously accelerated to the opposite direction, respectively. The results obtained here well explain the simulation results of collisionless coalescence instability of current loops. The simultaneous acceleration mechanism of ions and electrons is applied to the origin of explosive high energy particles in cosmic plasmas.

Keywords: Particle Acceleration, Explosive Transverse Electrostatic Field, Magnetic Collapse, Coalescence Instability, Solar Flare

1. INTRODUCTION

The acceleration mechanisms of charged particles to suprathermal energies in cosmic plasmas are of fundamental importance. A various kinds of acceleration mechanisms¹⁾ in the use of electric and magnetic fields in plasmas are proposed in connection with specific examples of observed high energy particles since the Fermi-type acceleration.

Recent observations²⁾ of solar flares showed that in the impulsive phase ions and electrons can be almost simultaneously accelerated within a few seconds in a quasi-periodic manner. This observation implies the improvement of widely accepted stochastic acceleration of particles.

Tajima et al.³⁾ explained the quasi-periodic acceleration of ions and electrons by nonlinear coalescence instability of two parallel current loops. In their computer simulation of the coalescence instability they showed the existence of strong explosive electrostatic field across the magnetic field which may cause the production of high energy ions and electrons.

Sugihara et al.⁴⁾ found a mechanism ($\vec{V}_p \times \vec{B}$ acceleration) of charged particles trapped by strong electrostatic waves propagating across the magnetic field. In the present paper we show theoretically the existence of explosive electrostatic field across the magnetic field moving with magnetized electrons during magnetic field collapse such as the coalescence instability of current loops. The transverse electrostatic field grows explosively with a velocity relative to the mag-

nitic field. The charged particles (ions and electrons) driven by the electrostatic field can be accelerated in the direction perpendicular both to the magnetic and electric field. This acceleration mechanism is thought to be an extension of $\vec{V}_P \times \vec{B}$ acceleration.

2. BASIC EQUATIONS FOR 1-D MODEL OF MAGNETIC COLLAPSE

In this section we present basic equations for one dimensional model of magnetic collapse such as coalescence instability of current loops. Before complete merging state of current loops ion streams across the poloidal magnetic field \vec{B} produced by the loop current \vec{J} itself are driven by $\vec{J} \times \vec{B}$ force. For simplicity we choose the direction of ion streams as x-coordinate and the poloidal magnetic field as y-coordinate, while the loop currents flow in the z direction. We assume that all physical quantities depend only on the x-coordinate (1-D model of magnetic collapse). During magnetic collapse besides complete merging state of two current blobs the pressure effect of plasmas are negligible compared with the Lorentz forces.

We start from two fluid equations of plasmas, neglecting the pressure terms as well as displacement current in the Maxwell equation. We obtain the following equations for electron fluid:

$$\frac{\partial n_e}{\partial t} + \frac{\partial}{\partial x}(n_e v_{ex}) = 0, \quad (1)$$

$$\frac{\partial v_{ex}}{\partial t} + v_{ex} \frac{\partial}{\partial x} v_{ex} = -\frac{e}{m_e} \left(E_x - \frac{v_{ez}}{c} B_y \right), \quad (2)$$

$$\frac{\partial v_{ez}}{\partial t} + v_{ex} \frac{\partial}{\partial x} v_{ez} = -\frac{e}{m_e} \left(E_z + \frac{v_{ex}}{c} B_y \right). \quad (3)$$

As the ions flow almost across the magnetic field because of $J_z \times B_y$ force, we may treat ions as unmagnetized fluid i.e. we neglect the term $eB_y v_{iz}/c$ compared with eE_x in the ion equation of motion. Therefore we obtain the following equations for ion fluid:

$$\frac{\partial n_i}{\partial t} + \frac{\partial}{\partial x}(n_i v_{ix}) = 0, \quad (4)$$

$$\frac{\partial v_{ix}}{\partial t} + v_{ix} \frac{\partial}{\partial x} v_{ix} = \frac{e}{m_i} E_x, \quad (5)$$

$$\frac{\partial v_{iz}}{\partial t} + v_{ix} \frac{\partial}{\partial x} v_{iz} = \frac{e}{m_i} \left(E_z + \frac{v_{ix}}{c} B_y \right). \quad (6)$$

Equations (1)–(6) are closed by the Maxwell equations,

$$\frac{\partial B_y}{\partial t} = c \frac{\partial E_z}{\partial x}, \quad (7)$$

$$\frac{\partial E_x}{\partial x} = 4\pi e(n_i - n_e), \quad (8)$$

$$v_{ez} = -\frac{c}{4\pi e n_e} \frac{\partial B_y}{\partial x}, \quad (9)$$

where we assumed that current in the z -direction can be maintained only by electrons in Eq. (9).

We try to seek local solutions of Eq.(1)–(9) representing magnetic collapse, where there is no definite scale-length i. e. the scale-length characterizing a distance between two current loop may continuously vary in time during magnetic collapse. Such a physical situation may be well described by self-similar solutions, in which scale factors $a(t)$ and $b(t)$ varying continuously in time are introduced as follows,

$$v_{ex} = \frac{\dot{a}}{a} x, \tag{10}$$

$$v_{ix} = \frac{\dot{b}}{b} x, \tag{11}$$

where the linear dependence on x means the fact that ion and electron streams are flowing in the opposite direction around $x=0$, which is the center of two current loops. In Eq. (10) and (11) \dot{a} and \dot{b} mean the time derivative. The unknown scale factors a and b will be determined from the above basic equations. From the continuity equations (1) and (4), we obtain

$$n_e = n_0 / a, \tag{12}$$

$$n_i = n_0 / b, \tag{13}$$

where n_0 is a constant. Equations(12)and(13) show that the density of ions and electrons is homogeneous in space and varies only in time during magnetic collapse. It is reasonable to assume that the poloidal magnetic field may have linear dependence on x as $B_y = B_0(t) x/\lambda$, because the poloidal magnetic field reverses its sign at $x=0$. λ is a characteristic length of magnetic inhomogeneity. Above poloidal magnetic field means that the current along z -direction is constant in the range of λ .

From Eqs.(7) and (9) we obtain

$$E_z = \frac{\dot{B}_0(t) x^2}{2\lambda c} + E_{z0}(t), \tag{14}$$

$$v_{ez} = -\frac{ca(t) B_0(t)}{4\pi en_0 \lambda}. \tag{15}$$

Substituting Eqs.(10),(14) and (15) into Eq.(3), we found

$$B_y = \frac{B_{00} x}{a^2 \lambda}, \tag{16}$$

$$E_z = -\frac{B_{00} \dot{a} x^2}{ca^3 \lambda} - \frac{B_{00} c m e \dot{a}}{4\pi n_0 e^2 \lambda a^2}, \tag{17}$$

$$v_{ez} = -\frac{c B_{00}}{4\pi en_0 \lambda a}. \tag{18}$$

Assuming the electrostatic field E_x as $E_x = E_0(t) x/\lambda$ and making use of Eqs. (2), (5) and (8), we found

$$\frac{\dot{b}}{b} = \frac{e E_0}{m_i \lambda}, \tag{19}$$

$$\frac{\ddot{a}}{a} = -\frac{eE_0}{m_e\lambda} - \frac{B_{00}^2}{4\pi n_0 m_e \lambda^2 a^3}, \quad (20)$$

$$E_0 = 4\pi e n_0 \lambda \left(\frac{1}{b} - \frac{1}{a} \right). \quad (21)$$

Finally we obtain the coupled nonlinear equations for $a(t)$ and $b(t)$ from above equations;

$$\ddot{a} = -\omega_{pe}^2 \left(\frac{a}{b} - 1 \right) - \frac{B_{00}^2}{4\pi n_0 m_e \lambda^2 a^2}, \quad (22)$$

$$\ddot{b} = \omega_{pi}^2 \left(1 - \frac{b}{a} \right), \quad (23)$$

where $\omega_{pe}^2 = \frac{4\pi n_0 e^2}{m_e}$, and $\omega_{pi}^2 = \frac{4\pi n_0 e^2}{m_i}$.

3. EXPLOSIVE ELECTROSTATIC FIELD DURING MAGNETIC COLLAPSE

In the previous section we derived basic equations (22) and (23) describing one-dimensional magnetic collapse. In Eqs. (22) and (23) the two first terms of right hand sides represent the effect of charge separation. While the second term of Eq. (22) comes from the force $\mathbf{J}_z \times \mathbf{B}_y$, which can drive magnetic collapse. When this driving term is dominant, it is good approximation to assume quasi-neutrality ($n_i = n_e$) which means $a = b$. This was confirmed by the numerical calculation of Eq. (22) and (23). In a quasi-neutral plasma we obtain the following equation for a from the summation of Eqs. (19) and (20),

$$\ddot{a} = -\frac{v_A^2}{\lambda^2 a^2}, \quad (24)$$

where $v_A^2 = B_{00}^2 / 4\pi n_0 (m_i + m_e)$.

The equation (24) is similar to the gravitational collapse in the Newtonian dynamics of a large gas cloud. The solution of Eq. (24) representing magnetic collapse is given by

$$a(t) = \alpha (t_0 - t)^{2/3}, \quad (25)$$

where α is given by $\alpha = \left(\frac{9}{2} \right)^{1/3} (v_A/\lambda)^{2/3}$ and t_0 is an explosion time.

The electrostatic field can be determined from Eq. (19), not from the Poisson equation (21) as

$$\begin{aligned} E_0(t) &= \frac{m_i \lambda}{e} \frac{\dot{a}}{a} \\ &= -\frac{m_i v_A^2}{\lambda e a^3}, \end{aligned} \quad (26)$$

By means of the solution (25) we obtain various kinds of physical quantities as follows;

$$v_{ex} = v_{ix} = -\frac{2}{3} \frac{x}{(t_0 - t)}, \quad (27)$$

$$n = n_i = n_e = \left(\frac{2}{9} \right)^{1/3} \frac{\lambda^{2/3} n_0}{v_A^{2/3} (t_0 - t)^{2/3}}, \quad (28)$$

$$E_x = -\frac{2}{9} \frac{m_i}{e} \frac{x}{(t_0 - t)^2}, \quad (29)$$

$$B_y = \left(\frac{2}{9} \right)^{2/3} \frac{B_{00} \lambda^{1/3} x}{v_A^{4/3} (t_0 - t)^{4/3}}, \quad (30)$$

$$E_z = \frac{2}{3} \left(\frac{2}{9} \right)^{2/3} \frac{B_{00} \lambda^{1/3} x^2}{v_A^{4/3} c (t_0 - t)^{7/3}} + \frac{2}{3} \left(\frac{2}{9} \right)^{1/3} \frac{B_{00} c}{\omega_{pe}^2 \lambda^{1/3} v_A^{2/3} (t_0 - t)^{5/3}}, \quad (31)$$

We found that during magnetic collapse the electromagnetic fields can grow explosively in time as seen from above relations. Particular interest in above solutions is that the explosive transverse electrostatic field E_x can grow faster than the magnetic field B_y , because of the fast explosiveness in time i.e. $E_x \propto (t_0 - t)^{-2}$, $B_y \propto (t_0 - t)^{-4/3}$ in the limit of $t \rightarrow t_0$. From this fact we may expect the particle acceleration driven by the electrostatic field as well as $V_x \times B_y$ acceleration in the z -direction. In the next section we examine the particle acceleration under the above explosive electromagnetic fields during magnetic collapse.

4. SIMULTANEOUS ACCELERATION OF IONS AND ELECTRONS DURING MAGNETIC COLLAPSE

In this section we examine a test particle motion under the explosive electromagnetic fields during magnetic collapse given in the previous section. The equations of motion of a test ion are given by

$$\frac{dv_x}{dt} = -\frac{eE_{x0}}{m_i} \frac{x}{(t_0 - t)^2} - \frac{eB_{y0} x v_z}{m_i c (t_0 - t)^{4/3}}, \quad (32)$$

$$\frac{dv_z}{dt} = \frac{eE_{z0}}{m_i} \frac{x^2}{(t_0 - t)^{7/3}} + \frac{9eE_{z0} c^2 v_A^{2/3}}{2m_i \lambda^{2/3} \omega_{pe}^2 (t_0 - t)^{5/3}} + \frac{eB_{y0}}{m_i c} \frac{x \dot{x}}{(t_0 - t)^{4/3}}, \quad (33)$$

where $E_{x0} = 2m_i/9e$, $E_{z0} = \frac{2}{3} \left(\frac{2}{9} \right)^{2/3} \frac{B_{00} \lambda^{1/3}}{c v_A^{4/3}}$,

and $B_{y0} = \left(\frac{2}{9} \right)^{2/3} \frac{B_{00} \lambda^{1/3}}{v_A^{4/3}}$.

Transforming the time t to τ by $\tau = t_0 - t$, we obtain

$$\frac{dv_x}{d\tau} = -\frac{eE_{x0}}{m_i} \frac{x}{\tau^2} - \frac{eB_{y0}}{m_i c} \frac{x v_z}{\tau^{4/3}}, \quad (34)$$

$$\frac{dv_z}{d\tau} = -\frac{eB_{y0}}{m_i c} \left[\frac{2}{3} \frac{x^2}{\tau^{7/3}} + \frac{\Delta}{\tau^{5/3}} - \frac{x}{\tau^{4/3}} \frac{dx}{d\tau} \right], \quad (35)$$

where $\Delta = 9 c^2 v_A^{2/3} / 2 \omega_{pe}^2 \lambda^{2/3}$ and we used the relation $E_{z0} = 2B_{y0} / 3c$ in Eq. (35).

Here we take particular attention to the ion which can be almostly accelerated by the transverse electrostatic field E_x across the magnetic field. This ion can be accelerated without gyration. The equation of this ion is approximately given by

$$\frac{dv_x}{d\tau} = -\frac{eE_{x0}}{m_i} \frac{x}{\tau^2}, \quad (36)$$

because of $eE_x \gg ev_z B_y / c$.

The solution of Eq. (36) is given by

$$x = c_1 \tau^{2/3} + c_2 \tau^{1/3}, \quad (37)$$

$$v_x = \dot{x} = \frac{2}{3} c_1 \tau^{-1/3} + \frac{1}{3} c_2 \tau^{-2/3}, \quad (38)$$

where c_1 and c_2 are determined from initial conditions,

$$\left. \begin{aligned} c_1 &= 3(v_0 t_0^{1/3} - x_0 t_0^{-2/3}), \\ c_2 &= 3(x_0 t_0^{-1/3} - v_0 t_0^{2/3}), \end{aligned} \right\} \quad (39)$$

The equation (38) shows that the ion for nonzero c_1 and c_2 can be explosively accelerated in the x -direction. By means of the solutions (37) and (38) we find the solution for v_z from Eq. (35)

$$v_z = \frac{eB_{y0}}{m_i c} \left(\frac{c_1^2 + 3\Delta}{2\tau^{2/3}} + \frac{c_1 c_2}{\tau^{1/3}} \right), \quad (40)$$

which shows that the ion for a particular initial condition, i.e. $c_2 \neq 0$ can be explosively accelerated in the z -direction. The dominant term in Eq. (40) is the first term including c_2 in the limit of $\tau \rightarrow 0$. The solution (40) also shows that ions and electrons can be accelerated in the opposite direction each other, because v_z is proportjional to the sign of the charge e . Actually we obtain for a test electron

$$v_{ez} = -\frac{eB_{y0}}{m_e c} \left\{ \frac{d_1^2}{2} \tau^{\mu-2/3} + \frac{3}{2} \Delta \tau^{-2/3} + d_1 d_2 \tau^{-1/3} + \frac{d_2^2}{2} \tau^{-\mu-1/3} \right\}, \quad (41)$$

where

$$\left. \begin{aligned} \mu &= (1 + 8m_i / 9m_e)^{1/2}, \\ d_1 &= \mu^{-1} \left[v_0 t_0^{\frac{1-\mu}{2}} - \frac{(1-\mu)}{2} x_0 t_0^{-\frac{1+\mu}{2}} \right], \\ d_2 &= \mu^{-1} \left[\frac{(1+\mu)}{2} x_0 t_0^{\frac{\mu-1}{2}} - v_0 t_0^{\frac{1+\mu}{2}} \right]. \end{aligned} \right\}$$

The main term in Eq. (41) is the last one, which shows that the electron with nonzero d_2 can be explosively accelerated in the opposite direction compared with the ion.

The above acceleration can continue until the Lorentz force $v_z B_y / c$ exceeds the electrostatic force. The ion with $\Delta \ll c_2^2 \leq (v_A^{8/3} / 2 \omega_{pi}^2 \lambda^{2/3})$ can be accelerated until the explosion time $t =$

t_0 , because the electrostatic force always exceeds the magnetic force $v_z \times B_y$. On the other hand, the electron can be detrapped from the electrostatic field at $\tau = \tau_A$ before the explosion time,

$$\tau_A = \left[\frac{2}{d_z^2} \left(\frac{eE_{x0}}{m_e} \right) \left(\frac{eB_{y0}}{m_e c} \right)^{-2} \right]^{\frac{3}{1-3\mu}} \quad (42)$$

At $\tau = \tau_A$ the electron can gain the maximum velocity v_{ze}^{\max} ,

$$\begin{aligned} v_{ze}^{\max} &= -\frac{d_z^2}{2} \left(\frac{eB_{y0}}{m_e c} \right) \tau_A^{-\mu - \frac{1}{3}} \\ &= -\frac{d_z^2}{2} \left(\frac{eB_{y0}}{m_e c} \right) \left[\frac{2}{d_z^2} \left(\frac{eE_{x0}}{m_e} \right) \left(\frac{eB_{y0}}{m_e c} \right)^{-2} \right]^{\frac{-1-3\mu}{1-3\mu}} \end{aligned} \quad (43)$$

The explosiveness ($v_{ez} \propto \tau^{-\mu - \frac{1}{3}}$) of electron acceleration in the z-direction is stronger than that of ion acceleration ($v_{iz} \propto \tau^{-2/3}$). Anyway ions and electrons can be almost simultaneously accelerated during magnetic collapse.

5. SUMMARY

We found that ion streams across the collapsing magnetic field can generate explosive electromagnetic fields. The transverse electrostatic field can grow faster than the magnetic field. The ions and electrons can be almost simultaneously accelerated in the opposite direction along the current flow each other. The computer simulation of collisionless coalescence instability showed³⁾ all above features. The dynamical magnetic collapse may occur in every plasma of astrophysical interest. The magnetic collapse can be driven in a system of many current loops such as in active star atmosphere. It may also be driven in accretion disk with magnetized plasma by strong gravitational force. The explosive acceleration of high energy particles can be observed during such magnetic collapse.

REFERENCES

1. Arons, J., Max, C. and McKee, C. Eds. 1979; *Particle Acceleration Mechanisms in Astrophysics*, American Institute of Physics.
2. Kulsrud, R.M. 1981, *Particle Acceleration in Plasma Astrophysics*, esp. pp-161, 105.
3. Forrest, D.J. et al. 1981, 17th *Inter. Cosmic Ray Conf.* 10, 5, .
Forrest, D.J. and Chupp, E.L. 1983, *Nature Letters* 305, 291.
4. Tajima, T., Brunel, F. and Sakai, J. 1982, *Ap. J.* 258, L45.
Tajima, T., Brunel, F., Sakai, J., Vlahos, L., and Kundu, M.R. 1985, *IAU Symposium No. 107*. P. 197.
Nakajima, H., Tajima, T., Brunel, F., and Sakai, J. 1984, *this issue*. P. 39.
5. Sugihara, R., and Midzuno, Y. 1979, *J. Phys. Soc. Jpn.* 47, 2 1290.
Dawson, J.M. et al. 1983, *Phys. Rev. Lett.* 50, 1455.

This paper was presented on 1984 Plasma Astrophysics/Course and Workshop held at Varenna, Italy.

(Aug. 28-Sep. 7, 1984)

(Received. October. 31. 1984)

Signatures of the Coalescence Instability in Solar Flares

H. Nakajima*

Laboratory for Astronomy and Solar Physics, NASA Goddard Space Flight Center

T. Tajima and F. Brunel

Department of Physics and Institute for Fusion Studies, University of Texas

J. Sakai

Department of Applied Mathematics and Physics, Faculty of Engineering,

To y a m a U n i v e r s i t y

ABSTRACT

Double sub-peak structures in the quasi-periodic oscillations found in the time profiles of two solar flares on 1980 June 7 and 1982 November 26 are well explained in terms of the coalescence instability of two current loops. This interpretation is supported by the observations of two microwave sources and their interaction for the November 26 flare. The difference of both sub-peak structures and time scales between the two flares are discussed from the viewpoint of different plasma parameters in our computer simulations.

I. INTRODUCTION

Recent observations of X-ray continuum emission, γ -ray line, and continuum emission from solar flares with instruments on the Solar Maximum Mission (SMM) and Hinotori satellites show that energetic ions and relativistic electrons are accelerated almost simultaneously with non-relativistic electrons during the impulsive phase of solar flares. These observational results make it necessary to revise the widely accepted hypothesis of particle acceleration that energetic ions and relativistic electrons are produced in the second phase a few minutes after the impulsive phase (Wild et al. 1963; de Jager 1969; Svestka 1976). Although Bai and Ramaty (1979), Bai (1982), and Bai et al. (1983) revised the hypothesis as the second-step acceleration taking note of a small delay of γ -ray line emission from hard X-ray emission, Kane et al. (1983), and Forrest and Chupp (1983) pointed out that such a small delay can be explained simply by either the injection, propagation, or energy loss processes of particles which are accelerated in a single step.

Tajima et al. (1982, 1983) proposed a simultaneous acceleration mechanism of protons and electrons in solar flares by the nonlinear coalescence instability of two current loops, based on the results of computer simulation. Two adjacent, parallel current loops are unstable against the coalescence instability which involves the rapid (sometimes explosive) conversion of magnetic energy to kinetic energy of particles (Tajima 1982). The results of computer simulation reve-

*NASA/NRC resident research associate from Nobeyama Solar Radio Observatory of Tokyo
Astronomical observatory.

aled that the time profiles of the proton and electron temperatures show quasi—periodic oscillations with double sub—peak structures.

Recently Nakajima et al. (1983) and Kiplinger et al. (1983) reported observations of quasi—periodic pulses with double sub—peak structure seen in hard X—ray, γ —ray, and microwave emissions in the two intense solar flares of 1980 June 7 and 1980 June 21. We are interested in the close similarity between the observed time profiles and those obtained with the computer simulation by Tajima et al.

In this letter, we present the results of our analysis of the 1980 June 7 and 1982 November 26 events, both of which show double sub—peak structures in quasi—periodic oscillations. Since these two events are widely different from each other in duration, source size, source height, etc., they provide a stringent test for examining the validity of our model of particle acceleration in solar flares in terms of the coalescence instability. Our study shows that observational features of the two events are consistent with the results of our computer simulation.

II. SUMMARY OF OBSERVATIONS

(a) 1980 June 7 Event

The impulsive burst of the 1980 June 7 solar flare (Figure 1) has been investigated by many authors (Forrest et al. 1981; Kane et al. 1983; Forrest and Chupp 1983; Nakajima et al. 1983; Kiplinger et al. 1984). We summarize below some essential points from these observations.

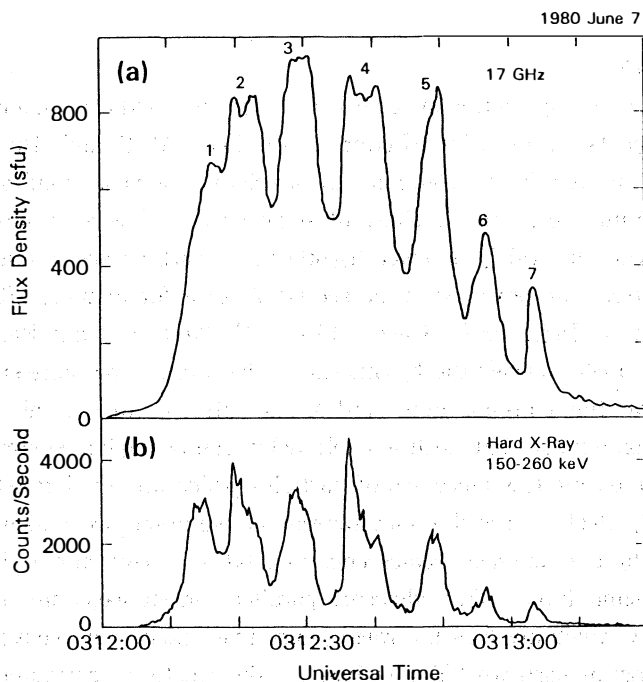


Figure 1: Time profiles of the 17 GHz microwave emission and the 150–260 keV X-ray emissions (from HXRBS) for the 1980 June 7 event.

- (1) The burst is composed of seven successive pulses with a quasi-periodicity of about 8 seconds. Each of the pulses in hard X-rays, prompt γ -ray lines, and microwaves is almost synchronous and similar in shape.
- (2) The microwave pulses consist of double sub-peaks as seen especially in the second and fourth pulses in Figure 1(a). The double sub-peak structure is also evident in the hard X-ray time profiles (Figure 1(b)).
- (3) The starting times of hard X-rays, prompt γ -ray lines, and microwaves coincide within ± 2.2 seconds.
- (4) The time scales of accelerations for both electrons (up to energies above 1 MeV) and ions (above 10 MeV/nucleon) are less than 5 seconds. And the accelerations must occur almost simultaneously.
- (5) The height of the microwave source is estimated to be within 10 arc sec above the photosphere ($H\alpha$ flare; $N12^\circ, W74^\circ$). The source has a small size of less than 5 arc sec in the east-west direction and shows no motion.

The $H\alpha$ photographs from the Peking Observatory (H. Chow, private communication) add a new finding. The flaring region has two structures that appear to be in contact with each other, one stretching in the east-west direction and the other in the north-south.

(b) 1982 November 26 Event

We briefly outline the characteristics of the 1982 November 26 flare (Figure 2). This event is of much longer duration than the event on 1980 June 7, about 20 min compared to about 1 min.

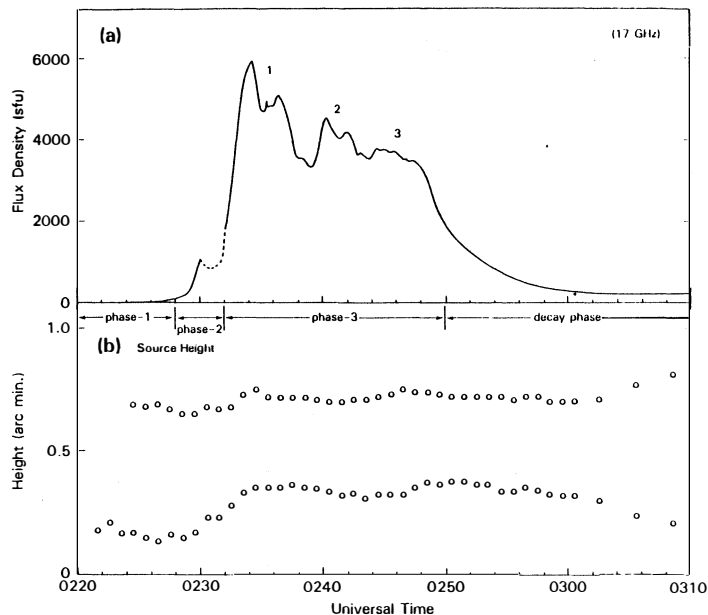


Figure 2: (a) The time profile of the 17 GHz microwave emission and (b) the time variation of the heights of two microwave (17 GHz) sources for the 1982 November 26 flare.

The microwave observations were made with the 17-GHz interferometer at Nobeyama, Japan, and the hard X-ray observation with the Hard X-Ray Burst Spectrometer (HXRBS) on SMM. More details will be reported in a separate paper ((Nakajima et al. 1984).

- (1) The microwave burst is composed of three successive peaks with a quasi-periodicity of about 6 min as indicated by number 1-3 in Figure 2(a).
- (2) Each of the microwave peaks further consists of two sub-peaks. The hard X-ray time profiles seems to coincide with the microwave sub-peaks. The SMM hard X-ray data are available only for the first peak.
- (3) The microwave and hard X-ray emissions start almost simultaneously within 10 seconds.
- (4) The microwave source is composed of two sources, one at a height of $\sim 10^4$ km above the photosphere and the other at $\sim 3 \times 10^4$ km. These values are derived on the assumption that the sources are located directly above the H α flare (S10°, W88°).

Figure 2(b) shows the height of the two microwave sources as a function of time. In the pre-burst phase (phase 1: 0220-0228 UT), the upper source appears at a height of $\sim 2.9 \times 10^4$ km above the photosphere and the lower one at $\sim 0.7 \times 10^4$ km. In phase 2, the lower source rises at a velocity of ~ 30 km s $^{-1}$. The main phase (phase 3) started when the lower source reaches a height of $\sim 1.5 \times 10^4$ km. It is suggested that the two sources collide with each other at this time. In fact, a small up-and-down motion of the lower source is observed in the main phase. The oscillation period and peak-to-peak amplitude of the up-and-down motion are ~ 14 min and $\sim 2 \times 10^3$ km (significantly larger than the fluctuation level due to the signal to noise ratio), respectively. After the main phase, the lower source begins to go down towards its previous position. On the other hand, the upper source rises gradually, though it remains at almost the same height until the decay phase starts.

The observational facts summarized above, especially the collision of the two microwave sources and the small up-and-down motion of the lower source in the 1982 November 26 event, suggest that the current-loop coalescence takes place. The existence of two H α bright components in the 1980 June 7 event also supports this interpretation.

III. INTERPRETATION BY SIMULATIONS

Two parallel current loops are unstable against the coalescence instability (Pritchett and Wu 1979). They are attracted by and collide with each other and finally coalesce into one loop. Its nonlinear development can release a large amount of poloidal magnetic energy associated with the current loops into particle energies (Tajima et al. 1982; Leboeuf et al. 1982). We investigated this process, i.e., the global plasma dynamics, heating and acceleration of particles, and so on, through computer simulations. Here, we made two different types of simulations in order to experiment with a wide variety of plasma parameters: one is an MHD particle simulation (Brunel et al. 1981), and the other a collisionless full-electromagnetic particle simulation (Tajima 1982), both of which are two-dimensional in space across the plane perpendicular to the current loops and three-dimensional in velocity space.

(a) Fast Coalescence---1980 June 7 Flare

The case that two parallel loops have sufficient electric currents so that they attract each

other fast enough (in about one Alfvén transit time) was simulated using the collisionless full-electromagnetic particle code.

The resultant time history of the electron temperature is shown in Figure 3(a).

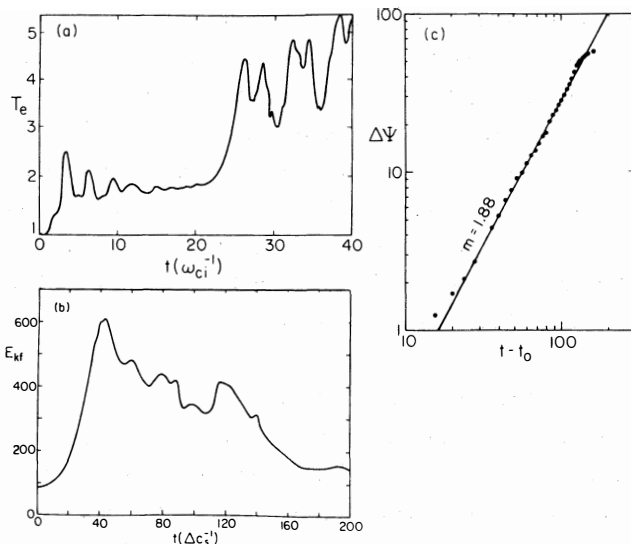


Figure 3: (a) The time history of the electron temperature T_e in case of fast coalescence (the oscillation period is about one Alfvén time) from the EM particle simulation. $\omega_{ci} = eB/Mc$ the ion cyclotron frequency and here one Alfvén time is about $8\omega_{ci}^{-1}$. T_e is normalized with the initial value.

(b), (c): Time histories of (b) the electron kinetic energy E_{kf} and (c) the integrated reconnected flux $\Delta\Psi$ through the X-points, in case of slower coalescence (the oscillation period is about five Alfvén times), from the MHD particle simulation. The time unit is Δc_s^{-1} with Δ and c_s being the grid spacing and the sound speed, respectively. The initial separation of loops is $\sim 60\Delta$. m is the slope ($\Delta\psi \propto (t-t_0)^m$).

We can clearly see a quasi-periodic oscillation, the period of which is about one Alfvén transit time ($8\omega_{ci}^{-1}$). The cause of this oscillation is as follows: after fast reconnection of poloidal magnetic fields takes place at the X-point between two approaching current loops, the two plasma blobs pass through each other and overshoot, resulting in the repetition of this process.

Figure 3(a) also shows that the electron temperature oscillation is characterized by prominent double sub-peak structure. The double sub-peaks occur just before and after each peak in the magnetic field intensity. Just before a peak, the magnetic acceleration of the plasma by $j \times B$ becomes strongest so that the magnetic flux behind the colliding plasma blobs as well as the plasma blobs themselves are strongly compressed. This plasma compression causes the first sub-peak of the electron temperature. Then, the plasma particles acquire velocities close to the Alfvén speed along the colliding direction, so that they detach from the magnetic flux against which they have been compressed, resulting in an expansion and hence in an adiabatic cooling of the plasma as the magnetic fields obtain peak values. After the peak in the magnetic fields, the process reverses giving rise to the second sub-peak of the electron temperature.

A similar time history is obtained for the kinetic energy of high-energy tail electrons and protons as well as for the proton temperature. The acceleration of the high energy-tail particles is due to a combination of localized electrostatic field acceleration across the poloidal magnetic field and magnetic acceleration in the poloidal to toroidal directions (Tajima et al. 1983). Since these processes accompany the local plasma compression/ decompression just before and after coalescence, it is not surprising that the time profile of the microwave emissions caused by high-energy tail electrons (Figure 1(a)) resembles that of figure 3(a).

The results of this simulation can also explain the observed period of the quasi-periodic oscillation of the 1980 June 7 event. The observed period (~ 8 seconds) of the June 7 flare is close to one Alfvén transit time (~ 4 sec) which is estimated with source size (~ 5 arc sec), magnetic field (~ 200 Gauss; Kiplinger et al. 1983) and emission measure ($\sim 10^{49}$ cm $^{-3}$) from the GOES soft X-ray data (Solar Geophysical Data).

(b) Slow Coalescence— 1982 November 26 Flare.

When two parallel loops have insufficient electric currents or are well separated and hence the attracting force of them is weaker than that of the previous case, reconnection of poloidal magnetic fields during loop coalescence becomes slower. (However, this reconnection rate is still faster than what would be predicted by a classical tearing theory (Furth et al. 1963)). This case was also simulated using the MHD particle code. Figure 3(b) shows the temporal development of plasma kinetic energy (the electron pressure energy) during the coalescence. Also shown in Figure 3(c) is the time history of the integrated reconnected magnetic flux through the X-point (case shown in Figure 5(a) in Bhattacharjee, et al. 1983). Note that a slight amount of oscillations of reconnected flux can be seen around the straight line. Again we can see the oscillatory behaviour with double sub-peak structure in both time histories, though it is less prominent compared with that of the fast coalescence case presented in the previous subsection. The period of oscillation is about 5 times the Alfvén transit time.

The obtained time history resulting from the simulation is explained as follows. In the case of slower reconnection, the two plasma blobs do not pass through each other but are pushed back by the magnetic field compressed between the two loops. This motion is repeated resulting in the damping oscillation shown in Figure 3(b). The amplitude of the oscillation in this case is less prominent compared with the previous case (Figure 3(a)).

The observed plasma kinetic energy oscillations exhibit a structure quite similar to the microwave time profile of the 1982 November 26 flare as shown in Figure 2(a). The source size of the November 26 flare is about 10 times larger than that of the June 7 flare. We therefore estimate the calculated period of the oscillation to be $5 \times 4 \times 10 = 200$ sec, assuming that the Alfvén velocity is about the same for both cases. This period is close to the observed period of about 6 min. Note also that in this case the flow velocity is much below the Alfvén velocity in agreement with the observational fact that the 30 km/s colliding velocity of the lower loop is much smaller than the Alfvén velocity of $\sim 10^3$ km/s.

IV. SUMMARY AND CONCLUSIONS

The results obtained from computer simulations of the coalescence instability of two current

loops are in good agreement with observations of two widely differing flares.

The key characteristics which are well explained are the simultaneous accelerations of both electrons and ions, and the double sub-peak structure in quasi-periodic pulses. The double sub-peak structure is more pronounced when the currents in the two loops are sufficient for the fast coalescence to occur. This case corresponds to the 1980 June 7 flare. When the currents are insufficient for the fast coalescence, the double sub-peak structure is less pronounced. This case corresponds to the 1982 November 26 flare. In addition, we have the observation suggesting the collision of the two microwave sources for the 1982 November 26 event.

Therefore, we consider that this mechanism is a plausible process for the particle acceleration mechanism in solar flares.

ACKNOWLEDGMENTS

We are grateful to T. Kosugi, K. Kai, B.R. Dennis, and A. Kiplinger for useful discussions. This work was supported by the National Science Foundation Grant ATM 82-14730. One of us (H.N.) was supported by the Laboratory for Astronomy and Solar Physics at NASA Goddard Space Flight Center and the National Academy of Sciences/National Research Council.

REFERENCES

- Bai, T. 1981, in *Gamma Ray Transients and Related Astrophysical Phenomena*, ed. R.E. Lingener, H.S. Hudson, and D.M. Worrall (New York: AIP), P. 409.
- Bai, T., Hudson, H.S., Pelling, R.M., Lin, R.P., Schwartz, R.A., and von Rosenvinge, T.T. 1983, *Ap. J.*, 267, 433.
- Bai, T. and Ramaty, R. 1979, *Ap. J.*, 227, 1072.
- Bhattacharjee, A., Brunel, F., Tajima, T. 1983, *Phys. Fluids*, 26, 3332.
- Brunel, F., Leboeuf, J.N., Tajima, T., Dawson, J.M., Makino, M., and Kamimura, T. 1981, *J. Comput. Phys.*, 43, 268.
- Chow, Y. 1983, private communication.
- de Jager, C. 1969, in *COSPAR Symposium on Solar Flares and Space Science Research*, ed. C. de Jager and Z. Svestka (Amsterdam: North Holland), p.1.
- Forrgst, D.J. et al. 1981, 17th Inter. Cosmic Ray Conf., 10, 5.
- Forrest, D.J. and Chupp, E.L. 1983, *Nature (Letters)*, 305, 291.
- Furth, H.P., Killeen, J., and Rosenbluth, N.N. 1963, *Phys. Fluids*, 6, 459.
- Kane, S.R., Kai, K., Kosugi, T., Enome, S., Landecker, P.B., and McKenzie, D.L. 1983, *Ap. J.*, 271, 376.
- Kiplinger, A.L., Dennis, B.R., Erostr, K.J., and Orwig, L.E. 1983, *Ap. J.*, 273, 783.
- Leboeuf, J.N., Tajima, T., and Dawson, J.M. 1982, *Phys. Fluids*, 25, 784.
- Nakajima, H., Kosugi, T., Kai, K., and Enome, S. 1983, *Nature (Letters)*, 305, 292.
- Nakajima, H., et al. 1985, in preparation.
- Pritchett, P. and Wu, C.C. 1979, *Phys. Fluids*, 22, 2140.
- Tajima, T. 1982, in *Fusion Energy-1981* (Trieste: International Center for Theoretical Physics) p. 403.
- Tajima, T., Brunel, F., and Sakai, J. 1982, *Ap. J.*, 258, L45.

Tajima, T., Brunel, F., Sakai, J., Vlahos, L., and Kundu, M.R. 1985, IAU
Symposium No. 107. P. 197.

Wild J.P., Smerd, S.F., and Weiss, A.A. 1963, *Ann. Rev. Astr. Ap.*, 1, 291.

This paper was presented on 1984 Plasma Astrophysics/Course and Workshop held at
Varenna, Italy. (Aug. 28–Sep. 7, 1984)

(Received October 31 1984)

A Dynamical Model of Solar Prominences with Current Sheet

J. Sakai¹ and H. Washimi²

1 Department of Applied Mathematics and Physics, Faculty of Engineering, Toyama University,
Toyama, 930 Japan

2 The Research Institute of Atmospheric, Nagoya University, Toyokawa, 442 Japan

Abstract

Recent observations of solar prominences show that slow upward motions ($\approx 1 \text{ km s}^{-1}$) occur through quiescent prominences and a fast input of material with horizontal motions ($\approx 5 \text{ km s}^{-1}$) occurs at both edges of prominences. A time-dependent dynamical model of solar prominences with current sheet is investigated. It is natural extension of the magnetostatic models proposed by Kippenhahn and Schlüter (KS) and Kuperus and Raadu (KR). It is shown that horizontal nonlinear oscillations can exist in the prominences. The global structure of current sheet including solar wind plasmas is also simulated by means of full MHD equations.

1. Introduction

Solar prominences are thin condensed sheets of cold material located in the low corona. They are suspended against gravity and above magnetic neutral lines between two opposite magnetic polarities (see Tandberg-Hanssen¹⁾, 1974). Recent observations (Malherbe et al.²⁾, 1983; Schmieder et al.³⁾, 1984) showed that slow upward motions (0.5 km s^{-1} in $H\alpha$ and 5.6 km s^{-1} in C_{IV}) occur in the prominences and a fast input of material with horizontal motion ($\approx 5 \text{ km s}^{-1}$) occurs at both edges of prominences.

Previous solar prominence models such as Kippenhahn and Schlüter⁴⁾ (KS) (1957) and Kuperus and Raadu (KR)⁵⁾ (1974) are magnetostatic and do not take into account the plasma dynamics, except for eruptive prominence model (see Sakai and Nishikawa⁶⁾, 1983). Recently, Malherbe and Priest (1983)⁷⁾ proposed a qualitative dynamical model with magnetic configurations either of the KR or KS type to explain the observed upward motions.

In the present paper we investigate a time-dependent dynamical model of solar prominences with current sheet. It is natural extension of the magnetostatic models proposed by the KS or KR. We pay particular attention on the local solutions describing the dynamical accumulation of plasmas near the current sheet. Coupled basic equations with self-similar solutions are derived. It is recently shown that magnetic reconnection forced by external plasma flow induced by coalescence of two current loops can be well described by the self-similar solutions (Sakai et al., 1984)⁸⁾.

It is shown that for nearly one-dimensional accumulation of plasmas horizontal nonlinear oscillations can exist in the prominences. Finally the global structure of current sheet including solar wind plasmas is simulated by means of full MHD equations.

2. Basic equations for current sheet model

We consider solar prominences as vertical thin current sheets supported by magnetic field in the low corona shown in Fig. 1. We consider a dynamical condensation of plasmas in the current sheet only by $\mathbf{j} \times \mathbf{B}$ force, neglecting the effect of thermal instability. We assume the law of adiabatic compression and that the sheet is homogenous in the z -direction. The MHD equation including gravity gives

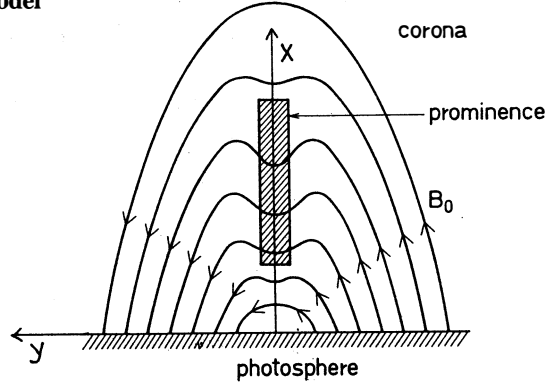


Fig. 1

$$\frac{\partial \rho}{\partial t} + \text{div}(\rho \mathbf{v}) = 0, \quad (1)$$

$$\rho \left(\frac{\rho \mathbf{v}}{\rho t} + \mathbf{v} \cdot \nabla \mathbf{v} \right) = -\nabla P + \frac{1}{4\pi} \text{rot} \mathbf{B} \times \mathbf{B} - \rho g \vec{e}_x, \quad (2)$$

$$\frac{\partial \mathbf{B}}{\partial t} = \text{rot}(\mathbf{v} \times \mathbf{B}) + \frac{c^2}{4\pi\sigma} \Delta \mathbf{B}, \quad (3)$$

$$\frac{\partial P}{\partial t} + \mathbf{v} \cdot \nabla P + \gamma P \text{div} \mathbf{v} = 0, \quad (4)$$

where the gravity is given by $g(x) = GM_\odot R_\odot^{-2} (1 + x/R_\odot)^{-2} = g_\odot (1 + x/R_\odot)^{-2}$ and $g_\odot = GM_\odot R_\odot^{-2}$.

We assume that the input horizontal flows around the current sheet obey

$$v_y = \frac{\dot{a}}{a} y, \quad (5)$$

where the dot means the time derivative and $a(t)$ is a scale factor characterizing continuous change of thickness of current sheet. The upward flow is taken as

$$v_x = v_{x0}(t) + \frac{\dot{b}}{b} x, \quad (6)$$

where v_{x0} and a scale factor $b(t)$ are determined self-consistently. The magnetic fields are assumed that

$$B_x = B_{x0}(t) y/\lambda, \quad B_y = B_{n0}(t) + B_{y0}(t) x/\lambda, \quad B_z = B_{z0}(t). \quad (7)$$

From the continuity equation (1) we find

$$\dot{\rho}/\rho + \dot{a}/a + \dot{b}/b = 0, \quad (8)$$

where ρ is a function of time only. The equation (8) gives

$$\rho = \rho_0 / ab, \quad (9)$$

where ρ_0 is a constant. From the induction equation (3) we obtain

$$B_{x0}(t) = B_0 / a^2, \quad (10)$$

$$B_{y0}(t) = B_0 / b^2, \quad (11)$$

$$B_{z0}(t) = B_{00} / ab, \quad (12)$$

$$\frac{\partial B_{n0}}{\partial t} = - \left(\frac{v_{x0}}{\lambda} \frac{B_0}{b^2} + B_{n0} \frac{\dot{b}}{b} \right), \quad (13)$$

where B_0 and B_{00} are constants.

If we assume that the pressure P is given by

$$P(x, y, t) = P_{00}(t) - P_0(t) \frac{x}{\lambda} - P_{x0}(t) \frac{x^2}{\lambda^2} - P_{y0}(t) \frac{y^2}{\lambda^2}, \quad (14)$$

we find from the equation (4)

$$P_{x0}(t) = P_0 / a^\gamma b^{\gamma+2}, \quad (15)$$

$$P_{y0}(t) = P_0 / a^{\gamma+2} b^\gamma, \quad (16)$$

$$\frac{\partial P_{00}}{\partial t} + \gamma P_{00} (\dot{a}/a + \dot{b}/b) - v_{x0} \frac{P_0(t)}{\lambda} = 0, \quad (17)$$

$$\frac{1}{P_0(t)} \frac{\partial P_0}{\partial t} + 2v_{x0} P_0 / P_0(t) \lambda a^\gamma b^{\gamma+2} + \dot{b}/b + \gamma \left(\dot{b}/b + \dot{a}/a \right) = 0, \quad (18)$$

where P_0 is a constant.

Finally we obtain basic equations for scale factors $a(t)$ and $b(t)$ from the equation of motions (2)

$$\dot{a} = \frac{c_s^2}{\lambda^2 a^\gamma b^{\gamma-1}} + \frac{V_A^2}{\lambda^2} \left(\frac{1}{b} - \frac{b}{a^2} \right), \quad (19)$$

$$\dot{b} = \frac{c_s^2}{\lambda^2 a^{\gamma-1} b^\gamma} - \frac{V_A^2}{\lambda^2} \left(\frac{a}{b^2} - \frac{1}{a} \right) + 2 \frac{g_\odot}{R_\odot} b, \quad (20)$$

$$\frac{\partial v_{x0}}{\partial t} + v_{x0} \frac{\dot{b}}{b} = \frac{P_0(t)}{\rho_0} \frac{ab}{\lambda} - \frac{B_{n0}(t) B_0}{4\pi\rho_0\lambda} \frac{(a^2 - b^2)}{ab} - g_\odot, \quad (21)$$

where we assumed that the gravitational acceleration $g(x)$ is approximated by $g(x) = g_\odot(1 - 2x/R_\odot)$, when $x \ll R_\odot$. $c_s^2 = 2P_0/\rho_0$ and $V_A^2 = B_0^2/4\pi\rho_0$.

If we neglect the pressure terms and the effect of gravity in the above equations we obtain

$$\dot{a} = \frac{V_A^2}{\lambda^2} \left(\frac{1}{b} - \frac{b}{a^2} \right), \quad (22)$$

$$\dot{b} = - \frac{V_A^2}{\lambda^2} \left(\frac{a}{b^2} - \frac{1}{a} \right), \quad (23)$$

which were first derived by Imshennik and Syrovatskii (1967)⁹⁾ for the investigation of plasma dynamics near X-type neutral point.

3. Self-similar solutions

We examine a few limiting cases for applications of solar prominence dynamics.

(case 1) $B_y=0$ and $g=0$.

In this case it is consistent to assume $V_{x0}=0$ and $P_0=0$. The above basic equations are simplified to

$$\ddot{a} = \frac{c_s^2}{\lambda^2 a^\gamma b^{\gamma-1}} - \frac{V_A^2 b}{\lambda^2 a^2} \quad , \quad (24)$$

$$\dot{b} = \frac{c_s^2}{\lambda^2 a^{\gamma-1} b^\gamma} \quad . \quad (25)$$

(case 2) $B_y = \text{constant}$ and $g = \text{constant}$.

In this case we can neglect the inhomogenous terms in v_x and B_y in Eq.(6) and (7). We find for $a(t)$

$$\ddot{a} = \frac{c_s^2}{\lambda^2 a^\gamma} - \frac{V_A^2}{\lambda^2 a^2} \quad . \quad (26)$$

and $v_{x0}(t)$ is determined from

$$\frac{\partial v_{x0}}{\partial t} = \frac{V_A^2 B_n}{\lambda B_0 a(t)} - g_\odot \quad , \quad (27)$$

instead of Eq.(21).

When the ratio of adiabatic capacity γ is larger than 2 ($\gamma > 2$), the equation (26) has the solutions of nonlinear oscillation. The period T of the nonlinear oscillation when $\gamma = 3$ is given by

$$T = 2\pi V_A^2 / E^{3/2} \lambda^2 \quad , \quad (28)$$

where E is a constant which is related with the initial conditions.

The minimum period T_{\min} is given by

$$T_{\min} = 2\pi \beta^{3/2} \tau_A \quad , \quad (29)$$

where $\beta = 8\pi P_0 / B_0^2 = c_s^2 / V_A^2$, and $\tau_A = \lambda / V_A$.

when $\gamma = 2$ and $v_A > c_s$, there occur only compressional motions. When E is small, we find

$$a(t) = \left(\frac{9}{2}\right)^{1/3} (v_A^2 - c_s^2)^{1/3} \lambda^{-2/3} (t_0 - t)^{2/3} \quad . \quad (30)$$

By means of Eq.(30) we obtain the upward flow v_{x0} from eq.(27)

$$v_{x0} = 3 \left(\frac{2}{9}\right)^{1/3} \frac{V_A^2}{\lambda^{1/3}} \frac{B_n}{B_0} \frac{(t_0 - t)^{1/3}}{(V_A^2 - c_s^2)^{1/3}} - g_\odot (t_0 - t) \quad . \quad (31)$$

If we take t_0 as the value when $v_{x0} = 0$, we find

$$t_0 \approx 0.84 (V_A / c_s)^3 \tau_A \quad . \quad (32)$$

The first term of Eq. (31) is always larger than the second term, so that we have upward flows. The time t_0 is the life time of the solar prominence which is order of 3.4 days if we take $V_A/c_2 \approx 33.3$ and $d \lambda/V_A \approx 10$ seconds.

4. Simulation of global structure with solar wind plasmas

We show the results of computer simulation by means of full MHD equations, which includes the expanding supersonic solar wind plasmas. The dipole magnetic field is taken at $x = 0.9 R_\odot$. On the solar surface the flows are taken along the magnetic field. The other boundary conditions are free. Fig. 2 shows the global plasma flow and magnetic field-line pattern. Fig. 3 shows the inflow velocity profile across y axis. Fig. 4 is the density profile and Fig. 5 is the magnetic field B_x . As seen in Fig. 3 and 5 the inflow velocity and magnetic field produced by the sheet current are well described as self-similar solutions which space dependency is proportional to y . The more detail comparison between the theory and the results of simulations will be needed.

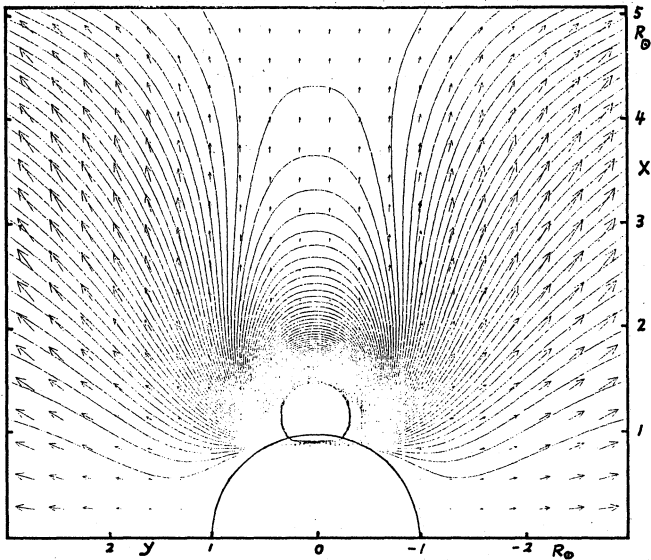


Fig. 2

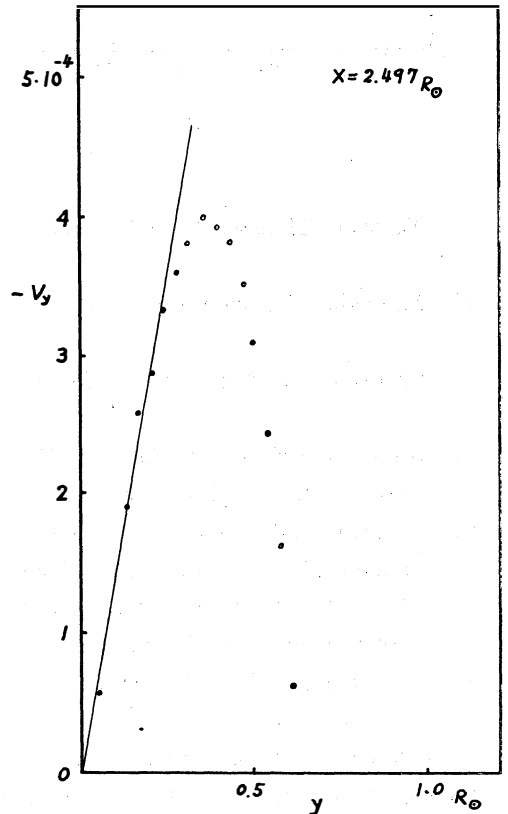


Fig. 3

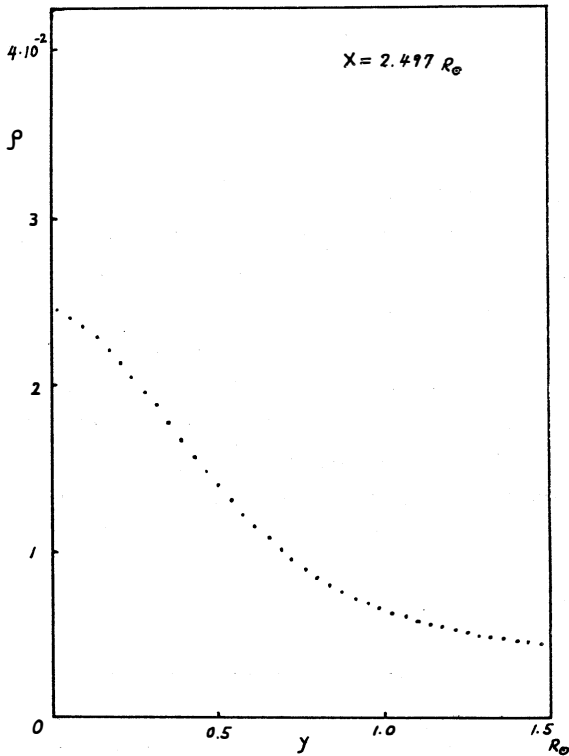


Fig. 4

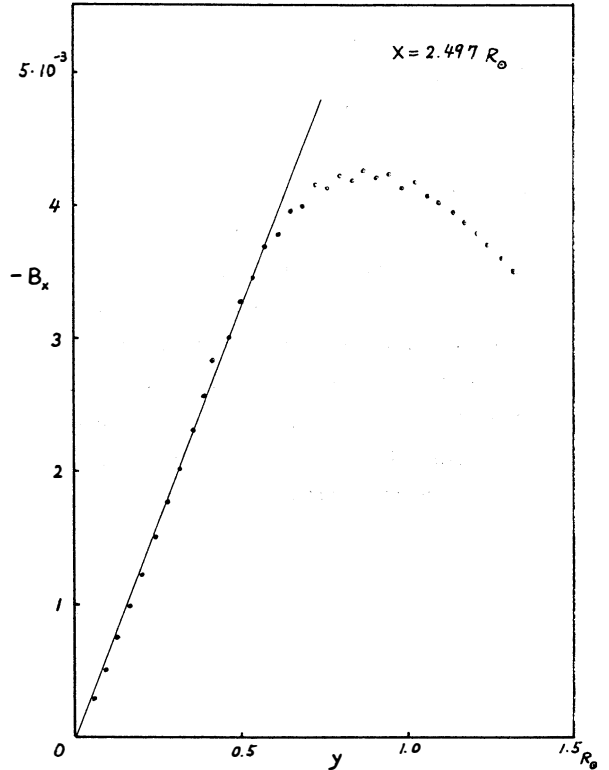


Fig. 5

References

- (1) Tandberg-Hanssen, E. 1974, Solar Prominence, D. Reidel Publ. Co., Dordrecht, Holland.
- (2) Malherbe, M., Schmieder, B., Ribes, E., and Mein, P. 1983, Astron. Astrophys. 119, 197.
- (3) Schmieder, B., Malherbe, M., Mein, P. and Tandberg-Hanssen, E. 1984, Astron. Astrophys. 136, 81.
- (4) Kippenhahn, R. and Schlüter, A. 1957, Z. Astrophys. 43, 36.
- (5) Kuperus, M., and Raadu, M. A. 1974, Astron. Astrophys. 31, 189.
- (6) Sakai, J. and Nishikawa, K. 1983, Solar Phys. 88, 241.
- (7) Malherbe, M., and Priest, E. 1983, Astron. Astrophys. 123, 80.
- (8) Sakai, J., Tajima, T., and Sugihara, R. 1984, Proc. Plasma Astrophysics/course and workshop, varenna, Italy, ESA SP-207, 189.
- (9) Imshennik, V. S., and Syrovatskii, S. I. 1967. Soviet Phys. JETP, 25, 656.

This paper was presented on Joint U.S.-Japan Seminar "Recent Advances in the Understanding of Structure and Dynamics of the Heliosphere during the Current Maximum and Declining Phase of Solar Activity" held at Kyoto, Japan. (5-9, November, 1984)

(Received October 31 1984)

Computer Modeling of Fast Collisionless Reconnection

J. N. LEBOEUF, F. BRUNEL, AND T. TAJIMA
INSTITUTE FOR FUSION STUDIES
UNIVERSITY OF TEXAS
AUSTIN, TEXAS 78712

J. SAKAI
DEPARTMENT OF APPLIED MATHEMATICS
AND PHYSICS, FACULTY OF ENGINEERING
TOYAMA UNIVERSITY
TOYAMA 930, JAPAN

C. C. WU, AND J. M. DAWSON
DEPARTMENT OF PHYSICS
UNIVERSITY OF CALIFORNIA
LOS ANGELES, CALIFORNIA 90024

ABSTRACT

Particle simulations of collisionless tearing, reconnection and coalescence of magnetic fields for a sheet-pinch configuration show that reconnection is Sweet-Parker like in the tearing and island formation phase. It is much faster to explosive in the island coalescence stage. Island coalescence is the most energetic process and leads to large ion temperature increase and oscillations in the merged state. Similar phenomena have been observed in equivalent MHD simulations. Coalescence and its effects, as observed in our simulations, may explain many of the features of solar flares and coronal X-ray brightening.

1. INTRODUCTION

Computer modeling of magnetic field reconnection, including island coalescence, has been tackled mainly with collisional MHD codes. Few kinetic studies of reconnection have been reported so far (Dickman and Morse, 1969; Amano and Tsuda, 1977; Katanuma and Kamimura, 1980; Terasawa, 1981; Hamilton and Eastwood, 1982; Leboeuf, Tajima and Dawson, 1981 and 1982; Tajima, 1982) even though in space plasmas collisionless tearing modes are believed to be one of the most effective mechanisms for magnetic field line reconnection. This is particularly true for the Earth's magnetospheric tail where the particles' mean free path is very large. Dickman, Morse and Nielson (1969) used a magnetostatic code to study tearing modes in the Astron fusion device. They found that the Astron plasma layer first develops tearing modes, but at later times the wavelength of this mode increases by coalescence until the plasma is completely reassembled. Amano and Tsuda (1977) were the first to study forced reconnection

with an electromagnetic code. They forced a flow towards the initial magnetic neutral sheet and observed the formation of an x-point. They also remarked that Joule heating in the diffusion region was not sufficient for the explosive energy release such as that observed in astrophysical and geophysical phenomena. The study of Katanuma and Kamimura (1980) involves using a magnetostatic code to study the nonlinear evolution of collisionless tearing modes. They verified the Drake-Lee (1977) theory of tearing. They did observe island coalescence in the case of multi-mode tearing. However, no discussion of the energetics of the interaction was given. Again using a magnetostatic code, Hamilton and Eastwood (1982) realistically modeled the geomagnetic tail and confirmed the stabilizing influence of a small magnetic field normal to the sheet of the tearing mode. Finally, Terasawa (1981) used a reduced Darwin model, with electrostatics neglected, and followed the ions only. He verified the explosive tearing mode theory of Galeev, Coroniti and Ashour-Abdalla (1978). The question is whether adding the electrons and the electrostatics will modify his conclusions.

Our program of kinetic simulations of collisionless reconnection was primarily motivated by the laboratory experiments of W. Gekelman and R. L. Stenzel. (Stenzel and Gekelman, 1979; Gekelman and Stenzel, 1981) The tools used consist of magnetostatic and electromagnetic finite size particle simulation models with two spatial dimensions only. This paper will mainly be a review of our own work, and some comparisons with similar MHD simulations. Applications to the physics of solar flares will also be discussed.

By having a current flow in two strips perpendicular to the plane of the simulation, with the current ramped in time much as it is in the experiments of Gekelman and Stenzel, we are able to pass through the successive stages of current sheet formation in between the two strips, tearing of the current sheet to form magnetic islands and finally magnetic island coalescence. The onset of coalescence occurs in an explosive fashion. Recent MHD simulations of reconnection and coalescence (Brunel, Tajima, and Dawson, 1982) exhibit comparable behaviour. Addition of a magnetic field parallel to the strips (a toroidal field in tokamaks) introduces incompressibility and prevents the fast reconnection that otherwise occurs (Tajima, 1982). The tearing phase leads to almost no energization of the particles' kinetic energy. Magnetic island coalescence, on the other hand, leads to a large increase in ion temperature. The oscillations exhibited by the ion temperature in the merged phase have also been observed in an MHD simulation of island coalescence (Wu, Leboeuf, Tajima, Dawson, 1980). These oscillations resemble what is reported of the solar gamma ray amplitude oscillations (Forrest et al., 1982) associated with loop coalescence in solar flares (Tajima, Brunel, Sakai, 1982).

II. COMPUTER MODEL

Our collisionless particle simulations follow the evolution of a plasma configuration which is unstable against the tearing and subsequent coalescence instabilities. The electromagnetic code (Leboeuf, Tajima, Dawson, 1982) is two-and-one-half (two space, x and y , and three velocity and field, x , y , and z dimensions) dimensional and periodic in both the particles and field quantities. The model includes electrons and ions, with ion-to-electron mass and temperature ratios of $M_i/m_e = 10$ and $T_i/T_e = 1/2$ respectively in a benchmark case. Both species of particles are given Maxwellian velocity distributions in all three directions at time $t = 0$. Four

particles per unit cell are typically used. The particles are loaded uniformly in space so that the density is uniform at $t=0$. We focus on rectangular system sizes $L_x \times L_y = 128 \Delta \times 32 \Delta$ and $256 \Delta \times 16 \Delta$, where Δ is the unit grid spacing. For the first, $\Delta = \lambda_e$, the electronic Debye length and the speed of light $c = v_{te}$, the electron thermal velocity, so that the collisionless skin depth $\delta = c/\omega_{pe} = 5\lambda_e$. For the second, $\Delta = 2\lambda_e$, with collisionless skin depth $c/\omega_{pe} = 6\lambda_e$ and the ratio of thermal velocity to speed of light $v_{te}/c = 1/6$.

The magnetic configuration is established by external current strips placed at $y=0$ and $y=L_y$ which extend along x . The current flows in the z -direction. To avoid infinite magnetic energy, the return path of the current is chosen to be through the plasma. At $t=0$, the current is zero in the strips and rises sinusoidally from zero at $t=0$ to a maximum at the quarter period after which it is kept constant (crowbar phase), with a rise time greater than or equal to the magnetosonic transit time from center to plates. By varying the strength of the currents in the strips, different plasmas are obtained. For the 128×32 case, the plasma $\beta = 0.2$, for maximum magnetic field and average density. This entails electron and ion Larmor radii of $1.3\lambda_e$ and $2.6\lambda_e$ respectively, and an Alfvén velocity $v_A = 1.22 v_{te}$. For the 256×16 case, the maximum field is such that $\beta = 0.06$, $\rho_e = .85\lambda_e$, $\rho_i = 1.90\lambda_e$. The Alfvén speed is $v_A = 2.2 v_{te}$. When a constant toroidal field is imposed in the z -direction it is such that $0.2 \lesssim B_t/B_p \lesssim 4$ where B_p is the maximum poloidal field. Straight forward calculations of the magnetic Reynolds number from the finite size particles collision frequency yield $S=800$. However since the current flow is in the ignorable z direction, the actual collisionality may be regarded as much smaller than the in-plane value and S greater than the above value.

It should be noted that our model is limited by the periodic boundary conditions imposed on both the particles and fields. Moreover, the system sizes used only describe a few collisionless skin depths, ion Larmor radii and Debye lengths. We are actually looking at rather microscopic x -points and o -points.

III. MAGNETIC RECONNECTION

We discuss the compressible cases without toroidal field first and those with toroidal field next. The "collisionless" reconnection rate in both cases is measured and compared with theory and similar MHD simulations.

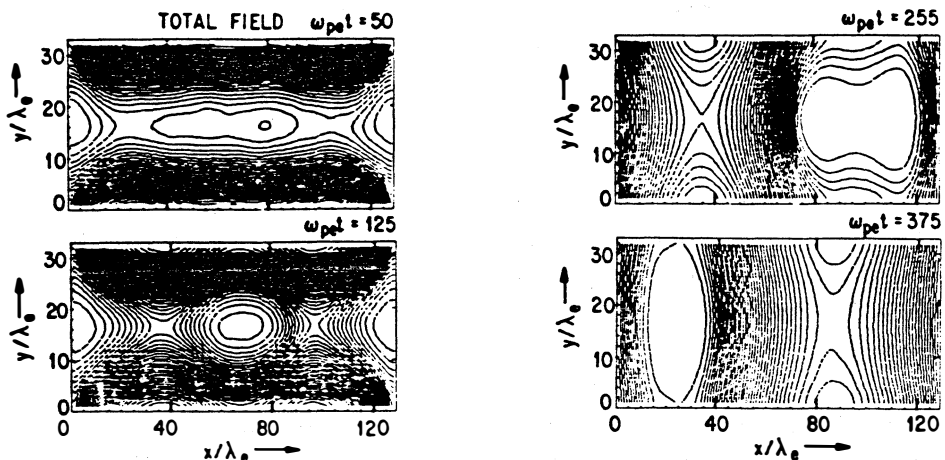


Fig. 1 Time evolution of the magnetic field lines in the 128×32 case with $B_t/B_p = 0$. (Leboeuf, Tajima, Dawson, 1982)

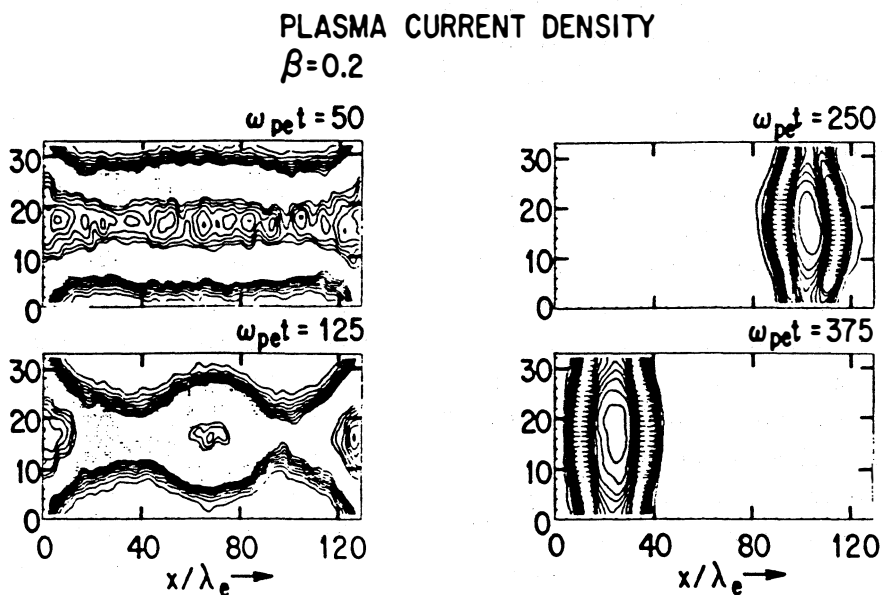


Fig. 2 Time evolution of the current density in the 128×32 case with $B_t/B_p = 0$. The dotted contours indicate regions of maximum plasma current. (Leboeuf, Tajima, Dawson, 1982)

The evolution of the field lines in the 128×32 case ($B_t = 0$) is shown in Fig. 1. The corresponding plasma current density is displayed in Fig. 2. The various stages of evolution consist of a current sheet formation at the center of the system, break-up of the current sheet to form a chain of x-points and o-points, i. e. establish a sheet pinch configuration, swelling of the islands by reconnection and finally coalescence of the islands. All of these phenomena happen within 2 to 4 Alfvén times. As the current increases in the strips, an equivalent amount of current is returned through the plasma. (Note the external current is maintained throughout the simulations.) Pinching occurs and induces a flow ($V_y = \pm J_p^z \times B_x^e$) through the x-points and into the o-points where the plasma remains trapped. The attractive force between the so-formed plasma filaments induces coalescence. The external circuit is coupled to the plasma and is the source of free energy. The events described are forced on the plasma by the external circuit and in that sense we are looking at forced reconnection.

In the 256×16 case ($B_t = 0$), the change in magnetic topology is best illustrated by the plasma current density. Tearing of the long and narrow current sheet induces 16 islets. They eventually coalesce pairwise down to one island, as shown in Fig. 3.

Tajima (1982) found that when a constant toroidal field B_z of strength B_t is added to the above configuration things happen in a qualitatively similar fashion for $B_t \lesssim B_p$, the maximum poloidal field, as when $B_t = 0$ in terms of topological changes. In particular the violent coalescence instability is still seen. When $B_t \gtrsim B_p$, however, the current sheet still tears into many islets but the coalescence instability does not occur (within the simulated time scales).

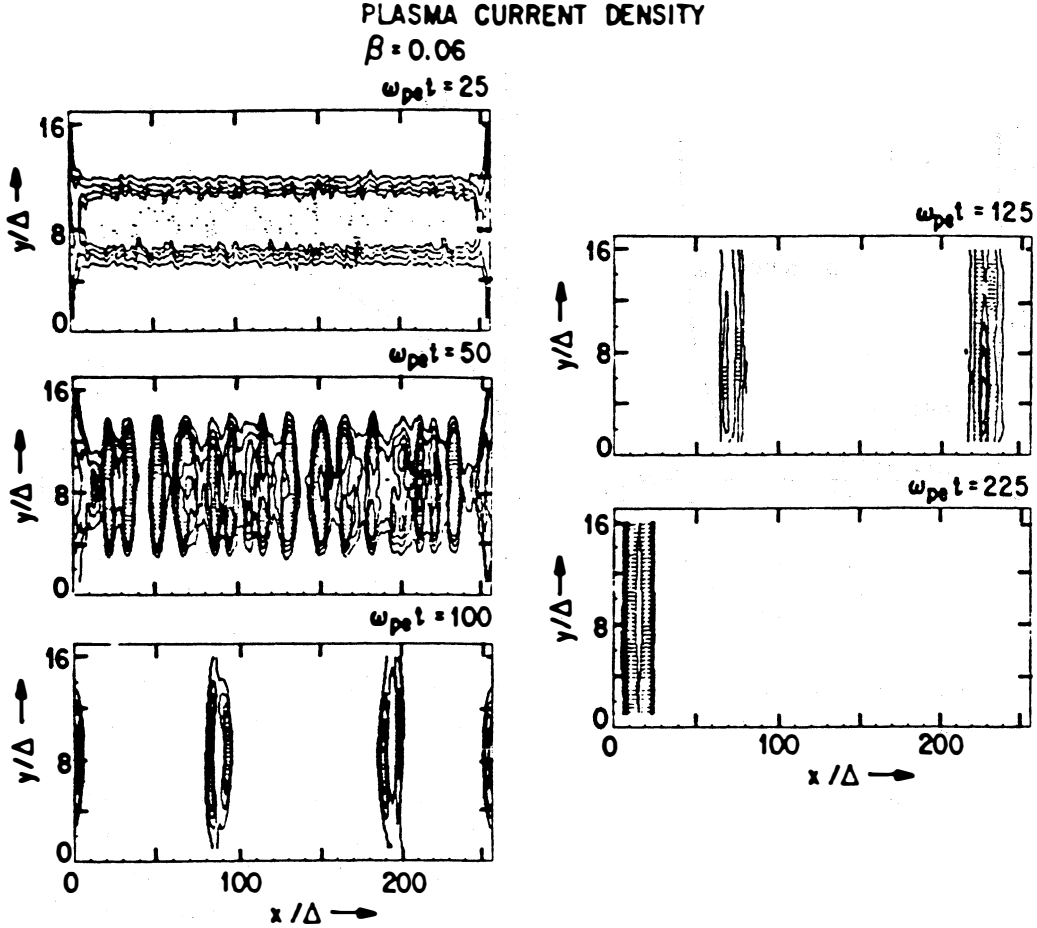


Fig. 3 Time evolution of the current density in the 256×16 case with $B_t/B_p = 0$. (Leboeuf, Tajima, Dawson, 1982)

For $B_t \gtrsim B_p$ i. e. strong field perpendicular to the plane of the simulations, the plasma is strongly magnetized ($\rho_e \lesssim \Delta$, $\rho_i \lesssim 3\Delta$) and cross-field motion of the particles is strongly impaired except through $E \times B$ spatial diffusion, i. e. the plasma is nearly incompressible since $\nabla \cdot v = \nabla \cdot (E \times B) = 0$. In this case many islets lead to turbulence of tearing modes. Each mode has a lifetime roughly the inverse of the linear growth rate. A renormalized turbulence theory was constructed by Tajima (1982) based on this observation. The flux increases with a time exponent smaller than predicted by Rutherford (1973) or Drake and Lee (1977) and may be explained by this turbulent tearing mode theory. In the collisionless tearing turbulence the magnetic fluttering-induced electron response adds the essentially new physics.

Measurements of the poloidal flux trapped in one island or islet (private flux) as a function of time for $B_t/B_p = 0.2$ (128×32 case) and $B_t/B_p = 2$ (256×16 case) are shown in Figs. 4a and 4b respectively. In the weak toroidal field case, a linear phase, which encompasses the

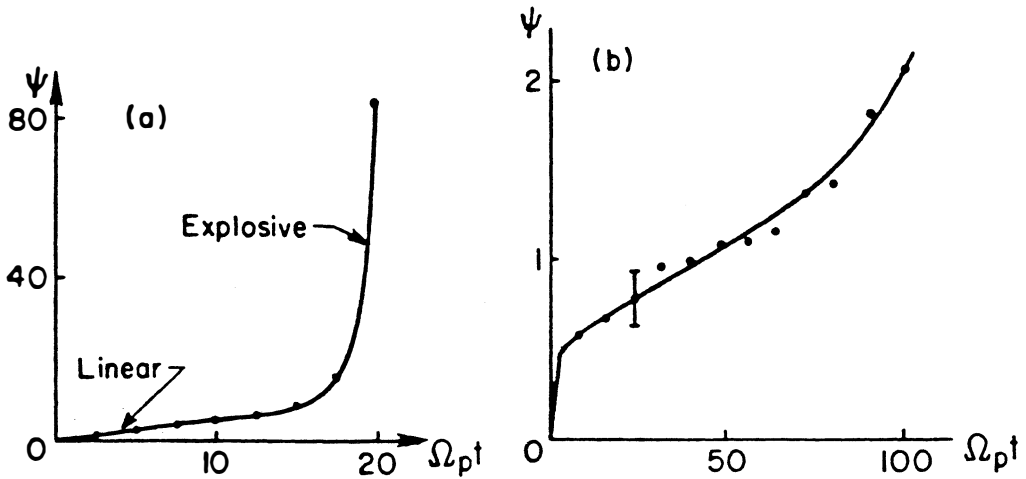


Fig. 4 Time evolution of the private poloidal flux in a) the 128×32 case with $B_t/B_p = 0.2$ and b) in the 256×16 case with $B_t/B_p = 2$. Ω_p represents the electron gyrofrequency measured with respect to the maximum poloidal field. (Tajima, 1982)

island swelling stage, precedes the explosive coalescence one. For the strong toroidal field case, the rise is linear in time over ten times longer time scales and the flux increase is 10^{-2} times smaller.

MHD simulations of magnetic reconnection driven either by external currents pinching the plasma by Brunel, Tajima and Dawson (1982) or by the coalescence instability of an equilibrium chain of magnetic islands by Bhattacharjee, Brunel and Tajima (1983) show similar behavior. It is found that fast magnetic reconnection may consist of more than one stage. After the Sweet-Parker phase (Parker, 1979) is established for an Alfvén time, a faster second phase of reconnection takes over if the plasma is compressible. The Sweet-Parker flux is

$$\psi_{sp}(t) = \eta^{1/2} B_p(y=a) \left(\frac{n_i}{n_e} \right)^{1/2} \left(\frac{v_A}{L} \right)^{1/2} t, \quad (1)$$

where n_e and n_i are the densities outside and inside the current channel, a the current channel width, η the resistivity, L the length of the reconnecting region, B_p , the poloidal field and v_A the Alfvén velocity. Our basic equations to describe the system have been reduced in order to gain reasonable analytical expressions and straightforward understanding of the underlying physics:

(outside)

$$\frac{\partial \psi}{\partial t} = v_1 \times B_p, \quad (2)$$

$$p_e^2 + B_e^2 / 8\pi = p_i^2 + B_i^2 / 8\pi \sim p_i, \quad (3)$$

(inside)

$$\frac{\partial \psi}{\partial t} = \eta \nabla_{\perp}^2 \psi \approx \eta B_p / a, \quad (4)$$

$$n_e L v_{\perp} = n_i a u. \quad (5)$$

The left-hand side of Eq. (5) is the particle flux outside the separatrix, while the right-hand side is that within the separatrix. The first equations (Eq. (2) and Eq. (4)) are the magnetic flux equations, i.e. Faraday's law, while the second equations (Eq. (3) and Eq. (5)) are related to the equations of motion of the plasma. As is expected, the outside solution should be the MHD solution according to Eq. (2). The velocity u in the internal layer was determined to be

$$u \sim v_{Ai} = B_e / (4\pi M n_i)^{1/2} \quad (6)$$

by Brunel and Tajima (1983). Using Eqs. (2)–(6) the second phase flux is calculated to go as

$$\psi = \psi_{sp}(t_A) (t/t_A)^{n_i/n_e} \quad (7)$$

Scalings of $\psi \propto t^4$ have been obtained in the pinching cases. Coalescence driven reconnection yields scalings up to $\psi \propto t^2$ for the compressible cases, but $\psi \propto t$ when a large toroidal field is applied.

IV. ENERGETICS

We concentrate here on cases with $0 \lesssim B_t/B_p \lesssim 0.2$ or compressible situations. A summary of the behavior of the various components of the temperatures for the 128×32 case with $B_t = 0$ is given in Fig. 5.

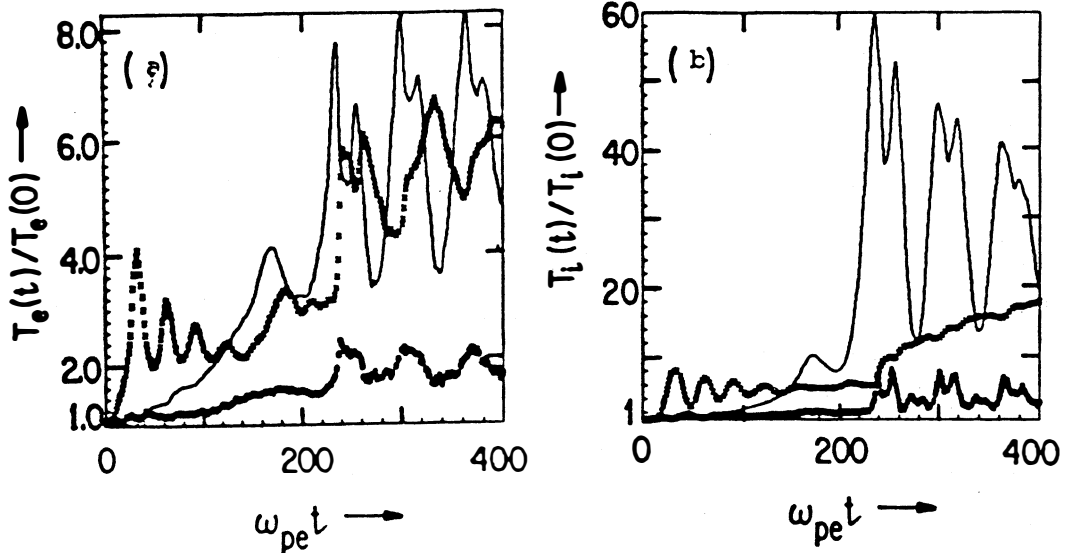


Fig. 5 Time evolution of the temperatures in all three directions in the 128×32 case with $B_t/B_p = 0$. for a) electrons and b) ions. The full curve refers to the x-direction, the crosses and circles to the y and z ones respectively. (Leboeuf, Tajima, Dawson, 1982)

No sizable increase is detected in the current sheet formation and tearing phases, just the adiabatic compression component associated with the external current rise in the strips. As the islands coalesce, fast increase in the temperatures is apparent. Most of the increase is concentrated in the x-direction, where the ion temperature in the merged phase is on average 30 times

its initial level. The ions achieve a higher temperature than the electrons in all three directions. Note the large oscillations in the ion and electron temperatures with a period $\tau = 60/\omega_{pe}$ in the merged phase. The momentum distribution functions of electrons and ions in the x-direction displayed in Fig. 6 exhibit bulk heating and symmetric high energy tails at late times. As shown in Fig. 7, an even more pronounced increase in temperature is obtained from the successive coalescence events of the 256×16 case with $B_t = 0$.

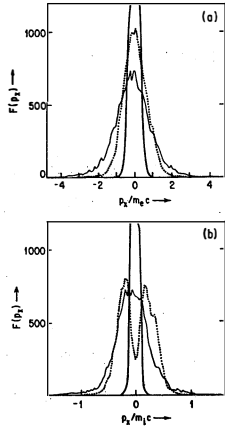


Fig. 6

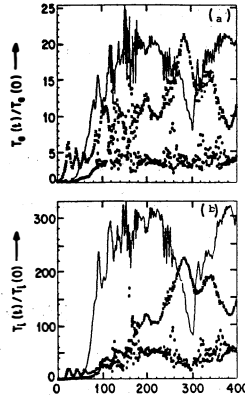


Fig. 7

Fig. 6 Momentum distribution functions in the x-direction for the 128×12 case with $B_t/B_p = 0$, and for a) electrons and b) ions at $\omega_{pe} t = 50$ (full bold curve: island formation stage), $\omega_{pe} t = 225$ (dotted curve: coalescence phase), $\omega_{pe} t = 325$ (full thin curve: merged state). The momenta are normalized to $m_e c$ for the electrons and $M_i c$ for the ions. (Leboeuf, Tajima, Dawson, 1982)

Fig. 7 Time evolution of the temperatures in all three directions in the 256×16 case with $B_t/B_p = 0$, for a) electrons and b) ions. The full curve refers to the x-direction, the crosses and circles to the y and z ones respectively. (Leboeuf, Tajima, Dawson, 1982)

Results for the compressible 128×32 case with $B_t/B_p = 0.2$ are displayed in Fig. 8. Fig. 8a is a plot of ion temperature versus time. Again sharp increase upon coalescence followed by oscillations is apparent. Fig. 8b, which represents the ion distribution function in the x-direction after coalescence, shows bulk heating and symmetric tails. Fig. 8c is a plot of the ion distribution function along the toroidal field. It shows three regimes. First the bulk, then the exponential section $f_2(p_z) = \exp(-P_z/P_0)$

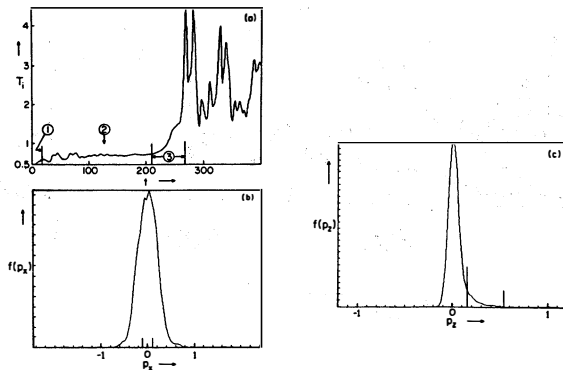


Fig. 8 Various data from 128×32 case with $B_t/B_p = 0.2$. a) Time evolution of the ions temperature. Phases 1 and 2 are the tearing growth and saturation phases, phase 3 is the explosive coalescence phase. The period of temperature oscillations in the merged phase is $\tau \sim \tau_A$. b) ion distribution function in the x-direction and in the merged state. c) Ion distribution function in the z-direction and in the merged state. The thermal momenta are indicated by tickmarks near $p = 0$. Momenta are normalized with respect to $M_i c$. (Tajima, Brunel, Sakai, 1982)

and third the flat distribution extending up to the relativistic factor $\gamma \sim 2$ in the relativistic region, where $p_0^2/2M_i = 10 \times$ (bulk temperature). The bulk ion heating in the is attributed to the "adiabatic heating"; the exponential heating in the x and z directions are inductive in nature. The hot flat long tails in the x and z directions are due to acceleration by the magnetosonic shock [Tajima et al., 1983]. The maximum energy may be estimated based on the Alfvén Mach number. Most of the energy of the particles still belongs to the bulk component, however.

We have seen that the total flux reconnection of two islands takes place within 1 to 2 Alfvén times. The magnetic energy contained in the islands is explosively released into kinetic energy as seen in Figs. 6, 7 and 8. The amount of available potential energy W_c by attracting two toroidal current rods I of radius a with separation L is

$$W_c \simeq -2I^2/c^2 \ell n(L/a) \quad . \quad (8)$$

Our simulations show that about 1/6 of the energy W_c was transferred to kinetic energy upon coalescence in the 128×32 case with $B_t = 0$. This amount of energy conversion is about two magnitude above that during the tearing process. The oscillations in temperature observed in the 128×32 cases are found to be magnetosonic ones with a frequency $\omega = kv_A$, where $k = 2\pi/a$, a the current channel width and v_A calculated according to the magnetic field measured at the island. These temperature oscillations can be attributed to the overshooting of the two coalescing and colliding current filaments. Once the two filaments merge, they are bound by the common flux and the resulting island shape oscillates from prolate to oblate on the time scale of the temperature oscillations. The colliding plasmas cause turbulent flows within the final island and the originally directed energy is eventually dissipated into heat. The turbulent mixing in the island also cause the bulk heating observed on the distribution functions.

Similar features have also been observed in 2-D Eulerian MHD simulations of the coalescence instability of magnetic islands formed by nonlinear tearing modes (Wu, Leboeuf, Tajima and Dawson, 1980). A sheet-pinch configuration is modeled. Initially small perturbations consisting of two linearized eigenfunctions are imposed: one with a wavelength $\lambda = L/2$ and a smaller perturbation with $\lambda = L$, L being the system size. The perturbation with $L/2$ gives rise to the formation of two magnetic islands at the stage of the nonlinear tearing mode. These islands then interact with each other due to the presence of the smaller perturbation with wavelength $\lambda = L$; they coalesce and merge into larger units. The time evolution of the fluid kinetic energy for an MHD case with $S = 2000$ is displayed in Fig. 9b, alongside a temperature plot for the 128×32 case with $B_t = 0$. The initial increase in energy up to $t = 120 \tau_A$ corresponds to the exponential growth of the $L/2$ perturbation with linear growth rate $\gamma_{L/2} = 9.6 \times 10^{-3}$. By $t = 720 \tau_A$, the perturbation with wavelength $\lambda = L$ ($\gamma_L = 1.2 \times 10^{-2}$) has reached a large enough amplitude to trigger coalescence. During coalescence, the fluid energy rises almost exponentially with growth rate $\gamma_c = 3.8 \times 10^{-2}$ ($\gamma_c > \gamma_L, \gamma_{L/2}$). While the kinetic energy only accounted for 0.04% of the magnetic energy up to $t = 720 \tau_A$, it accounts for 10% of it in the merged phase, 220 times the saturation value for the island formation stage. In the merged phase, the kinetic energy presents oscillations whose period $\tau = 80 \tau_A$, with τ_A defined with respect to the asymptotic field, roughly equivalent to oscillations at the Alfvén frequency

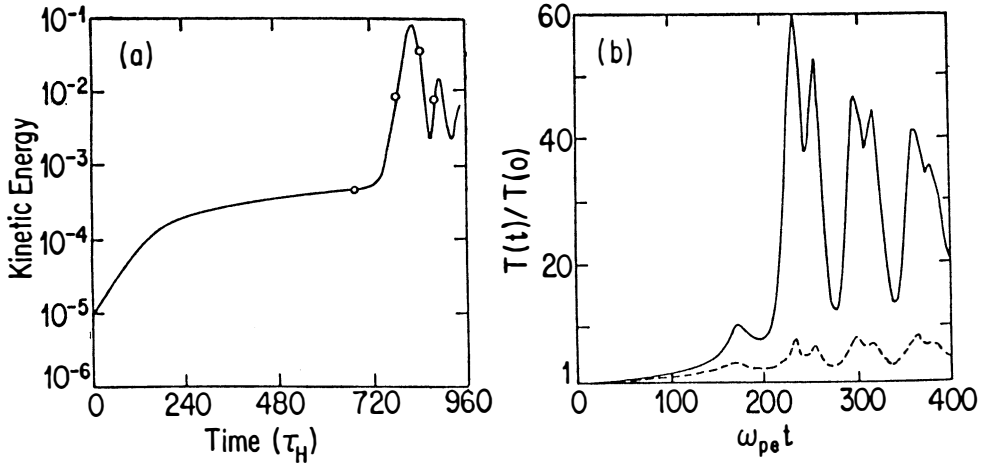


Fig. 9 Comparative data from particle simulations and MHD simulations. a) Ion (full curve) and electron (dotted curve) temperatures in the x -direction for the 128×32 case with $B_t/B_p = 0$. plotted as a function of time. b) Time evolution of the kinetic energy for the MHD simulation of island coalescence induced by nonlinear tearing modes with $S = 2000$. Note the oscillations on both at $\tau \sim \tau_A$, with the poloidal field measured at the island. (Wu, Leboeuf, Tajima- Dawson, 1982)

determined with the field at the island. These oscillations and the larger energy gain upon coalescence are similar to what we observe in the particle simulations.

V. APPLICATION TO SOLAR FLARES

Recent direct observations in soft X-rays (Howard and Svetska, 1977) of interconnecting coronal loops spur the theorist to consider loop coalescence as an important process for solar flares and coronal X-ray brightening phenomena. Another recent observation (Forrest et al., 1982) of amplitude oscillations in gamma-ray emission from the impulsive phase of a solar flare adds curiosity and an important clue to the underlying physical process. The nonlinear development of the coalescence instability of the current loops might provide a coherent explanation of the above observations (Tajima, Brunel and Sakai, 1982). Some of the results presented here offer a quantitative and natural explanation of such known characteristics as the impulsive nature of flares, the time scale of the impulsive phase, intense heating by flares, and formation of the high energy tails on the particle distributions.

The following scenario has been proposed by Tajima, Brunel and Sakai (1982). The flare loop slowly expands after it emerges from the photosphere as the toroidal field curvature of the loop makes the centrifugal motion. In time, the toroidal current J_t builds up, increasing the poloidal magnetic field B_p . As the poloidal field B_p reaches the critical value that is of the order of magnitude B_t , the adjacent flare current loops can now coalesce rapidly facilitated by the fast reconnection process governed by Eq. (7), the faster second phase. Such a fast coalescence of flare loops proceeds explosively once in its nonlinear regime in a matter of one or two Alfvén times, releasing more than one-tenth of the magnetic energy into (ion) kinetic energy.

For the flare loop magnetic field (100 Gauss) with current rod size ($a = 10^8$ cm), the energy density is $W_c \sim 0.5 \times 10^{20} \ln(L/a) \sim 1.5 \times 10^{20}$ erg/cm and the energy available in length $= L$ ($\sim 10^9$ cm) is $E = 1.5 \times 10^{29}$ erg for $a = 10^8$, $d = L = 10^9$ and $E = 1.5 \times 10^{31}$ erg for $a = 10^9$, $d = L = 10^{10}$. The released ion energy is $E_{ion} \sim E/6$ and is in between 2×10^{28} and 2×10^{30} erg due to coalescence. This amount of energy is in the neighborhood of the solar flare energy (Sturrock, 1980). These energies can be released during the impulsive phase as well as during the main phase.

With this magnetic field, the Alfvén time is of the order of 1–3 s, which is approximately the time scale for fast coalescence. The time scale for the impulsive phase is observed to be of the order of a few seconds. The sudden nature of the impulsive flare phase (Sturrock, 1980) is thus explained by increasing the field aligned current and by the faster second phase reconnection in the course of coalescence. The field aligned particle distribution $f(p_z)$ of Fig. 8 should represent approximately the energy observed in gamma rays from the flare loop interface with the photosphere where the energetic particles react with dense photospheric nuclei. The X-ray spectra represent the electron energy distribution, which also shows the oscillatory characteristics in parallel with the ions characteristics. Observation of these radiation spectra by Chupp, Forrest and Suri (1975) shows that the soft X-ray energy domain (up to 400 keV) and hard X-ray domain (up to 7 MeV) have different distribution characteristics: in the hard X-ray domain (700 keV–7 MeV) the energy spectrum is exponential. This type of characteristic seems to match the simulation results of Fig. 8, where the particle distribution breaks into the bulk, the $\exp(-p_z/p_0)$ domain (energy up to a typical temperature 10–50 times of the bulk temperature), and the flat low-population relativistic domain. The amplitude of the oscillation (~ 1 Alfvén time) and its more minute characteristics, resemble what is reported of the solar gamma ray amplitude oscillations (Forrest et al., 1982).

VI. DISCUSSION

We have examined through collisionless particle simulations some of the phenomena associated with current sheet formation, tearing of the sheet to form a chain of x-points and o-points and finally island coalescence. The analysis of these phenomena is far from complete. Nevertheless, the measured reconnection rates in the island formation stage can be matched with theoretical results from an analysis which is a modification of the Sweet–Parker reconnection rate by plasma compressibility. The effective resistivity is supplied in the collisionless case by wave–particle interactions and turbulent electron orbit modifications. The coalescence instability leads to an explosive increase of the reconnection rate. The consequences of tearing on the plasma are minimal in terms of particle energy gains. The consequences of the coalescence instability are large ion temperature increases and large temperature oscillations in the merged phase. The energy increase is accounted for by the loss of potential energy of the attracting current filaments, i.e. loss of poloidal magnetic energy. The oscillations in temperature are explained simply by the oscillations of the merged island at its magnetosonic frequency. It has been interesting to note that similar phenomena are observed in MHD simulations of reconnection and island coalescence even though both types of simulations cover vastly differing spatial scales. Finally, the nonlinear development of the coalescence instability seems to account for the im-

pulsive nature of some types of solar flares, their time scale, intense plasma heating by flares and formation of high energy tails on the particle distributions.

ACKNOWLEDGMENTS

This work was supported by the National Science Foundation grant ATM 82-14730 and Department of Energy, Office of Fusion Energy grant DE-FG05-80-ET-53088.

REFERENCES

- Amano, K., and T. Tsuda, Reconnection of magnetic field lines by clouds-in-cells plasma model, *J. Geomag. Geoelectr.* **29**, 9, 1977.
- Bhattacharjee, A., F. Brunel, and T. Tajima, Magnetic reconnection driven by the coalescence instability, *Phys. Fluids* **26**, 3322, 1983.
- Brunel, F., T. Tajima, and J. M. Dawson, Fast magnetic reconnection processes, *Phys. Rev. Letts.* **49**, 323, 1982.
- Brunel, F., and T. Tajima, Confinement of a high-beta plasma column, *Phys. Fluids* **26**, 535, 1983.
- Chupp, E. L., D. J. Forrest., A. N. Suri, High energy gamma-ray radiation above 300 keV associated with solar activity, in *Solar Gamma-, X-, and EUV radiation*, Ed. by S. R. Kane, p. 341, Reidel, Dordrecht, Holland, 1975.
- Dickman, D. O., R. L. Morse, and C. W. Nelson, Numerical simulation of axisymmetric, collisionless, finite- β plasma, *Phys. Fluids* **12**, 1708, 1969.
- Drake, J. F., and Y. C. Lee, Nonlinear evolution of collisionless and semicollisional tearing modes, *Phys. Rev. Letts.* **39**, 453, 1977.
- Forrest, D. J., E. L. Chupp, J. M. Ryan, C. Reppin, E. Rieger, G. Kanbach, K. Pinkau, G. Share and G. Kinzer, Evidence for impulsive ion acceleration during the 0312UT flare of 1980 June 7, in *Proceedings of the 17th International Cosmic Ray Conference, Paris, France, 1981*, to be published.
- Galeev, A. A., F. V. Coroniti, M. Ashour-Abdalla, Explosive tearing mode reconnection in the magnetospheric tail, *Geophys. Res. Lett.* **5**, 707, 1978.
- Gekelman, W., and R. L. Stenzel, Magnetic field line reconnection experiments, 2. Plasma parameters, *J. Geophys. Res.*, **86**, A2, 659, 1981.
- Hamilton, J. E. M., J. W. Eastwood, The effect of a normal magnetic field component on current sheet stability, *Planet. Space Sci.* **30**, 293, 1982. 2 10
- Howard, R., and Z. Svetska, Development of a complex of activity in the solar corona, *Solar Phys.* **54**, 65, 1977.
- Katanuma, I., and T. Kamimura, Collisionless tearing instabilities, *Phys. Fluids*, **23**, 2500, 1980.
- Leboeuf, J. N., T. Tajima and J. M. Dawson, Magnetic x-points, islands coalescence and intense plasma heating, in *Physics of Auroral Arc Formation*, Ed. by S. I. Akasofu and J. R. Kan, p. 337, AGU, Washington, D. C., 1981.
- Leboeuf, J. N., T. Tajima and J. M. Dawson, Dynamic x-points, *Phys. Fluids*, **25**, 784, 1982.

- Parker, E. N., *Cosmical magnetic Fields*, Chapter 15, Clarendon Press, Oxford, 1979.
- Rutherford, P., Nonlinear growth of the tearing mode, *Phys. Fluids* **16**, 1903, 1973.
- Stenzel, R. L., and W. Gekelman, Experiments on magnetic field line reconnection, *Phys. Rev. Letts.* **42**, 1055, 1979.
- Sturrock, P. A., Flare models, in *Solar Flares: A Monograph from Skylab Solar Workshop II*, Ed. P. A. Sturrock, p. 411, Colorado Associated University Press, Boulder, 1980.
- Tajima, T., Tearing and Reconnection, in *Fusion Energy - 1981 (Interkational Centre for for Theoretical Physics, Trieste, 1982)*, p. 403. International Atomic Energy Agency, Vienna, Austria, 1982.
- Tajima, T., F. Brunel and J. Sakai, Loop coalescence in flares and coronal x-ray brightening, *Astrophys. J.*, **258**, L45, 1982.
- Tajima, T., F. Brunel, J. Sakai, L. Vlahos and M. Kundu, The coalescence instability in solar flares, *Proceedings of the IAU conference on Tnstable Current Systems in Astrophysical Plasmas*, Ed. by M. Kundu, IAU, 1985. P 197. (North-Holland)
- Terasawa, T., Numerical study of explosive tearing mode instability in one-component plasmas, *J. Geophys. Res.* **86**, 9007, 1981.
- Wu, C. C., J. N. Leboeuf, T. Tajima and J. M. Dawson, Magnetic islands coalescence and intense plasma heating, University of California at Los Angeles, Plasma Physics Group Report No. PPG-551, 1981. 511

This paper was presented on Chapman Conference on Magnetic Reconnection held at the Los Alamas National Laboratory, U.S.A. October 3-7, 1983.

(Received October 31. 1984)

三角行列分解と行列リーマン・ヒルベルト問題

富山大学工学部情報処理 川 田 勉

1. 緒 言

いわゆる逆散乱法とは、解きたい非線形発展方程式を A) あるスペクトラル方程式と同伴する時間方程式に分解し、B) 逆スペクトラル理論により解こうとするものであり、これによって設定された初期値問題は一連の線形演算に帰着される。指定された非線形方程式に対し A) のプロセスが可能かどうかは一般的には非常に難しい問題である。直接 A) のプロセスを考える代りに、まず B) を考え、ついで時間発展方程式と連立して、解ける非線形方程式のリストを作っていく。この立場に立つと、どの程度迄のスペクトラル方程式の逆理論が構成できるかという事が重要となってくる。この事自身も簡単な事ではないが、従来迄の結果を拡張するという試みが、高階化、多次元化の方向で努力されている。本文では、高階系への拡張という方向を議論するものであり、以下、時間を省く。正規形の行列スペクトラル方程式 $\Phi_x = Q\Phi$ で考える。この際 Q の構造を、どの様にするかという問題があるが行列のオーダーを M (2, 3, ...) とする以外は、次の形に限定する。

$$\Phi_x = (i\lambda A + Q(x))\Phi \quad (1.1 a)$$

λ はスペクトラル・パラメーターで一般に複素数 ($\lambda = \zeta + i\eta$) である、又 A は対角実定数行列、

$$A \triangleq \text{diag.} \{a_1, a_2, \dots, a_M\}, \quad a_1 < \dots < a_M, \quad (1.1 b)$$

$Q(x)$ は、非対角ポテンシャル行列である。 $M=3$ の時は、有名な三波相互作用方程式のスペクトラル問題であり、すでに Zakharov-Manakov⁽¹⁾, Kaup⁽²⁾ によって解かれている。我々は、三波相互作用方程式の考察を行い、jost 函数 $\Phi(\lambda, x)$ の完全性、逆問題を解く Gel'fand-Levitan 形積分方程式の一般化、線形化された三波相互作用方程式の解となる“2乗固有函数”とその完全性、更には線形化方程式の非斉次一般解の構成を行った⁽³⁾。これらは、形式的にはうまく遂行されたのであるが、数学的厳密性に欠けている。従来の 2×2 では生じなかった jost 函数の解析接続の困難が原因となって、G-L 方程式の一般化に必要な変換演算子の積分核表示、jost 函数の完全性条件等が不明確に定義されたのである。他方、素粒子論等においては、アイソトピック空間に対応した高階系への拡張が重要である。Zakharov 等に始まるリーマン・ヒルベルト問題による扱いがあり、^(4,5) “解析的因子分解法”^(6,7) によって、ソリトン解が直接的に構成できる。けれど、この方法は初期値問題を解く事ができなかった。最近、我々は、この方法が連続スペクトラムの存在する問題も含めて、従来の逆散乱に完全に対応できる事を $M=2$ の典型である AKNS 方程式⁽⁸⁾ について示した。^(9,10) 所で $M=3$ なる式 (1.1) にも行列リーマン・ヒルベルト問題を導出できる⁽³⁾ が、留意すべきは AKNS 方程式の際⁽⁹⁾ も同様、jost 函数の解析性の既知な事実を使っている点であり、逆散乱理論を構築しようという本文の主旨にそぐわない。これは、ともかく jost 函数の解析性を明かにする事の重要性に他ならない。

式 (1.1 a) で、 $Q(x)$ は $x \rightarrow \pm\infty$ で急減少 (もっと強く、ある閉区間 $a \leq x \leq b$ 以外で零としても

良い。)とする。この時 $\exp(i\lambda Ax)$ を式(1.1)の真空解と呼ぶ。ここで次の行列を導入する、

$$\Psi(\xi, x) \triangleq \exp(-i\xi Ax) \cdot \Phi(\xi, x), \quad (\xi = \text{Re. } \lambda) \quad (1.2)$$

簡単な計算から、これは (x, ξ) に関し一様に有界で、 $x \rightarrow \pm\infty$ で $\Psi(\xi, x) \rightarrow C^\pm(\xi)$ とでき、 x 独立な散乱行列 $S(\xi)$ が定義できる。

$$S(\xi) \triangleq C^+(\xi)[C^-(\xi)]^{-1}. \quad (1.3)$$

問題は、複素数 λ に対し定義可能な行列を見出す事である。Caudrey⁽¹¹⁾によれば、次の函数

$$\Theta(\lambda, x) \triangleq \Phi(\lambda, x) \exp(-i\lambda Ax) \quad (1.4)$$

が、それを与える。然るに、 Θ の方程式

$$\Theta x = i\lambda[A, \Theta] + Q(x)\Theta, \quad ([A, \Theta] = A\Theta - \Theta A) \quad (1.5)$$

は、次の変換に関し不変である、

$$\Theta \rightarrow \Theta^1 = \Theta e^{-iAx} G(\lambda) e^{-i\lambda Ax}. \quad (1.6)$$

この不変性がリーマン・ヒルベルト問題に転化していくのだが、この時(1.6)式右辺の行列 G を散乱行列 S で表示せねばならない。式(1.4)で $x \rightarrow \pm\infty$ とすると判る様に、 Θ の (λ, x) に関する一様有界性から、 $C^\pm(\lambda)$ 従って $\Theta(x = \pm\infty)$ が下三角又は上三角行列とならねばいけない。この重要な事実は、すでに文献(3)に表れていたが、実はShabatが最初に示したものである。⁽¹²⁾彼は、この三角行列を使って逆散乱理論の数学的構成を行っている。この三角行列は、行列 S で G を定める際の媒介を行うが、この際に尤長度が存在し、これを適当に処理せねばならない。換言すれば、式(1.1)に対する行列リーマン・ヒルベルト問題は一意に定まらないのである。⁽¹³⁾一方この性質を利用すれば、最も簡潔なリーマン・ヒルベルト問題を与える事ができる。^(13,14)これを主リーマン・ヒルベルト問題と呼ぼう。この選択も含めて、一般の M に対し、リーマン・ヒルベルト問題の具体的表示を与えるのは簡単でない。本文の主たる目的は、この部分の解明にある。散乱行列の一意的三角行列分解が研究され、その逐次表示が与えられる。この分解と、先の三角行列を比較する事によって尤長度の削除が行われる。

2. スペクトラル解の解析性

式(1.2)で導入された $\Psi(\xi, x)$ は、次の積分方程式を満たす。

$$\Psi(\xi, x) = C^\pm(\xi) + \int_{\pm\infty}^x e^{-i\xi Ay} Q(y) e^{i\xi Ay} \Psi(\xi, y) dy. \quad (2.1)$$

これはVolterra型なので、Neumann級数は $Q(x)$ の条件から (ξ, x) に関し一様に収束する。そこで次の函数を考える。

$$S(\xi, x) \triangleq \Psi(\xi, x)[C^-(\xi)]^{-1}. \quad (2.2)$$

式(1.3)から $x \rightarrow +\infty$ について $S(\xi, x) \rightarrow S(\xi)$ となる。所で(2.1), (2.2)式から

$$S(\xi, x) = E + \int_{-\infty}^x e^{-i\xi Ay} Q(y) e^{i\xi Ay} S(\xi, y) dy. \quad (2.3)$$

$S(\xi, x)$ は、 (ξ, x) に関し有限であり、そこで第 j 列ベクトル $s_j(\xi, x)$ を取り出し、Neumann 級数に展開し、 $1/\xi$ のべきを取り出す。

$$s_j(\xi, x) = |j\rangle + \int_{-\infty}^x e^{-i\xi A y} Q(y) e^{i\xi A y} s_j(\xi, y) dy = \sum_{n=0}^{\infty} I_n(\xi, x). \quad (2.4)$$

$I_n(x)$ は、次の逐次列で与えられる。

$$I_{n+1}(\xi, x) = \sum_{k,l=1}^M \int_{-\infty}^x |k\rangle q_l^k(y) e^{-i\xi(a_k - a_l)y} \langle l| I_n(\xi, y) dy, \quad I_1 = |j\rangle. \quad (2.5)$$

但し $Q = \sum |k\rangle q_l^k \langle l|$. $1/\xi$ のオーダーを評価する、指数函数に注意して部分積分を行って、

$$I_2(\xi, x) = -\frac{1}{i\xi} \sum_{k(\neq j)} |k\rangle \frac{q_l^k(x)}{a_k - a_j} e^{-i\xi(a_k - a_j)x} + O(\xi^{-2}),$$

$$I_3(\xi, x) = -\frac{1}{i\xi} |j\rangle \sum_{l(\neq j)} \int_{-\infty}^x \frac{q_l^j(y) q_l^j(y)}{a_l - a_j} dy + O(\xi^{-2}),$$

$I_3 \cong \xi^{-1} |j\rangle$ を (2.5) 式に用いれば、 $I_4(\xi, x) = O(\xi^{-2})$ をえる。結局、次式となる。

$$s_j(\xi, x) - |j\rangle = -\frac{1}{i\xi} \left\{ \sum_{k(\neq j)} |k\rangle \frac{q_l^k(x)}{a_k - a_j} e^{-i\xi(a_k - a_j)x} + |j\rangle \sum_{l(\neq j)} \int_{-\infty}^x \frac{q_l^j(y) q_l^j(y)}{a_l - a_j} dy \right\} + O(\xi^{-2}). \quad (2.6)$$

問題は複素面上での議論である。すでに述べたが式(1.4)の Θ がこれを可能にする事を示そう。

式(1.5)を積分方程式に直す。 $\Theta |j\rangle = \theta_j, c_j$ を積分定数として Fredholm 型方程式をえる、

$$\theta_j(\lambda, x) = c_j |j\rangle - \left\{ K_j \int_{-\infty}^x + (E + K_j) \int_x^{\infty} \right\} e^{i\lambda(A - a_j)(x-y)} Q(y) \theta_j(\lambda, y) dy. \quad (2.7)$$

対角定数 K_j は、後で適当に定められる。Fredholm 型では Volterra 型の様に簡単に収束しない。

$M=2$ のケースでは、この状態を避けて、 θ_1, θ_2 を共に Volterra 型に帰着できる。 $M \geq 3$ では、それは不可能である。 θ_j が有界となる様に K_j を設定できる事に注目する。簡単にいえば、積分内の指数項の発散を消す様に K_j を選択する。明らかに全 λ 面上で指数項を押えられなく、上半面と下半面に分けて考える必要がある。上・下半面に対し、式(2.7)の各量に肩字 "P, N" を付加して区別する。この時、各 K_j は 1 ヶの自由度を残して定まる、

$$K_j^P = \begin{pmatrix} & & & (j) \\ & -1 & & \\ & & -1 & \\ (j) & & & k_j^P \\ & & & & 0 \\ & & & & & 0 \end{pmatrix}, \quad K_j^N = \begin{pmatrix} & & & (j) \\ & 0 & & \\ & & 0 & \\ (j) & & & k_j^N \\ & & & & -1 \\ & & & & & -1 \end{pmatrix}. \quad (2.8)$$

この $K_j^{P,N}$ に対し $\theta_j^{P,N}$ は上・下半面で解析函数となる。さて、式(2.7)によれば、

$$\lim_{x \rightarrow \infty} \theta_j^P(\lambda, x) = c_j^P(\lambda) |j\rangle - \lim_{x \rightarrow \infty} e^{i\lambda(A - a_j)(x-b)} \cdot K_j^P \int_{-\infty}^x e^{i\lambda(A - a_j)(b-y)} \theta_j^P(\lambda, y) dy. \quad (2.9)$$

但し、 $Q(x)$ は $a \leq x \leq b$ 以外では零 (Compact support) とした。式(2.8)から、列ベクトル $\theta_j^P(x = \infty)$ の

第1～第j成分のみが値を持ち、従って行列 $\Theta^P(x=\infty)$ は上三角行列 U^P となる。その際、式(2.9)の積分項の前に出した指数部は $|\lambda|=\infty$ で解析的とならない。この事を式で示せば、上半面で解析的な三角行列 $U^P(\lambda)$ が存在して、 $x \rightarrow \infty$ について

$$\Theta^P(\lambda, x) \rightarrow e^{i\lambda A(x-b)} U^P(\lambda) e^{-i\lambda A(x-b)} \quad (2.10)$$

と書け、更に次の行列は(対角成分は別にして) $\text{Im } \lambda = +\infty$ を解析域に含まない。

$$U_0^P(\lambda) = e^{-i\lambda Ab} U^P(\lambda) e^{i\lambda Ab}. \quad (2.11)$$

他のケースもまとめよう。 $x \rightarrow \{-\infty, +\infty\}$ に応じて

$$\Theta^P(\lambda, x) \rightarrow e^{i\lambda Ax} \{L_0^P(\lambda), U_0^P(\lambda)\} e^{-i\lambda Ax}, \quad (2.12 a)$$

$$\Theta^N(\lambda, x) \rightarrow e^{i\lambda Ax} \{U_0^N(\lambda), L_0^N(\lambda)\} e^{-i\lambda Ax}. \quad (2.12 b)$$

さて、これ以降の議論には、式(1.1)の随判系を導入せねばならない。

$$\tilde{\Phi}_x = -(i\lambda A + Q^T(x)) \tilde{\Phi}.$$

省略するが、随判系の各量(チルドを付す)は、今迄のと同様に導入する。但し、

$$\tilde{\Phi} \triangleq e^{-i\lambda Ax} \tilde{\Phi}, \quad \tilde{\Theta} \triangleq \tilde{\Phi} e^{-i\lambda Ax}.$$

式(2.12)に相当するものは、 $x \rightarrow \{-\infty, +\infty\}$ に対し

$$\tilde{\Theta}^P(\lambda, x) \rightarrow e^{-i\lambda Ax} \{\tilde{U}_0^P(\lambda), \tilde{L}_0^P(\lambda)\} e^{i\lambda Ax}, \quad (2.12 c)$$

$$\tilde{\Theta}^N(\lambda, x) \rightarrow e^{-i\lambda Ax} \{\tilde{L}_0^N(\lambda), \tilde{U}_0^N(\lambda)\} e^{i\lambda Ax}. \quad (2.12 d)$$

式(1.6)の不変性を使って $x = \pm\infty$ で規格化された解 Θ_{\pm} を構成する、

$$\begin{aligned} \{\Theta_-, \Theta_+\} &= \Theta^P e^{i\epsilon Ax} \{[L_0^P]^{-1}, [U_0^P]^{-1}\} e^{-i\epsilon Ax} \\ &= \Theta^N e^{i\epsilon Ax} \{[U_0^N]^{-1}, [L_0^N]^{-1}\} e^{-i\epsilon Ax}, \end{aligned} \quad (2.13 a)$$

$$\begin{aligned} \{\tilde{\Theta}_-, \tilde{\Theta}_+\} &= \tilde{\Theta}^P e^{-i\epsilon Ax} \{[\tilde{U}_0^P]^{-1}, [\tilde{L}_0^P]^{-1}\} e^{i\epsilon Ax} \\ &= \tilde{\Theta}^N e^{-i\epsilon Ax} \{[\tilde{L}_0^N]^{-1}, [\tilde{U}_0^N]^{-1}\} e^{i\epsilon Ax}. \end{aligned} \quad (2.13 b)$$

$x \rightarrow \pm\infty$ に対し、明かに $\Theta_{\pm}, \tilde{\Theta}_{\pm} \rightarrow E$ である。又、簡単な計算から

$$\frac{d}{dx} [\tilde{\Theta}_{\pm}^{\pm} \Theta_{\pm}] = i\xi [A, \tilde{\Theta}_{\pm}^{\pm} \Theta_{\pm}]$$

であり、従って

$$\tilde{\Theta}_{\pm}^{\pm}(\xi, x) \Theta_{\pm}(\xi, x) = E. \quad (2.14)$$

式(2.13)を(2.14)に代入すると、上下半面に解析接続できる行列 $G^{P,N}(\lambda)$ が定義できる。仮りに、 $G^P(\lambda)$ を取り上げると、

$$G^P \triangleq [\tilde{\Theta}^P]^T \Theta^P = e^{i\xi Ax} [\tilde{U}_0^P]^T L_0^P e^{-i\xi Ax},$$

指数項が存在しても上半面で解析的なのだから、 $[\tilde{U}_0^P]^T L_0^P$ 、従って G^P は対角行列でなければならない。この関係をまとめると、

$$G^P \triangleq [\tilde{\Theta}^P]^T \Theta^P = [\tilde{U}_0^P]^T L_0^P = [\tilde{L}_0^P]^T U_0^P, \quad (2.15 a)$$

$$G^N \triangleq [\tilde{\Theta}^N]^T \Theta^N = [\tilde{L}_0^N]^T U_0^N = [\tilde{U}_0^N]^T L_0^N. \quad (2.15 b)$$

更に式 (2.13) より散乱行列と (1.6) 式で示した行列 G に関して、次の関係が成立つ、

$$\begin{cases} S(\xi) = e^{-i\xi Ax} [\Theta_+(\xi, x)]^{-1} \Theta_-(\xi, x) e^{i\xi Ax}, \\ S(\xi) = e^{i\xi Ax} [\tilde{\Theta}_+(\xi, x)]^{-1} \tilde{\Theta}_-(\xi, x) e^{-i\xi Ax}, \end{cases} \quad (2.16)$$

$$\begin{cases} [\Theta^N(\xi, x)]^{-1} \Theta^P(\xi, x) = e^{i\xi Ax} G(\xi) e^{-i\xi Ax}, \\ [\tilde{\Theta}^N(\xi, x)]^{-1} \tilde{\Theta}^P(\xi, x) = e^{-i\xi Ax} \tilde{G}(\xi) e^{i\xi Ax}. \end{cases} \quad (2.17)$$

式 (2.12) を考慮して、行列 S, G 等を三角行列 (L, U) で書ける。

$$S = U_0^P (G^P)^{-1} [\tilde{U}_0^P]^T = L_0^N (G^N)^{-1} [\tilde{L}_0^N]^T, \quad (2.18 a)$$

$$\tilde{S} = \tilde{U}_0^N (G^N)^{-1} [U_0^N]^T = \tilde{L}_0^P (\tilde{G}^P)^{-1} [L_0^P]^T, \quad (2.18 b)$$

$$G = [G^N]^{-1} [\tilde{U}_0^N]^T U_0^P = [G^N]^{-1} [\tilde{L}_0^N]^T L_0^P, \quad (2.19 a)$$

$$\tilde{G} = [G^N]^{-1} [U_0^N]^T \tilde{U}_0^P = [G^N]^{-1} [L_0^N]^T \tilde{L}_0^P, \quad (2.19 b)$$

式 (2.15), (2.18) より次式が成立つ、

$$\tilde{S}^T(\xi) S(\xi) = E. \quad (2.20)$$

$S = [s_{ij}]$ として、次の様な主小行列式を定義しよう、

$$\det_j S \triangleq \begin{pmatrix} s_{11} & \cdots & s_{1j} \\ \vdots & & \vdots \\ s_{j1} & \cdots & s_{jj} \end{pmatrix}, \quad \det^k S \triangleq \begin{pmatrix} s_{k1} & \cdots & s_{kM} \\ \vdots & & \vdots \\ s_{M1} & \cdots & s_{Mk} \end{pmatrix}. \quad (2.21)$$

式 (2.11) と $\det_j(LU) = \det_j L \cdot \det_j U$ 等に留意して、式 (2.18) から次の関係をえる。

$$\det_j \tilde{S} = \det_j L^N \cdot \det_j \tilde{L}^N / \det_j G^N, \quad \det^k S = \det^k U^P \cdot \det^k \tilde{U}^P / \det^k G^P, \quad (2.22 a)$$

$$\det_j \tilde{S} = \det_j \tilde{L}^P \cdot \det_j L^P / \det_j G^P, \quad \det^k \tilde{S} = \det^k \tilde{U}^N \cdot \det^k U^N / \det^k G^N, \quad (2.22 b)$$

明らかに $(\det_j \tilde{S}, \det^k S)$ は、上半面で、 $(\det_j S, \det^k \tilde{S})$ は下半面で解析的となる。

3. リーマン・ヒルベルト問題

すでに述べた様に、式 (2.17) がリーマン・ヒルベルト問題になっていく。その際、行列 G, \tilde{G} を各 S 行列要素を使って表示したい。而るに、式 (2.18), (2.19) から判るのだが、一意にそれを行えない。その理由は、任意な行列の一意的三角分解は対角成分を 1 とする “強”(上・下) 三角行列 (U, L) と対角行列 (D) の積の形 (LDU 又は UDL で与えられるのに対し、式 (2.18) に使われた三角行列の対角成分は 1 でないからである。この部分を明確にするために、とにかく S 行列の一意的分解を定義する。

$$S \triangleq S_L^N S_D^N S_U^N = S_L^U S_D^U S_U^U, \quad \tilde{S} \triangleq \tilde{S}_L^U \tilde{S}_D^U \tilde{S}_U^U = \tilde{S}_L^N \tilde{S}_D^N \tilde{S}_U^N \quad (3.1)$$

ここに $S_{L,U}$ 等は強三角, S_D は対角, 肩字 P, N は主小行列式 (2.22) との比較による対角部分 S_D, \tilde{S}_D の上・下半面における解析性に依じて付加された。つまり (S_L^N, \tilde{S}_L^N) は下半面で、 (S_D^U, \tilde{S}_D^U) は上半面で解析的である。式 (3.1) を (2.20) に代入すると、

$$\tilde{S}_L^U S_D^U = \tilde{S}_L^N S_D^N = E, \quad (3.2 a)$$

$$(\tilde{S}_L^U)^T S_D^U = (\tilde{S}_L^N)^T S_D^U = (\tilde{S}_L^N)^T S_D^N = (\tilde{S}_L^N)^T S_D^U = E. \quad (3.2 b)$$

式 (2.17) の左辺の逆行列を式 (2.15) で書き直す事ができる、

$$[(\tilde{\Theta}^N)^T \Theta^P = e^{i\epsilon Ax} G_{NP} e^{-i\epsilon Ax}, \quad [(\tilde{\Theta}^P)^T \Theta^N = e^{i\epsilon Ax} G_{PN} e^{-i\epsilon Ax}. \quad (3.3 a)$$

但し、

$$G_{NP} = [\tilde{U}_0^N]^T U_0^P = [\tilde{L}_0^N]^T L_0^P, \quad G_{PN} = [\tilde{U}_0^P]^T U_0^N = [\tilde{L}_0^P]^T L_0^N. \quad (3.3 b)$$

ここで、 U_0, L_0 等を強三角行列 (L_1, U_1 等) と対角行列 (D_L, D_U 等) に一意分解しよう、

$$L_0^{P,N} = L_1^{P,N} D_L^{P,N}, \quad U_0^{P,N} = U_1^{P,N} D_U^{P,N}, \quad \tilde{L}_0^{P,N} = \tilde{L}_1^{P,N} \tilde{D}_L^{P,N}, \quad \tilde{U}_0^{P,N} = \tilde{U}_1^{P,N} \tilde{D}_U^{P,N}. \quad (3.4)$$

これを式 (2.18) に代入し、式 (3.1) と比較すれば、まず強三角部分は

$$\begin{cases} S_L^N = L_1^N, S_U^N = [\tilde{L}_1^N]^T, & S_L^U = [\tilde{U}_1^U]^T, S_D^U = U_1^U, \\ \tilde{S}_L^U = \tilde{L}_1^U, \tilde{S}_D^U = [L_1^U]^T, & \tilde{S}_L^N = [U_1^N]^T, \tilde{S}_U^N = \tilde{U}_1^N, \end{cases} \quad (3.5 a)$$

と一意に対応する。これと (3.2 b) を使って式 (2.15) を整理すれば

$$G^P = \tilde{D}_U^U D_L^U = \tilde{D}_L^L D_U^L, \quad G^N = \tilde{D}_L^L D_U^L = \tilde{D}_U^U D_L^U. \quad (3.6)$$

これを (3.5 a) に対応する対角成分の関係に適用すると、

$$\begin{cases} S_D^U = D_L^U [D_U^L]^{-1} = \tilde{D}_L^L [\tilde{D}_U^U]^{-1} = [\tilde{S}_D^N]^{-1}, \\ S_D^L = D_U^L [D_L^U]^{-1} = \tilde{D}_U^U [\tilde{D}_L^L]^{-1} = [\tilde{S}_D^U]^{-1}. \end{cases} \quad (3.5 b)$$

明かに冗長があって、 $S_D^{P,N}$ 等を与えても $D_L^{P,N}$ 等は定まらない。少し吟味すれば判るが、 $D_L^{P,N}$ を固定すれば他は定まる。特に、次の選定が許される。

$$D_{\xi}^{P,N} = \widetilde{D}_{\xi}^{P,N}. \quad (3.7)$$

以下、この条件下で議論を進める。先の関係式 (3.6), (3.5 b), (3.3 b) は、次の様になる、

$$G^P = D_0^P D_{\xi}^P, \quad G^N = D_0^N D_{\xi}^N, \quad (3.8)$$

$$S_B^N = D_{\xi}^N (D_0^N)^{-1} = [\widetilde{S}_B^N]^{-1}, \quad S_B^P = D_{\xi}^P (D_0^P)^{-1} = [\widetilde{S}_B^P]^{-1}, \quad (3.9)$$

$$G_{NP} = D_{\xi}^N (\widetilde{S}_B^N)^T S_B^P D_0^P = D_{\xi}^N S_N (\widetilde{S}_B^P)^T D^P, \quad (3.10 a)$$

$$G_{PN} = D_{\xi}^P S_P (\widetilde{S}_B^N)^T D_0^N = D_{\xi}^P (\widetilde{S}_B^P)^T S_N D_{\xi}^N. \quad (3.10 b)$$

付録に示した関係(A.3), (A.7), (B.2 a), (B.3 a)等によれば、式(3.9)の対角行列は、

$$S_B^N = \text{diag.} \left[s_{11}, \frac{\mu_2^N}{s_{11}}, \frac{\mu_3^N}{\mu_2^N}, \dots, \frac{\widetilde{s}_{MN}}{\mu_{M-2}^N}, \frac{1}{\widetilde{s}_{MM}} \right], \quad (3.11 a)$$

$$S_B^P = \text{diag.} \left[\frac{1}{s_{11}}, \frac{\widetilde{s}_{11}}{\mu_2^P}, \frac{\mu_2^P}{\mu_3^P}, \dots, \frac{\mu_{M-2}^P}{s_{MM}}, s_{MM} \right]. \quad (3.11 b)$$

ここに $\mu_j^{P,N}$ は (B.4) 式の一般化であり、 $2 \leq j \leq M-2$ の時に存在する。

$$\mu_j^N \triangleq |s_{11}, \dots, s_{jj}| = |\widetilde{s}_{j+1,j+1}, \dots, \widetilde{s}_{MM}|, \quad \mu_j^P \triangleq |\widetilde{s}_{11}, \dots, \widetilde{s}_{jj}| = |s_{j+1,j+1}, \dots, s_{MM}|. \quad (3.12)$$

これによれば、 $\mu_j^{P,N}$ なる函数は $M \leq 4$ で本質的であるといえる。さて、式(3.9), (3.11)から、次の様に (3.7) 式の行列を定める。

$$\begin{cases} D_{\xi}^N = \text{diag.} [s_{11}, \mu_2^N, \dots, \widetilde{s}_{MM}, 1], & D_0^N = \text{diag.} [1, s_{11}, \dots, \mu_{M-2}^N, \widetilde{s}_{MM}], \\ D_{\xi}^P = \text{diag.} [\widetilde{s}_{11}, \mu_2^P, \dots, s_{MM}, 1], & D_0^P = \text{diag.} [1, \widetilde{s}_{11}, \dots, \mu_{M-2}^P, s_{MM}]. \end{cases} \quad (3.13)$$

式(3.10)の主小行列式を取り、(3.9)式を使うと、

$$\det_j (S_B (S_B^N)^{-1}) = \det_j (S_N (\widetilde{S}_B^N)^T), \quad \det^k (S_B (S_B^P)^{-1}) = \det^k ((\widetilde{S}_B^P)^T S_P). \quad (3.14)$$

これは、行列 $D_{\xi}^{P,N}$ の成分に関するスカラー形ローマン・ヒルベルト問題である。 $D_{\xi}^{P,N}(\lambda)$ は上下半面に解析接続でき、 $|\lambda| \rightarrow \infty$ で単位行列に漸近する事から、強三角行列部分を実軸上で与えられれば、 $D_{\xi}^{P,N}$ の各成分は一意に再構成できる事になる。この事実は、強三角行列が連続スペクトルに関する散乱データとなる事を暗示する。さて、例えば (3.10 b) 式の $D_{\xi}^P S_P (\widetilde{S}_B^N)^T D_0^N$ の $(1-1)$, $(M-M)$ 要素を取出そう。 $(1-1)$ 要素は明かに 1 である。一方、 $(M-M)$ 要素は付録 A から $\widetilde{s}_{M1} \widetilde{s}_{M1} + \dots + s_{MM} \widetilde{s}_{MM}$ となるが $S^T S = E$, つまり $\widetilde{s}_{jk} = \sum_m \widetilde{s}_{mj} s_{mk}$ よりやはり 1 となる。従って、

$$G_{NP}^0 \triangleq E - G_{NP}, \quad G_{PN}^0 \triangleq E - G_{PN}, \quad (3.15)$$

を導くと、これらの $(1-1)$, $(M-M)$ 要素は消失する。この事実は、式(3.3 a), (3.15)より得られる解析接続を与える式の簡単化に貢献する、

$$\Theta^P(\lambda, x) = E - \frac{1}{2\pi i} \int_{-\infty}^{\infty} \frac{d\xi}{\xi - \lambda} \Theta^N(\xi, x) e^{i\xi 4x} [G^N(\xi)]^{-1} G_{NP}^0(\xi) e^{-i\xi 4x} \quad (\text{Im } \lambda > 0), \quad (3.16 a)$$

$$\Theta^N(\lambda, x) = E + \frac{1}{2\pi i} \int_{-\infty}^{\infty} \frac{d\xi}{\xi - \lambda} \Theta^P(\xi, x) e^{i\xi 4x} [G^P(\xi)]^{-1} G_{PN}^0(\xi) e^{-i\xi 4x} \quad (\text{Im } \lambda < 0). \quad (3.16 b)$$

これと少し異った関係を次の様に求めることができる。(2.13 a)式等より、次の様な関係をえる。

$$\Theta_+ = \Theta^P [D_1^P]^{-1} e^{i\epsilon Ax} [\tilde{S}_1^P]^T e^{-i\epsilon Ax} \xi = \Theta^N [D_1^N]^{-1} e^{i\epsilon Ax} [\tilde{S}_1^N]^T e^{-i\epsilon Ax}, \quad (3.17 a)$$

$$\Theta_- = \Theta^P [D_1^P]^{-1} e^{i\epsilon Ax} S_1^P e^{-i\epsilon Ax} = \Theta^N [D_1^N]^{-1} e^{i\epsilon Ax} S_1^N e^{-i\epsilon Ax}. \quad (3.17 b)$$

例えば、(3.17 a)式を分解すると、

$$\hat{\theta}_1^P - \hat{\theta}_1^N = -\sum_{k=1}^{j-1} \hat{\theta}_k^P \langle k | [\tilde{S}_1^P]^T | j \rangle e^{i\epsilon \beta_{kj} x} + \sum_{k=j+1}^M \hat{\theta}_k^N \langle k | [\tilde{S}_1^N]^T | j \rangle e^{i\epsilon \beta_{kj} x}. \quad (3.18)$$

但し、 $\Theta^P [D_1^P]^{-1} = (\hat{\theta}_1^P, \hat{\theta}_2^P, \dots)$ 、 $\Theta^N [D_1^N]^{-1} = (\hat{\theta}_1^N, \hat{\theta}_2^N, \dots)$ 又 $\beta_{ki} = a_k - a_i$ である。これは、ベクトル形式のリーマン・ヒルベルト問題であり $\hat{\theta}_1^P, \hat{\theta}_1^N$ に関してのコーシー積分表示をえるが、(3.16)式と同様にその形は解かれていない。これは、従来のケースがすべてそうであった様に、解法はそんなに簡単でない。これとは別に、式(2.7)から判る様に、行列 $\Theta^{P,N}$ はフレドホルム方程式に従うが、次の成分

$$\theta_1^P = \hat{\theta}_1^P = \theta_{1+}, \quad \theta_4^N = \hat{\theta}_4^N = \theta_{+4}, \quad \theta_1^N = \theta_{1-}, \quad \theta_4^P = \theta_{-4} \quad (M=4) \quad (3.19)$$

に限り、ポルテラ方程式に従う。故にこの各成分は、各々の上下半面上に特異点(極)を持たず、 λ 独立な核を持った積分演算子(変換演算子)表現を持つ。 $M=2$ では $\Theta^{P,N}$ の成分は式(3.19)のもののみで、直接逆問題を解く Gel'fand-Levitan 方程式が得られる。これらの事柄が $3 \leq M$ でどうなるかは次節で論じられるが、式(3.18)に現れている行列 $\tilde{S}_1^P, \tilde{S}_1^N$ が散乱データ行列と呼ばれるにふさわしい事と、 $\Theta^{P,N}$ とポテンシャル $Q(x)$ を結ぶ関係が必要であるという事である。行列リーマン・ヒルベルト問題の変分操作を行って、次の表示が求まる、^{10,14)}

$$\begin{aligned} Q(x) &= \frac{1}{2\pi} \int_{-\infty}^{\infty} [A, \Theta^P(\xi, x) [G^P(\xi)]^{-1} e^{i\epsilon Ax} G_{PN}^0(\xi) e^{-i\epsilon Ax}] d\xi \\ &= -\frac{1}{2\pi} \int_{-\infty}^{\infty} [A, \Theta^N(\xi, x) [G^N(\xi)]^{-1} e^{i\epsilon Ax} G_{NP}^0(\xi) e^{-i\epsilon Ax}] d\xi. \end{aligned} \quad (3.20)$$

4. 逆 散 乱

$M=3, 4$ のケースにおける逆理論の構成を考える。 $M=3$ ではポルテラ形(3.19)以外の成分 θ_2^P, θ_3^N が存在するが、式(3.18)によれば

$$\theta_{2+} = \frac{\theta_2^P}{\tilde{S}_{11}} + \theta_3^N \frac{\tilde{S}_{21}}{\tilde{S}_{11}} e^{i\epsilon \beta_{12} x} = \frac{\theta_2^N}{\tilde{S}_{33}} + \theta_3^N \frac{\tilde{S}_{23}}{\tilde{S}_{33}} e^{i\epsilon \beta_{32} x}. \quad (4.1)$$

これより θ_2^P, θ_2^N に関し解けた形のコーシー積分表示を得る。

$$\left. \begin{aligned} (\theta_2^P / \tilde{S}_{11})(\lambda, x) \\ (\theta_2^N / \tilde{S}_{33})(\lambda, x) \end{aligned} \right\} = |2\rangle + \frac{1}{2\pi i} \int_{-\infty}^{\infty} \frac{d\xi}{\xi - \lambda} \{ \theta_3^N \tilde{\gamma}_3^2 e^{-i\epsilon \beta_{23} x} - \theta_1^P \tilde{\gamma}_1^2 e^{i\epsilon \beta_{12} x} \} (\xi, x). \quad (4.2)$$

但し、 $\tilde{\gamma}_k = \langle j | [\tilde{S}_1^P + \tilde{S}_1^N] | k \rangle$ 。 θ_1^P, θ_3^N の表示も同様に与えられるが、変換演算子の核が定義できる。

$$K^P(x, y) = -\frac{\beta_{12}}{2\pi} \int_{-\infty}^{\infty} \{ \theta_1^P(\xi + i\epsilon, x) - |1\rangle \} e^{i\epsilon \beta_{12}(x-y)} d\xi,$$

$$K^N(x, y) = -\frac{\beta_{23}}{2\pi} \int_{-\infty}^{\infty} \{ \theta_3^N(\xi - i\epsilon, x) - |3\rangle \} e^{-i\epsilon\beta_{23}(x-y)} d\xi. \quad (0 < \epsilon \ll 1) \quad (4.3)$$

この核に関する閉じたGel' fand-Levitan 方程式, 又式(3.16), (3.20), (4.3)より核とポテンシャルの関係が求まる。¹⁴⁾ 我々は式(3.13)の行列が零点を持たない(連続スペクトルのみ)としている。

$M=4$ のケースの解析は複雑であるが付録Bに示したS行列の分解を使えば, 式(3.18)が書き下せる。

$$\begin{cases} \hat{\theta}_1^P - \hat{\theta}_1^N = -\hat{\theta}_2^N \gamma_1^2 e^{i\epsilon\beta_{21}x} + \hat{\theta}_3^N \tilde{\rho}_3^2 e^{i\epsilon\beta_{31}x} + \hat{\theta}_4^N \tilde{\gamma}_4^1 e^{i\epsilon\beta_{41}x}, \\ \hat{\theta}_4^N - \hat{\theta}_4^P = -\hat{\theta}_3^P \gamma_4^3 e^{i\epsilon\beta_{34}x} + \hat{\theta}_2^P \tilde{\rho}_2^4 e^{i\epsilon\beta_{24}x} + \hat{\theta}_1^P \tilde{\gamma}_1^4 e^{i\epsilon\beta_{14}x}, \end{cases} \quad (4.4 a)$$

$$\begin{cases} \hat{\theta}_2^P - \hat{\theta}_2^N = \hat{\theta}_4^N \tilde{\gamma}_4^2 e^{i\epsilon\beta_{42}x} + \hat{\theta}_3^N \tilde{\rho}_3^2 e^{i\epsilon\beta_{32}x} - \hat{\theta}_1^P \tilde{\gamma}_1^2 e^{i\epsilon\beta_{12}x}, \\ \hat{\theta}_3^N - \hat{\theta}_3^P = \hat{\theta}_1^P \tilde{\gamma}_1^3 e^{i\epsilon\beta_{13}x} + \hat{\theta}_2^P \tilde{\rho}_2^3 e^{i\epsilon\beta_{23}x} - \hat{\theta}_4^N \tilde{\gamma}_4^3 e^{i\epsilon\beta_{43}x}. \end{cases} \quad (4.4 b)$$

但し,

$$\tilde{S}_I^P = \begin{bmatrix} 1, \\ \tilde{\gamma}_1^2, 1, \\ \tilde{\gamma}_1^3, \tilde{\rho}_2^3, 1, \\ \tilde{\gamma}_1^4, \tilde{\rho}_2^4, -\gamma_4^3, 1 \end{bmatrix}, \quad \tilde{S}_I^N = \begin{bmatrix} 1, -\gamma_1^2, \tilde{\rho}_3^1, \tilde{\gamma}_4^1 \\ 1, \tilde{\rho}_3^2, \tilde{\gamma}_4^2 \\ 1, \tilde{\gamma}_4^3 \\ 1 \end{bmatrix}. \quad (4.5)$$

$\hat{\theta}_1^P (= \theta_1^P)$ と $\hat{\theta}_4^N (= \theta_4^N)$ は (4.3) 式の様に入独立な核を定義するが (4.4 a) 式より判る様に, それらのコーシー積分表示には, $\theta_{2,3}^N$ が含まれる。 $M=3$ では, これは(4.1), (4.2)式を使って消去されそれでGel' fand-Levitan方程式が構成されたが, 今のケースではその操作は困難である。(4.1)式に相当する式は(4.4 b)で変数が倍に増えたのに応じて2ヶの関係があるのだけれど, それを使って, $\hat{\theta}_2^P, \hat{\theta}_3^N$ の閉じた形のコーシー積分表示が作れないのである。それが可能になるのは $\tilde{\rho}_3^2, \rho_3^2$ が消失するケースである。

$$\tilde{\rho}_3^2 \triangleq \frac{|\tilde{S}_{23}, \tilde{S}_{44}|}{|\tilde{S}_{33}, \tilde{S}_{44}|} = 0, \quad \tilde{\rho}_3^3 \triangleq \frac{|\tilde{S}_{11}, \tilde{S}_{32}|}{|\tilde{S}_{11}, \tilde{S}_{22}|} = 0. \quad (4.6)$$

この困難は, ボルテラ形成分をベースにしている事に留意しよう。もっと広い意味で(4.4)式に対する解法が研究されるべきである。少くとも(4.5)式は, $\tilde{\rho}_3^2, \tilde{\rho}_3^3$ を小パラメーターとみて摂動解を持っており従って解の存在がいえる。(4.6)式を持つ意味, 極の寄与による解の研究が, 今後の課題となろう。

5. 結 言

$M \times M$ 次のスペクトラル問題の解析性が明らかにされ, それに関与する三角行列の代数が調べられた。スペクトラル解や, 散乱行列の主小行列式の構成を与えるリーマン・ヒルベルト問題の一般形式が与えられ, 逆散乱の問題がこれらの解法に帰着された。最も重要な結果は (3.18) 式に示すリーマン・ヒルベルト問題であり, 散乱(行列)データがS行列の三角分解で得られる2種の三角行列に相当する事を示している。この表示を変分して, ポテンシャルの変分と散乱データの変分を関係付ける式が得られる可能性があり, 高階系の線形化問題に対し重要である。更に, この関係は逆問題を直接解くGel' fand-Levitan方程式の導出に使われ, 実際 $M \leq 3$ で成功する。けれど, $4 \leq M$ では大きな困難に見舞れ, ある条件(4.6)が課されないと, Gel' fand-Levitan方程式は簡単に求まらないのである。

参 考 文 献

- (1) V. E. Zakharov and S. V. Manakov: JETP Soviet Phys. **42**(1976) 482
- (2) D. J. Kaup: Stud. Appl. Math. **55**(1976) 9
- (3) T. Kawata: Research Report of IPP Nagoya Univ., 1983, No.IPPJ-641
- (4) A. A. Belavin and V. E. Zakharov : Phys. Lett. **73B**(1978) 53
- (5) V. E. Zakharov and A. V. Mikhailov: Commun. Math. Phys. **74**(1980) 21
- (6) V. E. Zakharov and A. B. Shabat: Func. Anal. Appl. **13**(1980) 13
- (7) 川田 勉：富山大学工学部紀要, **35**, p101, 昭和59年3月
- (8) M. J. Ablowitz, D. J. Kaup, A. C. Newell and H. Segur: Stud. Appl. Math. **53**(1974) 249
- (9) T. Kawata: J. Phys. Soc. Jpn **51**(1982) 3381
- (10) T. Kawata: J. Phys. Soc. Jpn **53**(1984) 2879
- (11) P. J. Caudrey: Physica **6D**(1982) 51
- (12) A. B. Shabat: 1980 Plenum Publishing Co., translated from Differential Equations, **15**(1979) 1824
- (13) T. Kawata: "Triangular Factorizations and Riemann-Hilbert Problem of the AKNS Equation", J. Phys. Soc. Jpn. **54** (1985) 57
- (14) T. Kawata: "Riemann - Hilbert Problem and Inverse Scattering Method for the 3×3 -Spectral Problem", J. Phys. Soc. Jpn. **54** (1985) 885.

付録 A. 散乱行列の三角分解

行列 S (その要素を s_{ij} とする) の一意的三角分解を具体的に調べる。

A1) LDU分解

対角要素を 1 とする強三角行列 $L(= [\ell_m^j])$, $U(= [u_k^m])$ と対角行列 $D(= [d_m])$ で $S=LDU$ と分解する。この分野は一意であり, 次の関係から逐次的に L, D, U が決定できる。

$$s_{jk} = \sum_{m=1}^{\inf(j,k)} \ell_m^j d_m u_k^m \quad (j, k = 1, \dots, M) . \quad (A, 1)$$

但し和は $m=1$ より (j, k) の小さい値迄とられる。 s_{jk} が M 次行列の要素である事から $s_{jk} = s_{jk}^{(M)}$ と記すと

$$s_{jk}^{(M-1)} = \det \left[\begin{array}{cc} s_{jj}^{(M)} & s_{jk}^{(M)} \\ s_{j1}^{(M)} & s_{jk}^{(M)} \end{array} \right] \triangleq |s_{jj}^{(M)}, s_{jk}^{(M)}| \quad (2 \leq j, k), \quad s_{jk}^{(M-2)} = |s_{jj}^{(M-2)}, s_{jk}^{(M-1)}| \quad (3 \leq j, k), \dots,$$

の様に $(M-1)$ 次, $(M-2)$ 次の行列の要素を構成してゆける。この一般項は

$$s_{jk}^{(M-n+1)} = |s_{n-1, n-1}^{(M-n+2)}, s_{jk}^{(M-n+2)}| \quad (2 \leq n \leq j, k \leq M) \quad (A. 2 a)$$

与えられ, これを使えば, 三角行列成分は次式で与えられる。

$$\ell_n^j = \frac{s_{jn}^{(M-n+1)}}{s_{nn}^{(M-n+1)}}, \quad u_k^n = \frac{s_{nk}^{(M-n+1)}}{s_{nn}^{(M-n+1)}} . \quad (A : 2 b)$$

対角成分も同様に決定できる,

$$d_1 = s_{11}^{(M)}, d_2 = \frac{s_{22}^{(M-1)}}{s_{11}^{(M)}}, d_3 = \frac{s_{33}^{(M-2)}}{s_{11}^{(M)} s_{22}^{(M-1)}}, \dots, d_n = \frac{s_{nn}^{(M-n+1)}}{s_{11}^{(M)} s_{22}^{(M-1)} \dots s_{n-1, n-1}^{(M-n+2)}} \quad (A.2c)$$

これと違った表示もある。\$S=LDU\$の主小行列式を取れば容易に判るように、

$$d_1 = s_{11}, d_2 = \frac{|s_{11}, s_{22}|}{s_{11}}, d_3 = \frac{|s_{11}, s_{22}, s_{33}|}{|s_{11}, s_{22}|}, \dots, d_n = \frac{|s_{11}, \dots, s_{n-1, n-1}, s_{nn}|}{|s_{11}, \dots, s_{n-1, n-1}|} \quad (A.3)$$

これらより、主小行列式と (A.2a) 式の行列要素の間に何等かの関係が期待される。実際、計算をしてみると、次の関係が得られる。

$$s_{jk}^{(M-2)} = s_{11} |s_{11}, s_{22}, s_{jk}|, s_{jk}^{(M-3)} = (s_{11})^2 |s_{11}, s_{22}| \cdot |s_{11}, s_{22}, s_{33}, s_{jk}| \quad (A.4)$$

A2) UDL分解

改めて\$S=UDL\$とすれば、式 (A.1) に対応して、

$$s_{jk} = \sum_{m=\sup(j,k)}^M u_m^j d_m \ell_k^m \quad (A.5)$$

\$1 \le j, k \le M-n\$ において、各要素は次式で与えられる。

$$s_{jk}^{(M-n)} = |s_{jk}^{(M-n+1)}, s_{M-n+1, M-n+1}^{(M-n+1)}| \quad (A.6a)$$

$$u_{M-n}^j = \frac{s_{j, M-n}^{(M-n)}}{s_{M-n, M-n}^{(M-n)}}, \ell_k^{M-n} = \frac{s_{M-n, k}^{(M-n)}}{s_{M-n, M-n}^{(M-n)}}, d_{M-n} = \frac{s_{M-n, M-n}^{(M-n)}}{s_{MM}^{(M)} s_{M-1, M-1}^{(M-1)} \dots s_{M-n+1, M-n+1}^{(M-n+1)}} \quad (A.6b)$$

式 (A.3), (A.4) に対応して

$$d_M = s_{MM}, d_{M-1} = \frac{|s_{M-1, M-1}, s_{MM}|}{s_{MM}}, d_{M-2} = \frac{|s_{M-2, M-2}, s_{M-1, M-1}, s_{MM}|}{|s_{M-1, M-1}, s_{MM}|}, \dots, d_{M-n} = \frac{|s_{M-n, M-n}, s_{M+n-1, M-n+1}, \dots, s_{MM}|}{|s_{M-n+1, M-n+1}, \dots, s_{MM}|} \quad (A.7)$$

$$s_{jk}^{(M-2)} = s_{MM} |s_{jk}, s_{M-1, M-1}, s_{MM}|, s_{jk}^{(M-3)} = (s_{MM})^2 |s_{M-1, M-1}, s_{MM}| \cdot |s_{jk}, s_{M-2, M-2}, s_{M-1, M-1}, s_{MM}| \quad (A.8)$$

これら式 (A.3), (A.4), (A.7), (A.8) は、分解のケース\$LDU, UDL\$に独立な表示を与える。尚、ここでは随伴行列\$S\$については省略する。

付録B. 4 × 4 散乱行列 (M = 4)

ここでは\$M = 4\$の散乱行列を扱う。\$\det S = 1, \tilde{S}^T S = E\$の条件も課される。まず、

$$\tilde{S} = [S^T]^{-1} \equiv \begin{bmatrix} |s_{22}, s_{33}, s_{44}|, & -|s_{21}, s_{33}, s_{44}|, & |s_{21}, s_{32}, s_{44}|, & -|s_{21}, s_{32}, s_{43}| \\ -|s_{12}, s_{33}, s_{44}|, & |s_{11}, s_{33}, s_{44}|, & -|s_{11}, s_{32}, s_{44}|, & |s_{11}, s_{32}, s_{43}| \\ |s_{12}, s_{23}, s_{44}|, & -|s_{11}, s_{23}, s_{44}|, & |s_{11}, s_{22}, s_{44}|, & -|s_{11}, s_{22}, s_{43}| \\ -|s_{12}, s_{23}, s_{34}|, & |s_{11}, s_{23}, s_{34}|, & -|s_{11}, s_{22}, s_{34}|, & |s_{11}, s_{22}, s_{33}| \end{bmatrix} \quad (B.1)$$

式(A.2)-(A.4)を使えば、\$S\$の\$LDU\$分解を、その表示法に独立な形で与えることができる。今、式(3.1)の\$S=S^1 S^2 S^3 S^4\$に従うとする。而るに\$\det S = 1\$より、対角部\$S^i\$は

Triangular Factorizations and Matrix Riemann-Hilbert Problems

Tsutomu KAWATA

An important type of $M \times M$ -th spectral problems are studied for developing its inverse scattering theory. Under the assumption of the potential on a compact support, we show that the spectral solution can be continued analytically into the upper or lower spectral plane and result in triangular states at $x = \pm \infty$. The triangular factorization of the scattering matrix is studied generally and the inverse problems reduced to a "principal" type of Riemann-Hilbert problems. The scattering data is given by the "strongly" triangular matrices for the scattering matrix. For $M \leq 3$ the Gel'fand-Levitan integral equation which solves the inverse problems systematically derived, while this falls difficult for $4 \leq M$.

[英文和訳]

三角行列分解と行列リーマン・ヒルベルト問題

川 田 勉

$M \times M$ 次オーダーの重要なスペクトラル方程式の逆散乱法が研究される。有限台上でのみ値を持つポテンシャルを仮定して、解のスペクトラル平面の上半面への解析接続可能性と $x \rightarrow \pm \infty$ で三角行列状態を取る事が示される。一般的に散乱行列の三角行列分解が行われ、これにより逆問題は "主行列リーマン・ヒルベルト問題" に帰着される。又、散乱データは、散乱行列を分解して得られる三角行列部に相当する事が判る。 $M \leq 3$ では、逆問題を解く所の Gel'fand-Levitan 積分方程式が体系的に求まるが、 $4 \leq M$ では大きな困難におちいる。

(1984年10月31日受理)

昭和58年度富山大学大学院工学研究科学位論文一覧表

〔電気工学専攻〕

コオロギにおける触覚運動の電気生理学的研究

上 埜 英 昭

コオロギは触覚運動により外界情報の一部を収集している他に、他の個体との間で情報交換を行っている。この触覚運動はいかなる指令所（脳のいかなる場所）からの神経情報によって制御されているのかを、触覚の運動を直接駆動している横紋筋から、フック電極を介して電気活動を検出し、解析した。この制御は、それぞれ脳内にある4種の運動ニューロン、すなわち左から右へ、その逆、上から下へ、その逆へ動かす指令を発生する神経細胞の存在が、電気生理学的に確認された。これらの運動と相互の情報交換との関係は、今後の課題であろう。特に、脳の活動と触覚運動との関係は、将来のロボットのセンサーへの道を開くのに大きく貢献しよう。

直接差分モデルによる水蒸気バブルの生成シミュレーション

浦 田 久 雄

ノンインパクト型図形文字出力装置として、インクジェット方式が注目を集めている。その中でバブルジェット方式は、インクを満たしたノズル内に発熱素子を組み込んだもので、急激な加熱により気泡が生じ、それが蒸気圧によってインクを吐出する方式である。

このバブルジェット方式のメカニズムは大きく分けて気泡の成長・収縮とインクの流動・吐出から成っている。これは互いに関連を持っているが、まず気泡の成長・収縮のモデルから得られた成長曲線を駆動条件として、インクの流動・吐出を直接差分法でシミュレーションした。印加時間を長くし、熱を加え続けると一度成長した気泡が収縮し、また気泡が再膨張するなど実験で観測される様子が定性的ではあるが、よくシミュレートされた。

小動物の機能測定のためのトランスジューサに関する研究

田 淵 眞 澄

小動物の各種機能測定は、脊椎動物のそれらの計測に比して、研究方法が大変遅れている。それは、小動物に大きな負荷を与えずにこれらを計測せねばならないという制約があるためである。

本研究は、各種機能を測定するためのトランスジューサ一般につき検討した後、昆虫を中心として、歩行、呼吸運動などの計測を行う変換器について検討したもので、主題は、フォト・インタ・ラプタを中心とした光センサを用いた方法である。センサよりの情報は有線方式、無線方式それぞれ両方につき伝送手段として検討してきたが、被検体によりそれぞれ使い分けのが良いことが明確になった。

〔工業化学専攻〕

ビスクロ [3,3,0] オクター-2,6-ジオンジエナミンより ヘプタレン核及びジアズレノペンタレン核の合成

池 田 まり子

ビスクロ [3,3,0] オクター-2,6-ジオンジエナミンとジメチルアセチレンジカルボキシレート (DMAD) との反応により、ヘプタレン核の合成を行った。又、オキサズラノンとの反応により、テトラヒドロジアズレノペンタレンが得られた。これをジトリフルオロアセチル化し、脱水素反応により、ジヒドロ体、又DDQ酸化により、ジケトン体が合成された。

アルキル化による石炭の可溶化 —ジグライムを溶媒とした石炭の繰返し還元メチル化—

厚 主 文 弘

石炭の可溶化効率と可溶化物の構造特性に就て更に詳細な情報を得るため、品位の異なる石炭5種を、石炭/金属カリウム/ジグライム系で3時間を単位に1回~9回還元メチル化した。各石炭の可溶化度はメチル化回数が多くなるに従って指数関数的に増加した。9回処理して可溶化度は下記の順となり、

Kairan (81%) > Akabira (50%) > Illinois No.6 (39%) > Daido (31%) > Wandoan (16%)
繰返しメチル化することによってベンゼン不溶分が可溶分に転化する様子が明瞭に観察された。各メチル化段階のベンゼン可溶分はGPC法で分別し構造パラメータを算出した。概してKairanの様に、繰返し初期の段階で良く溶解する石炭は既溶のベンゼン可溶分が電子移動剤として働き繰返し処理する方法は効果があるが、Wandoan などのような低品位炭の場合には、電子移動剤の添加が必要であると思われた。

1-メチルシクロアルキルフェニルスルホキシドの脱離反応機構

関 岡 忠 康

1-メチルシクロアルキルフェニルスルホキシド類を熱分解させ、その脱離反応機構を動力学的に検討した。これらのスルホキシドを熱分解させると endo 及び exo の両方のオレフィンを生成するがそのオレフィンの選択性や反応速度に対する環の大きさの効果、また環を6員環に固定して、フェニル基上の置換基の効果や同位体効果及び活性化パラメータ、溶媒効果を検討した結果、この脱離反応はS-C_α結合とC_β-H結合の切断が協奏的起こるが、その遷移状態は6員環でexoオレフィンを選択的に与えるほどの立体規制が崩れない程度にS-C_α結合が伸びたE I型に片寄った構造をしていることが推定された。

(日本化学会第47及び第49春季年会で発表)

無水マレイン酸及びエチレンイミン含有 複合樹脂のウラン吸着に関する研究

高 田 京 子

無水マレイン酸—イソブテン共重合体にポリエチレンイミンを反応させた樹脂中の窒素とカルボキシルとの当量比を 1.0 以上にした複合樹脂は(1)陰イオン系を良く吸着する。(2)ウランに対する優れた選択吸着性を示す。(3)多量の塩類と共存する海水中のウラン (3.3 P P b) の回収に適用しうることを認めた。これらの結果より当樹脂へのウランの吸着は $UO_2(CO_3)_3^{4-}$ であると推定した。X線マイクロアナライザで海水に溶存する諸元素の樹脂への吸着分布状況を測定し樹脂改質の知見を得た。

脱水閉環によるベンズアズレン類及び縮環フェナレノン類の合成

田 中 英 司

トロポンとベンジルクロリドのグリニャール試薬との反応で得られるケトン体に 2mol の塩化水素を付加し、これを 85% 硫酸で処理すると、1 段階で脱水閉環、脱塩化水素、酸化が起り、ベンズアズレンを与えた。又、シクロアルカノンと 1-ホルミル-2-メトキシナフタリンより得られる縮合体を直接あるいは部分接触還元した後、85% 硫酸により脱水閉環を行なうと 1 段階で縮環フェナレノン類が合成された。

置換アゾキシベンゼンの合成と反応

南 部 元 志

モノ置換アゾキシベンゼンは一般に硫酸により転位し、おもに 4-ヒドロキシアゾベンゼン類を生成する。電子吸引性基があるとき水酸基は置換基のない方のベンゼン核により多く入り、電子供与性基が存在するときは置換基のついたベンゼン核に多く入る。またアゾベンゼン類への還元および少量の 2-ヒドロキシアゾベンゼン類の生成もおこった。置換基の種類および位置の反応性への影響などについて調べた。

〔金属工学専攻〕

Cu-Zn 系合金における加工硬化係数 nの変化に伴うすべり模様の光顕観察

浅井 康夫

f. C. C. 合金の代表であるCu基合金の塑性変形特性を組織学的に解析し、新解釈を加えた。即ち、金属の変形はマクロ的に均一変形すると仮定し、同一機構により破壊に至るとされてきた。これに転位論的なすべり帯の因子を導入し検討して、材料の持つすべり様式が変形特性を定めていることを解明した。

また、すべり様式を定めるものとして結晶粒界及び粒内における転位構造の概念を導入して、変形特性を明らかにした。

Ni-Al 系合金の時効過程における析出挙動について

久保 嘉成

耐熱用超合金の析出相 γ' の挙動については、従来構生成一成長反応によって析出するものか、スピノーダル分解によるかいろいろ論議されてきた。本研究はNi 4~7.5%Al合金の時効過程を電気抵抗測定から検討し、またTEMによる組織観察から変調構造組織を形成する過程を γ' 相の析出間隔に注目して定量的に整理した。その結果、本来合金では溶質濃度と時効温度に応じてスピノーダル分解域の構生成一成長反応域が存在することを明らかにできた。

Versatic Acid 10によるFeの溶媒抽出に関する研究

矢野 豊

湿式製錬法の単位プロセスである浄液あるいは有価成分の濃縮分離行程に溶媒抽出法を適用する研究の一環としてVersatic Acid 10によるFeの抽出反応についての検討を行ない、抽出の総括反応、抽出速度におよぼす環境因子の影響を定量的に検討した結果をもとに、抽出種、平衡定数の決定を行った。さらに抽出反応機構についても考察した。

Al-Mg-Si 系合金における時効析出と機械的性質

山 本 有 一

典型的な時効硬化型アルミニウム合金である Al-Mg-Si 合金は、粒界破断により極端に延性が少ないことが問題である。本研究は、加工熱処理法を適用し、顕著な延性の上昇をはかり、Al-Mg-Si 合金の新用途を開発すると共に、延性改善の機構を明らかとしたものである。即ち、この種の合金では粒界における優先析出が破断の主因であり、この優先析出を理論的手順に従って処理して抑制することにより延性の豊かな材性を開発することに成功した。

[機械工学専攻]

乱流境界層における熱線風速計の特性

古場田 良 之

壁面近傍の流速を熱線風速計で測定する場合、壁への熱損失が加わるために速度誤差を生ずる。この問題に対して、熱線から失われる熱量として対流、空気の熱伝導、サポートへの熱伝導および熱ふく射を考慮し、圧力勾配のない平板乱流境界層において実験的に研究し、層流境界層の場合の実験および数値計算結果と比較検討し、熱線風速計が壁面から受ける影響の大小は熱線の高さと速度勾配によって決定されることを導いた。

回転曲り矩形管内の流れ

櫻 野 克 也

矩形断面曲り管がその曲率中心軸の回りに一定角速度で回転するときの十分発達した領域における層流強制対流問題を、熱流束一定で断面の周囲温度が一定の仮定の下で数値解析を行った。その結果、ディーン数の増加につれて付随渦は発生・消滅を繰り返し、付随渦の発生に伴い、平均管摩擦係数、平均ヌセルト数は著しく増加すること、また、断面の縦横比および回転レイノルズ数の違いにより付随渦発生限界のディーン数が異なることを明らかにした。

低温における粉体真空断熱に関する研究

佐藤 佳司

低温における有効な断熱方法として、グラスバブルス、パーライト等の低密度粒子充てん層を用いた粉体真空断熱が注目されている。本研究では、このような低密度粒子充てん層におけるふく射伝熱を減少させるために、グラスバブルス表面にニッケルメッキ、半球状アルミ被膜を施した粒子や、アルミ粉、アルミ箔片等を混入した充てん層について実験を行い、充てん層の温度と有効熱伝導率の関係、表面処理を施したグラスバブルスやアルミ箔片の混入率と有効熱伝導率との関係を考察した。さらに充てん層内の熱流束を伝導によるものとふく射によるものとに分けて考えることによって、ふく射伝熱に対するアルミ粉等の寄与を検討した。

スラスト軸受の動特性におよぼす潤滑流体の慣性力の影響に関する研究

吉澤 慎一

軸受の動特性を潤滑流体の慣性力を考慮して解析するに当たって、微小な調和振動の仮定のもとに時間的加速度項を比較的厳密に評価する解法を提案し、従来より行なわれている近似解法と比較して近似の精度を調べた。数値解析結果との比較、実験的な検討も加えて、提案する解法は非定常性の強い領域でも精度が良いこと、平均化法も比較的良いこと等がわかった。

〔生産機械工学専攻〕

焼入れ焼戻し鋼における研削加工層について

沢崎 康二

中高炭素鋼および中高炭素合金鋼について焼入れ焼戻しを行い、同一鋼種についてもかたさを変えて調質した試料を研削し、研削残留応力、研削面下の硬度変化の測定を行った。

その結果、残留応力の大きさおよび引張応力の分布深さは試料かたさの影響を受ける。また高かたさ、特にマルテンサイト組織のものは残留応力の発生には、研削熱による焼戻し効果が大きく影響し、これによって最大残留応力および残留応力の分布深さは増大する。

CO₂レーザの製作と応用に関する研究

浜 田 真

レーザ計測技術は、被測定物から非接触で各種の測定値が得られることから注目されている。この報告では波長10.6 μ mのCO₂レーザを試作し、物体の表面粗さの測定を試みた。トワイマングリーン光学系をセットし、物体表面と参照鏡との干渉によって生じる干渉縞のビジビリティから三次元的な粗さを求めた。この結果、従来の理論と比較して、より実験と近似した理論式が得られた。また、粗面物体の形状の測定も可能となった。

〔化学工学専攻〕

流動層型生物膜廃水処理装置によるBOD、COD処理

石 橋 大 策

流動層型生物膜廃水処理装置による、高容積負荷状態での廃水中のBOD、COD処理について、実験的に検討した。その結果、以下のことが明らかとなった。

- i) 流動層型生物膜廃水処理装置は、単位容積当りの処理速度が非常に大きく、BOD処理の場合、最低でも標準活性汚泥法の場合の15倍程度となる。
- ii) 1日に数時間ずつ停止する間歇処理も可能である。
- iii) 処理速度は、層内の溶存酸素濃度に大きく影響を受ける。

W/O/Wエマルションの滴径 に及ぼす界面活性剤濃度の影響

田 中 成 典

水中に分散した油滴中に水滴が分散しているW/O/W型エマルションは、液膜による分離操作への応用が期待されるが、本研究では、水-ケロシン系を用い、その滴径に及ぼす添加界面活性剤濃度の影響について実験的に検討を加えた。その結果、平均滴径及び滴径分布は、界面張力、連続水相粘度等の影響を受けて、より単純なO/W型エマルションとは異なる変化が観察された。

単一水平回転円錐型容器を用いた閉回路造粒プロセスの検討

中 村 恵 威

粉体プロセスの如く低エネルギー効率の工業プロセスの省エネルギー化の一つに、2 またはそれ以上のプロセスの複合化が見当る。

本研究では、水平回転円錐型容器内の粉粒体の偏析現象に伴う分粒効果と、回転容器内の粉末の造粒効果を利用して、単一水平回転円錐型容器による微粉末の造粒と分粒との同時操作を検討し、省エネルギー的連続造粒プロセスの一つとして、同容器による開回路、及び閉回路造粒プロセスの開発を試みた。その結果、バンダー（水）とともに供給された微粉末（ CaCO_3 粉末）は同容器内で造粒と同時に分粒され、容器一端より均一球状製品が、他端より不均一非球状粒子が排出されることを確かめ、さらに、閉回路造粒システムの導入により、製品の改善を確かめ得た。

多孔性固体電極の有効係数について

西 尾 弘 伸

粒子充填層型の多孔性固体電極の反応器挙動を銅粒子-硫酸銅（硫酸）系を用いて調べた。粒子径、層高、銅イオン濃度などを実験変数として、層内過電圧分布を求めた結果、層高の影響が顕著で、長さ方向の泳動電流と系の交換電流の比の $1/2$ 乗の指数関数で表わされること、層全体に層頂部の過電圧を仮定した場合のTafel 型電解電流と実測電流の比を有効係数として求めた結果、過電圧分布とおなじ電流比の $1/2$ 乗のパラメータで良好に相関できることなどがわかった。

矩形ダクト内乱流促進体による物質移動の増進機構に関する研究

平 野 誠 一

熱交換器流路内における壁・液間の伝熱促進を目的として流路内に乱流促進体を設置し、種々の装置変数（促進体径、ピッチ、クリアランス）および操作変数（レイノルズ数）を変化させて伝熱増進の度合を電気化学的に測定した。

そしてその増進のメカニズムの究明を目的として乱流強度、剪断応力、物質移動の変動強度 etc を測り、輸送現象論的に解明を試みた。

特定制御対象についての人間の制御特性の追求

吉 村 浩 吉

むだ時間のある一次遅れ系制御対象にステップ状外乱を入力したときの人間による制御の成績（ITAE値で評価）と人間に与えた信号の種類の間を追求した。時定数が小さくむだ時間のないときは人間の思考動作を補うための情報（過去のデータのグラフ）を与えると制御成績が向上するが、時定数やむだ時間が大になると余分な情報の提示は却って制御成績を下げた。

〔電子工学専攻〕

層間化合物の合成と電子物性に関する研究

池 上 雅 一

新しい物質を合成する目的で、層状半導体 GaSe, InSe の層間に蒸気反応法、溶液反応法によってアルカリ金属を挿入し、層間化合物を作製することを試みた。蒸気反応法では結晶全体に均一ではないが、MoS₂ に Cs 及び K をインターカレーション（挿入）することが出来た。インターカレーションによって MoS₂ の層間は Cs の場合は 2.86 Å, K の場合は 1.68 Å 拡がることがわかった。HMPA を用いた溶液法では MoS₂ の比抵抗は Na のインターカレーションにより 1/10~1/100 に減少した。

III-VI 族層状半導体の熱酸化過程の研究

入 野 清

III-VI 族層状半導体 GaSe, InSe の空気中での種々の温度における熱酸化の進行過程を XPS（X線光電子分光法）により研究した。酸化は時間と共に一様に進行するのではなく、最初およそ 1 原子層程度の酸素の吸着が起きた後、ある程度時間が経過してから急激に進むこと、酸化が充分進んだ時点では表面はそれぞれ Ga₂O₃, In₂O₃ となっていることがわかった。又、表面電位は酸化によって InSe の場合には上に 0.8eV, GaSe では下に 0.3eV 変化することを見出した。

垂直磁気記録による録画の研究

大 畑 司

垂直磁気記録方式は、従来行われている長手磁気記録方式に比較し、より高密度な記録を可能とする画期的手法である。まず、垂直記録の基本的な記録再生特性を測定することにより、従来方式に比較し14倍以上の高密度記録が行えることを確認した。又、二種類の変調方式を用い、ビデオ信号を垂直記録方式の大きな特徴であるセカンドピークに録画再生を行い、その有用性を明らかにした。

アンテナ近傍に存在する誘電体の及ぼす影響についての研究

鳥 山 一 郎

北陸、東北、北海道、山岳地域等に於いては、アンテナに雪が付着し、凍結し、落雪する過程に於いて通信に影響をおよぼしている。本論はこのような問題を解決する為のアンテナの基本的特性を得ることを目的とし、アンテナの近傍に任意の形のロスを含む誘電体が存在する場合の解析手段を与え、これにより計算結果を示した。

図書目録カードの自動認識に関する研究

藤 田 政 志

富山大学付属図書館で用いられている図書目録カードの自動読取りに関する実験を行った。主に洋書用カードについて行い、和書用カードに関しては判別分析により前者との分離について検討した結果、ほぼ100%分離できることがわかった。洋書用カードについては、主に入力カードからの行の取り出し、文字の切り出し、認識の各アルゴリズムを考案した。実験の結果、全過程を通しての認識率は77%であった。

酸化バナジウム蒸着膜のエレクトロクロミズムの機構に関する研究

藤 田 佳 隆

V_2O_5 粉末を抵抗加熱法でITOガラス基板上に真空蒸着して作製したアモルファス V_2O_5 薄膜エレクトロクロミック素子 (ECD) の光吸収特性、XPS (X線光電子分光)、SIMS (2次イオン質量分析) を測定し、そのエレクトロクロミズムの機構を研究した。その結果、 α - V_2O_5 の着色過程は電極からの電子と溶液からの L^+ イオンの2重注入により、 V_2O_5 の分子状態が VO_2 に変わるることによることが明らかとなった。

昭和 60 年 3 月 発行

富山県高岡市中川園町 1 の 1

富山大学工学部紀要委員会

Contents

| | |
|---|----|
| 1. Effects of Stabilizer on Dynamic Characteristics of Self-Controlled Externally Pressurized Bearing with Positive Static Stiffness (Frequency and Indicial Responses) | 1 |
|Tsuyoshi OHSUMI,Haruo MORI,Ken IKEUCHI | |
| 2. Augmentation Mechanism of Mass Transfer Among Turbulence Promoters on Wall Surface in Rectangular Duct | 10 |
|Hisashi MIYASHITA,Kaichiro WAKABAYASHI | |
| 3. Forced Reconnection by Nonlinear Magnetohydrodynamic Waves | 23 |
|Jun-ichi SAKAI, T. TAJIMA,F. BRUNEL | |
| 4. Explosive Transverse Electric Field and Particle Acceleration During Magnetic Collapse | 32 |
|Jun-ichi SAKAI, T. TAJIMA,Ryo SUGIHARA | |
| 5. Signatures of the Coalescence Instability in Solar Flares | 39 |
|Hiroshi NAKAJIMA.T. TAJIMA,F.BRUNELJun-ichi SAKAI | |
| 6. A Dynamical Model of Solar Prominences with Current Sheet | 47 |
|Jun-ichi SAKAI , Haruichi WASHIMI | |
| 7. Computer Modling of Fast Collisionless Reconnection | 53 |
|J.N.LEBOEUF,F.BRUNEL, T. TAJIMA,Jun-ichi SAKAI, C.C. WU, J.M. DAWSON | |
| 8. Triangular Factorizations and Matrix Riemann-Hilbert Problems | 66 |
|Tsutomu KAWATA | |
| 9. Abstract of Master degree s thesis in 1984 | 79 |